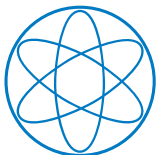# DEPARTMENT OF PHYSICS

TECHNISCHE UNIVERSITÄT MÜNCHEN

Characterization of the turbulence driven boron transport in the core of fusion plasmas in the ASDEX Upgrade tokamak

Cecilia Bruhn

HELMHOLTZ
RESEARCH FOR GRAND CHALLENGES

Fakultät für Physik

TECHNISCHE UNIVERSITÄT MÜNCHEN

Characterization of the turbulence driven boron transport in the core of fusion plasmas in the ASDEX Upgrade tokamak

Cecilia Bruhn

Vollständiger Abdruck der von der Fakultät für Physik der Technischen Universität München zur Erlangung der akademischen Grades eines

Doktors der Naturwissenschaften (Dr. rer. nat.)

genehmigten Dissertation.

Vorsitzender: Prof. Dr. Martin Zacharias
Prüfer der Dissertation: 1. Prof. Dr. Ulrich Stroth
                          2. Prof. Dr. Laura Fabbietti

Abstract

Nuclear fusion is the next carbon dioxide-free envisaged energy source. It occurs when two nuclei fuse together to form a heavier nucleus and in the process release energy. High particle energies are necessary to overcome the Coulomb barrier and enable the plasma ions to fuse together. One way of confining the energetic plasma particles is via magnetic confinement and the tokamak is a toroidal device that utilizes this technique. Impurities are other elements, except for the fusing ions, that are present in tokamak plasmas. If the transport and control of both light and heavy impurities are not well understood, they can hamper the goal of obtaining a self-sustained burning plasma.

In this thesis, a transient transport study of the low-Z impurity boron was conducted at the ASDEX Upgrade tokamak. Transient here means that the transport coefficients, that is the diffusivity and a convective velocity, from the radial transport equation could be individually determined. A requirement for such an analysis is a time-dependent boron density signal. At ASDEX Upgrade, such a signal for boron can be obtained by a square-wave modulation of the power of the ion cyclotron resonance heating (ICRH) antennas. This results in a periodic boron density signal with the same frequency as the modulation of the ICRH power. The boron content in the plasma is measured with the charge exchange recombination spectroscopy (CXRS) diagnostics. From the measured boron intensity, the boron density is calculated with the in-house code CHICA. This procedure yields boron profiles with high spatial and temporal resolution. The transport coefficients can then be deduced by solving an inverse problem in the form of a minimization. The functional form assumed for the boron density is a sum of a sine and a cosine, which describes the shape of the measured boron signal very well. This implemented framework yields good agreement between the measured and reconstructed boron densities, which in turn results in highly spatially-resolved diffusion and convective velocity profiles.

This experimental technique was utilized in several high confinement (H-mode) plasmas and a database of boron transport coefficients was assembled. The boron density profiles are observed to vary from very hollow to peaked with the convective velocity taking on values at mid-radius between $-5\,\mathrm{m/s}$ and $4\,\mathrm{m/s}$. The values of the diffusivity in the database at mid-radius range from $2\,\mathrm{m^2/s}$ up to $6\,\mathrm{m^2/s}$. This database was first compared to a previous boron steady-state study and this comparison showed consistency between the two datasets. To validate the transport theory, the transport coefficients in the database were compared to the theoretical predictions in the form of collisional (neoclassical) and turbulent transport theory. The neoclassical transport coefficients are considerably smaller than the experimental ones meaning that the transport in the performed experiments is turbulence driven. Comparing the experimental transport coefficients with the turbulent predictions shows a very good agreement in the diffusivity, however, a discrepancy in the convective velocity is observed. The theoretical convection is always more negative than the experimental one, hence, the

turbulent transport theory always predicts a more peaked boron density profile than what was experimentally measured. It is also observed that this discrepancy is worse for the most hollow boron density profiles meaning that there is still a piece of physics missing in the turbulent modeling especially for the hollow cases. Scalings between the plasma parameters and the transport coefficients were observed, but due to the strong correlations between the plasma parameters it is difficult to pinpoint which of the parameters have the highest influence on the boron transport.

In this work, high quality and high resolution profiles of the boron transport coefficients were measured for the first time. This study has clarified where there is agreement between the theoretical predictions and the experimental results, namely for the diffusion coefficient, but also where there is disagreement, namely for the convection. The gyrokinetic turbulent transport always predicts a stronger inward convection than measured, and the discrepancy is largest when the outward transport is strong, i.e. for hollow boron density profiles.

Zusammenfassung

Kernfusion ist die nächste zukünftige kohlendioxidfreie Energiequelle. Diese findet statt, wenn zwei Atomkerne zu einem schwereren Kern fusionieren und dabei Energie freisetzen. Es sind hohe Teilchenenergien notwendig, um die Coulomb Barriere zu überwinden, was es den Plasmaionen ermöglicht zu fusionieren. Eine Möglichkeit die fusionierenden Teilchen einzuschließen ist der magnetische Einschluss und der Tokamak ist ein toroidales Gefäß, das diese Technik nutzt. Verunrenigungen sind alle anderen Elemente, bis auf die fusionierenden Ionen, die in Tokamak Plasmen vorhanden sind. Ist der Transport und die Kontrolle von sowohl leichten, als auch schweren Verunreinigungen nicht gut verstanden, so können diese das Ziel, ein selbsterhaltendes brennendes Plasma zu erhalten, gefährden.

In dieser Arbeit wurde eine Studie des transienten Transports der low-Z Verunreinigung Bohr an dem ASDEX Upgrade Tokamak durchgeführt. Transient bedeutet in diesem Zusammenhang, dass die Transportkoeffizienten der radialen Transportgleichung, bestehend aus der Diffusivität und der Konvektion, einzeln bestimmt werden konnten. Eine Voraussetzung für eine solche Analyse ist ein zeitabhängiges Signal der Bohrdichte. An ASDEX Upgrade kann ein solches Signal durch eine Modulation der Leistung in den ICRH-Antennen mit einem Rechtecksignal erzeugt werden. Dadurch ergibt sich ein periodisches Signal in der Bohrdichte mit derselben Frequenz, wie die der Modulation der ICRH Leistung. Der Bohrgehalt des Plasmas wird mittels Ladungsaustausch-Spektroskopie gemessen. Aus der gemessenen Bohrintensität wird die Bohrdichte mit dem hauseigenenen Programm CHICA berechnet. Diese Methode ergibt Bohrdichteprofile mit hoher räumlicher und zeitlicher Auflösung. Von diesen können die Transportkoeffizienten abgeleitet werden, indem ein inverses Problem in Form einer Minimierung gelöst wird. Das Bohrdichteprofil wird als Summe von Sinus und Cosinus angenommen, was sehr gut mit der Form des gemessenen Bohrsignals übereinstimmt. Diese Methodik weißt eine gute Übereinstimmung zwischen gemessener und rekonstruierter Bohrdichte auf, und liefert räumlich hochaufgelöste Diffusions- und Geschwindigkeitsprofile. Diese experimentelle Technik wurde in mehreren Plasmen mit hohem Einschluss (H-Moden) benutzt, um eine Datenbank von Bohr-Transportkoeffizienten aufzustellen. Es wurde beobachtet, dass die radialen Bohrdichteprofile von sehr hohl zu spitz variieren, bei Driftgeschwindigkeiten an mittleren Radien mit Werten zwischen $-5\,\text{m/s}$ und $4\,\text{m/s}$. Die Werte der Diffusivität in diesem Bereich reichen in der Datenbank von $2\,\text{m}^2/\text{s}$ bis zu $6\,\text{m}^2/\text{s}$. Zunächst wurden die Ergebnisse dieser Datenbank mit einer vorherigen stationären Studie verglichen und dabei weitgehende Übereinstimmung zwischen beiden Datenbanken festgestellt. Um die Transporttheorie zu validieren, wurden die Transportkoeffizienten der Datenbank mit theoretischen Vorhersagen für den stoßbehafteten (neoklassischen) und den turbulenten Transport verglichen. Die neoklassischen Transportkoeffizienten sind deutlich kleiner als die experimentellen, was bedeutet, dass der Transport in den durchgeführten Exper-

imenten durch Turbulenz dominiert wird. Der Vergleich von experimentellen Diffusionskoeffizienten mit den turbulenten Vorhersagen ergibt eine sehr gute Übereinstimmung. Allerdings wird bei den Driftgeschwindigkeiten eine Diskrepanz beobachtet. Die theoretische Konvektion ist immer deutlich negativer als die experimentelle, weshalb die turbulente Transporttheorie stets ein spitzeres Bohrdichteprofil vorhersagt, als experimentell gemessen. Es wird auch beobachtet, dass diese Diskrepanz für die hohlsten Bohrdichteprofile größer ist, was bedeutet, dass die Modellierung des turbulenten Transports, insbesondere für die hohlen Fälle immer noch unzureichend ist. Es wurden Verbindungen zwischen den Plasmaparametern und den Transportkoeffizienten beobachtet, aber aufgrund der starken Korrelationen zwischen den Plasmaparametern ist es schwierig festzustellen, welche der Parameter den Bohrtransport am stärksten beeinflussen.

In dieser Arbeit wurden zum ersten Mal hochqualitative und hochaufgelöste Profile der Bohr-Transportkoeffizenten gemessen. Diese Studie hat klar gezeigt, worin die theoretischen Vorhersagen und experimentellen Ergebnisse übereinstimmen, nämlich bei den Diffusionskoeffizienten, aber auch, dass die Unterschiede bei der Konvektion liegen. Der gyrokinetische turbulente Transport sagt in allen Fällen eine stärkere nach innen gerichtete Konvektion als gemessen vorher. Hierbei sind die Unterschiede am größten, wenn die nach außen gerichtete Konvektion stark ist, d.h. unter einem hohlen Bohrdichteprofil.

Contents

Chapter 1.

Introduction

1.1. Nuclear fusion

Nuclear fusion is, in contrast to nuclear fission, the process of two light nuclei fusing together to form a heavier nucleus. For this reaction to take place, the kinetic energy of the fusing particles must be high enough to overcome the repulsive Coulomb force. At the high temperatures required for this to happen the atoms are fully stripped and form a plasma. In fusion reactions energy is released, since the binding energy of the fusing nuclei is larger than the binding energy of the fusion products. Nuclear fusion is the mechanism that powers the stars, starting with fusing hydrogen with hydrogen and in stages consequently creating heavier elements. The biggest limitation of a fusion reaction is the cross-section. The probability of the hydrogen-hydrogen reaction is too low for it to be a feasible candidate for fusion here on earth. This is, however, not a problem in the stars, since the high pressure in the star created by the gravitational force makes this fusion reaction possible. One of the reactions with the highest cross-section at achievable temperatures on earth, as well as a high energy yield, is when deuterium (D) fuses with tritium (T) to form helium (He):

$$^2_1\text{D} +^3_1\text{T} \rightarrow^4_2\text{He} + \text{n} + 17.6\,\text{MeV}. \tag{1.1}$$

The energy of this reaction (17.6 MeV) is released in the form of kinetic energy and is split between the neutron (14.1 MeV) and the alpha particle (3.5 MeV). The alpha particles will collide with other plasma particles and thus heat the plasma, while the neutrons will travel through the plasma without interacting. On earth, we have plentiful deuterium resources, since it can be extracted from water. Tritium, on the other hand, does not occur naturally, but can be produced from lithium. The plan for a future fusion reactor is to produce tritium through the reaction between lithium and neutrons behind the first wall inside the so-called Li-blanket. One of the main challenges in a future fusion reactor is to create a self-sustained burning plasma in which enough particles are confined for a sufficiently long time and at a sufficiently high density and temperature such that the heating from the alpha particles is the main source of heating for the plasma. This condition is called ignition and the threshold for fusion ignition can be formulated in the Lawson criterion [1]:

$$nT\tau_E > 3 \times 10^{21}\,\text{m}^{-3}\text{keVs} \tag{1.2}$$

where n is the plasma density, T the plasma temperature, and τ_E the energy confinement time. The range of acceptable temperatures T is defined by the cross-section of

the fusion reaction, whereas the choice of density n and energy confinement time τ_E depend on the confinement technique. There are mainly two different approaches for confining the particles here on earth: inertial confinement and magnetic confinement. The concept of inertial confinement [2] is to increase the density by compression. This is often accomplished by compressing frozen D-T pellets with laser beams. The aim with magnetic confinement [3] is to maximize the confinement time by trapping the particles with strong magnetic fields. Magnetic confinement devices, therefore, operate at lower plasma densities than inertial systems. Several schemes for magnetic confinement exist and the most promising ones are stellarators and tokamaks. The experiments presented in this thesis were performed in a tokamak. However, the turbulent transport physics studied here can also be more generally applied to any magnetized plasma system, including stellarators. In the next section, tokamaks will be described.

1.2. The tokamak concept

The tokamak concept was developed in the 1950s in the Soviet Union. A schematic picture of such a device is shown in figure 1.1. The bulk of the magnetic field holding the plasma is generated by toroidal field coils (blue coils in figure 1.1). Since the toroidal coils are closer together on the inner side of the machine than on the outer side, the toroidal magnetic field is not homogeneous and this leads to a drift velocity of the particle orbits:

$$\vec{v}_D = \frac{\frac{1}{2}mv_\perp^2 + mv_\parallel^2}{qB^3}(\vec{B} \times \nabla B). \tag{1.3}$$

Here m is the mass, q the charge and, $v_\perp$ and $v_\parallel$ are the perpendicular and parallel particle velocities to the magnetic field, respectively. This drift is charge dependent which leads to an up/down charge separation of the electrons and the ions. This charge separation in turn creates a vertical electric field. This electric field causes an additional outward $\vec{E} \times \vec{B}$ drift:

$$\vec{v}_{\vec{E} \times \vec{B}} = \frac{\vec{E} \times \vec{B}}{B^2}. \tag{1.4}$$

Thus, a toroidal field alone would result in an unstable plasma where all the particles drift outwards, and therefore, a poloidal field component (green arrows in figure 1.1) is imposed. This poloidal field component is created by induction of an Ohmic current in the plasma, which is done with the inner poloidal field coils (green in figure 1.1). These coils represent the primary circuit of a transformer with the plasma as the secondary circuit. The combination of the toroidal and poloidal magnetic fields results in helically twisted field lines (dark blue arrows in figure 1.1), which can confine the ionized plasma particles. This confinement is the result of the Lorentz force $\vec{F} = q(\vec{E} + \vec{v} \times \vec{B})$, which causes the charged particles to gyrate around the magnetic fields lines. This motion perpendicular to the magnetic field is limited to the drifts as in equation (1.3) and (1.4). Since the Ohmic current is inductively driven using a transformer, a conventional tokamak is always limited to pulsed operation, which limits the duration of a plasma discharge. Further outer poloidal field coils (gray in figure 1.1) are used for shaping and positioning of the plasma. The experiments in this work were carried out at the ASDEX Upgrade tokamak, which will be described in more detail in the next
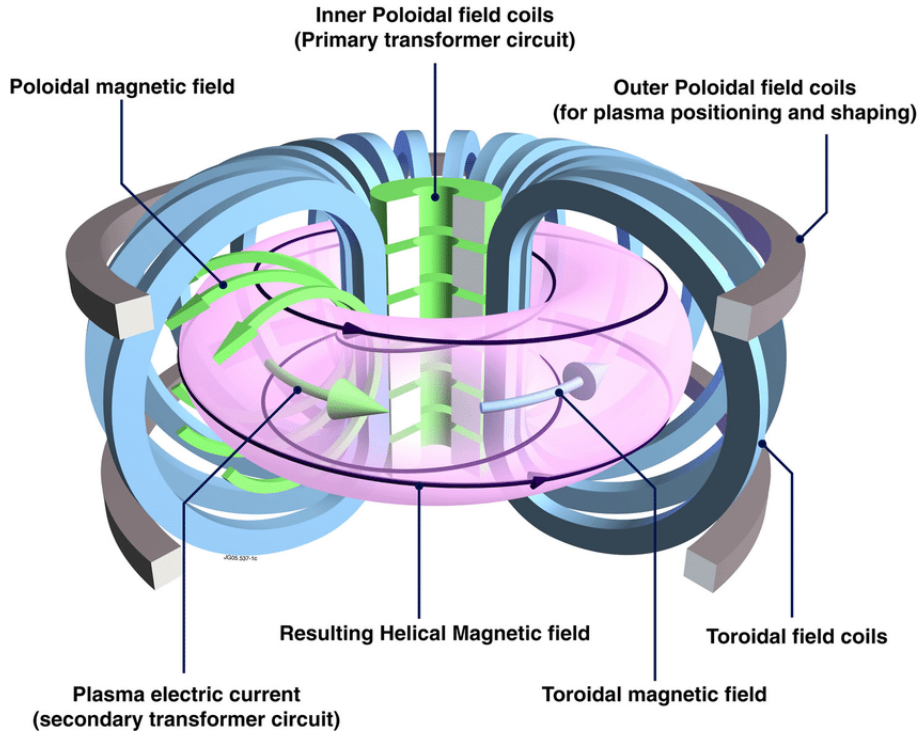
Figure 1.1.: Schematic picture of the structure of a tokamak. The superposition of the toroidal (light blue arrow) and poloidal magnetic field components (green arrows) result in a helical magnetic field (dark blue). The plasma is shaped and positioned by poloidal field coils (gray). Picture taken from [4].

chapter.

When describing the tokamak it is convenient to make use of its toroidal geometry. The safety factor q_s is a quantity that describes the helicity of the magnetic field lines:

$$q_s = \frac{2\pi}{\Delta\theta} = \frac{d\phi}{d\theta}, \tag{1.5}$$

where θ is the poloidal angle and ϕ is the toroidal angle. The safety factor corresponds to the number of toroidal turns a field line has to make before it closes. If q_s is not a rational number the magnetic field lines circulate an infinite number of times around the torus forming closed flux surfaces (see figure 1.2). The flux surfaces are, hence, contours of constant toroidal and poloidal magnetic flux. q_s characterizes the plasma stability; at rational q_s surfaces a variety of magnetohydrodynamic (MHD) instabilities [5] can develop, which break down the magnetic structure of flux surfaces and consequently can enhance the radial transport of heat and particles. It is specifically because the field lines close on themselves on rational surfaces, that allows periodic perturbations to grow there. One example is the sawtooth instability [6], which exist on the $q_s = 1$ surface. Hence in this particular case, the field line closes on itself after one toroidal and one poloidal turn. As a result of this instability, periodic increases and decreases of the plasma temperature and density are observed. Sawteeth were regularly observed in the experiments presented in this work, but this will be further discussed in chapter 4.

By using Ampere's law and integrating around one toroidal turn:

$$\oint B_t ds = \mu I_0 \Rightarrow 2\pi B_t R = \mu I_0 \tag{1.6}$$

we see that the toroidal magnetic field component B_t decreases from the inboard side towards the outboard side of the torus as

$$B_t \sim 1/R. \tag{1.7}$$

This forms two regions on a flux surface, one with higher B_t called the high field side (HFS) and one with lower B_t called the low field side (LFS) (see figure 1.2). The gradient of the magnetic field is a drive for plasma instabilities at the LFS, while it stabilizes the plasma at the HFS. This will be discussed further in chapter 4.

In magnetohydrodynamics (MHD) [7], the plasma is treated as an electrically conducting fluid. From the ideal MHD equations the force balance, for a plasma in equilibrium, reads:

$$\nabla p = \vec{j} \times \vec{B}, \tag{1.8}$$

where ∇p is the pressure gradient, $\vec{j}$ the plasma current, and $\vec{B}$ the magnetic field. This equation implies that the kinetic pressure of the plasma is balanced by the magnetic pressure and that the pressure is constant on magnetic flux surfaces. Due to the fast parallel transport along the magnetic field lines other parameters, for example, the density and temperature are also assumed to be constant on the flux surfaces. Since flux surfaces are contours of constant toroidal and poloidal magnetic flux, they can be used to define a normalized radial coordinate ρ. For example, from the toroidal flux Φ at the magnetic axis Φ_{axis} and at the separatrix or last closed flux surface (LCFS) $\Phi_{separatrix}$, ρ_{tor} is defined as:

$$\rho_{tor} = \sqrt{\frac{(\Phi - \Phi_{axis})}{(\Phi_{separatrix} - \Phi_{axis})}}. \tag{1.9}$$

This implies that $\rho_{tor} = 0$ at the magnetic axis and $\rho_{tor} = 1$ at the separatrix. This coordinate is used to represent flux quantities such as temperature and density in 1D profiles.

1.2.1. Divertor configuration

To avoid plasma contact with the wall of the vacuum vessel the divertor concept was developed at the Max Planck Institute for Plasma Physics. With external shaping coils the magnetic field is tailored in such a way that two regions exist: an inner one with closed magnetic flux surfaces and an outer one with open magnetic flux surfaces called the scrape-off layer (SOL) (see figure 1.3). The last closed flux surface or separatrix closes itself in the X-point and then continues down to the divertor target plates. The divertor can be seen as a dumpster for particles and its target plates are made out of materials that can withstand high heat loads. Since charged particles stream along the magnetic field lines, the particles which, due to radial transport, reach the open field lines will travel along them and then be directed into the divertor. The divertor
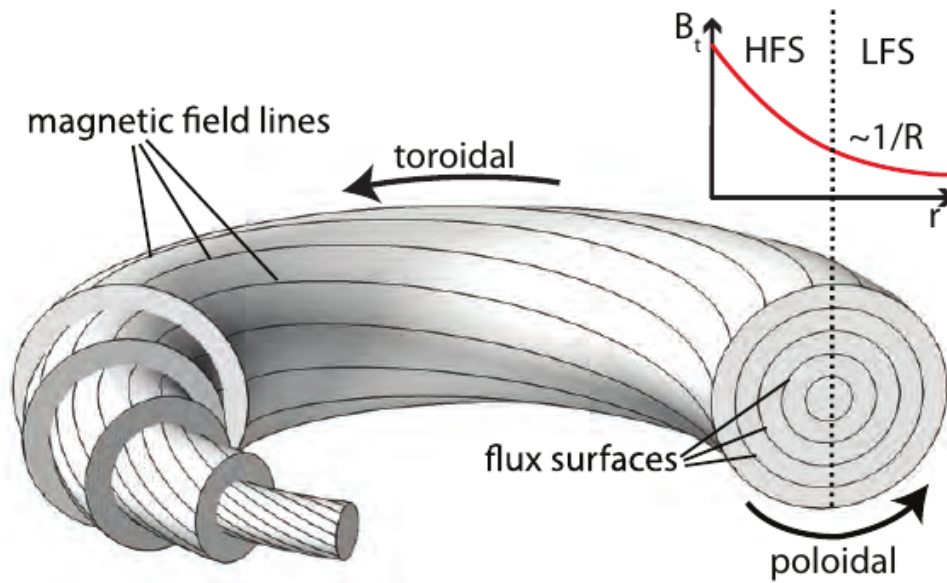
Figure 1.2.: Closed flux surfaces of constant pressure, density, and temperature. Picture taken from [8].

concept has several advantages and the main one is that it reduces the contamination of impurities in the confined region and thereby reduces the radiation losses and prevents dilution of the main ion population. Particles that end up in the divertor region can be pumped out. In a future fusion reactor, the so-called helium ash produced in the DT reaction (1.1) will be removed in this manner. Additionally, the divertor also allows easier access to the H-mode (see section below).
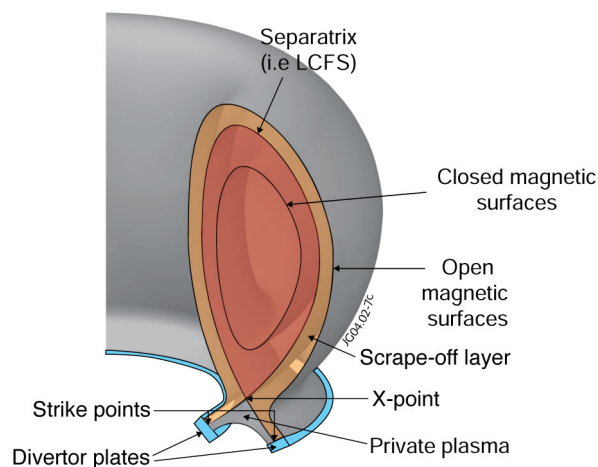
Figure 1.3.: A schematic picture of the divertor concept, which helps prevent the plasma from touching the vacuum vessel walls. The magnetic field is shaped in such a way that two regions are formed: the confined plasma region with closed flux surfaces and the scrape-off layer with open ones. Particles ending up outside of the last closed flux surface are deposited in the divertor. Picture taken from [4].
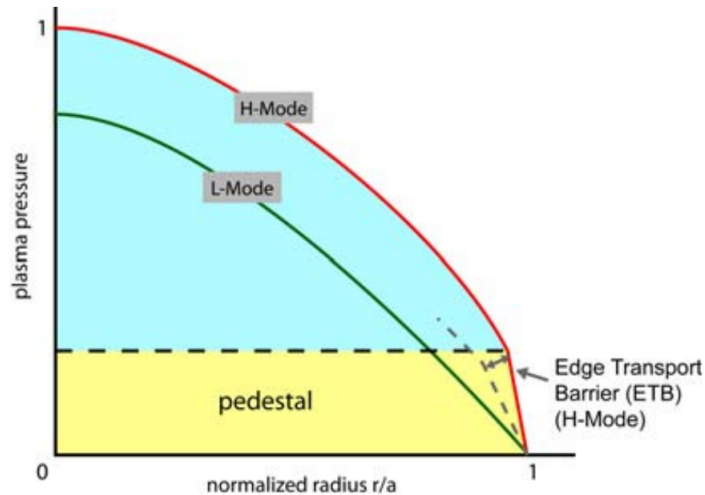
Figure 1.4.: Comparison of the pressure profile in L-mode and H-mode. In H-mode an edge transport barrier (ETB) is formed, in which the transport of particles and energy is reduced, resulting in the whole profile being "lifted up" and a higher core pressure. Picture taken from [11].

1.2.2. High confinement mode and edge localized modes

A tokamak plasma can be run in different regimes and the two most common regimes are the low confinement mode (L-mode) and the high confinement mode (H-mode). As the names suggest, the energy confinement time is higher in H-mode compared to L-mode by roughly a factor of 2. The H-mode was dicovered at ASDEX in 1982 [9]. By increasing the heating power the transition to H-mode is achieved. The L-H power threshold mainly depends on the magnetic field and the plasma density. At AUG the power threshold is between $1.4 - 2.3$ MW [10]. The improved energy confinement in H-mode is connected to the formation of a transport barrier (ETB) at the edge of the plasma. In the ETB the radial transport of heat and particles is reduced and this is characterized by a steepening of the pressure gradient and the formation of the so-called pedestal (see figure 1.4). This is connected to a suppression of the turbulence level in this region. The core temperature and density profiles in H-mode are stiff, meaning that above a critical threshold of the gradient of these profiles, a further increase in heating power does not cause a significant change in the gradient. However, the density and temperature profiles, just like the pressure, also exhibit a steepening at the pedestal in H-mode and the whole profile is "raised" enabling a higher core temperature and density, which otherwise would not be possible due to the stiffness of the profile in the core.

The H-mode is often accompanied by edge localised modes (ELMs) [12], which are quasi-periodical MHD instabilities. They cause a collapse of the pedestal and particles and heat are expelled from the plasma onto the open field lines resulting in a flattening of the associated gradients.

1.3. The role of impurities

Fusion plasmas are never pure (only the fuel ions exist) and impurities arise from many different sources: the erosion and sputtering of materials from plasma facing components, the intentional injection of impurities via gas puffing, pellets, or laser blow-off, and the production of helium from the fusion process itself. The presence of impurities affects the fusion performance in two ways. First, it dilutes the fuel reducing the probability of deuterium fusing with tritium. This is mainly the problem with the low-Z impurities. Second, the high-Z impurities increase the radiative cooling of the plasma. In the absence of impurities the power balance can be written as

$$P_\alpha = P_{rad} + P_{transport}, \tag{1.10}$$

where P_α is the heating from the alpha particles, P_{rad} is the energy losses due to radiation and $P_{transport}$ the energy losses due to particle and heat transport. To achieve a self-sustainable burning plasma this balance must be met, but in the presence of impurities, the operational window in which this is obtainable is significantly reduced [13]. This is visualized in figure 1.5, where the fusion triple product $nT\tau_E$, presented in equation (1.2), is plotted as a function of the temperature for a burning DT-plasma. The black lines represent the operational window for an ideal plasma with no helium. In this case, the alpha particles would transfer all of their energy to the plasma and be removed immediately after production and, thus, neither cool nor dilute the plasma. When considering a more realistic situation where the energy confinement time of helium is five times longer than the energy confinement time of the main ions we obtain a narrower operational space, which is shown in blue. For the red curves, we have added other impurities (carbon on the left hand side and tungsten on the right hand side) of various concentrations. The curves do indeed shrink the higher the concentration becomes and at some point the operational window fully closes and ignition is not possible. Despite this, impurities can, to some extent, be favorable. In modern tokamaks, most of the power is exhausted in the divertor causing this machine component to face extreme heat loads. Since the heat load scales with machine size, the divertor in a future reactor would not be able to withstand these power loads and start to melt. A considerable fraction of the power, therefore, has to be radiated from the edge of the plasma. This has to be done without deterioration of the core confinement. Often, impurities are seeded to create a radiative mantel for the purpose of edge and divertor cooling [14].

Impurities in a fusion reactor are unavoidable and, therefore, the main focus is to keep their concentration as low as possible in the plasma center. It is desirable that the main ion density profile is peaked in the core, hence n is maximized, while the impurity density profiles should be hollow in order to avoid central impurity accumulation. To achieve this, a fundamental understanding of the mechanisms behind the transport of both low- and high-Z impurities in fusion plasmas, the predictive capabilities, as well as the engineering parameters with which the transport can be controlled are essential.
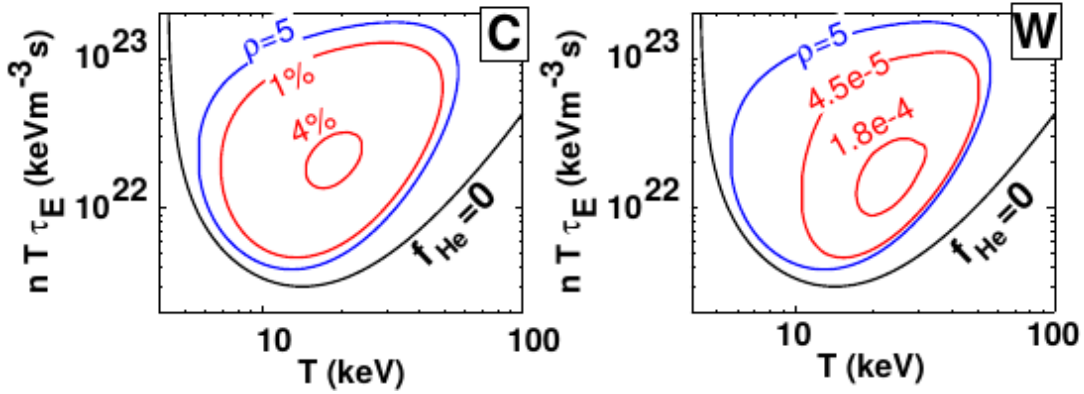
Figure 1.5.: Burning curves for a DT-plasma showing the extent of the possible operational window when impurities of different concentrations are added to the plasma. The black lines represent an idealized case with no impurities, that is, the produced helium transfers all of its energy to the plasma and is then instantly removed from the plasma. In the blue case the produced helium has an energy confinement time which is five times higher than the energy confinement time of the main ions. For the red lines carbon (left) and tungsten (right) has been added with different concentrations. The higher the impurity concentration is, the narrower the operational space becomes. Plot taken from [13].

1.4. This thesis

From the discussion on impurities in fusion plasmas in the previous section, it is understandable why impurity transport is a hot topic in the fusion community. In the past decades, we have reached a better understanding of the impurity transport, but there are still several open questions. As the equipment and the diagnostics at the different machines improve, we are able to experimentally measure the impurity transport with higher accuracy. From the theory side progress has also been made. A more reliable prediction of the transport has been enabled by faster codes and more advanced models. Thus, the gap between theory and experiment is slowly being bridged. Nevertheless, the picture is not complete and we still have a discrepancy between theory and experiment, which we will address in this work.

The main objective of this thesis was to characterize the core transport of the low-Z impurity boron. One part of the work was to develop a new boron modulation technique which should deliver highly resolved transport coefficients. The other part was to validate the theoretical understanding of impurity transport by comparing the experimentally deduced coefficients with the theoretical modeling. The experiments on the boron transport were carried out at the ASDEX Upgrade tokamak (AUG) and in chapter 2, AUG and some of its basic diagnostic systems will be presented. The boron content in the plasma can be measured with the charge exchange recombination spectroscopy (CXRS) diagnostics and, therefore, chapter 3 has been dedicated to explaining its basic principle, the calibration procedure, and the CXRS systems installed at AUG. In chapter 4, a short description of the theory of impurity transport will be given as well as a review on previous experimental transport studies. The newly devel-

oped modulation technique and the framework of obtaining the transport coefficients from the experimental data will be introduced in chapter 5. This technique has been utilized in several plasma discharges and a database of boron transport coefficients has been collected. The results of this database will be presented in chapter 6 along with a comparison to the theoretical modeling. This is followed by a conclusion in chapter 7.

Chapter 2.

The ASDEX Upgrade tokamak

2.1. The tokamak device

All experiments for this thesis were carried out at ASDEX (Axis Symetric Divertor EXperiment) Upgrade, which is a medium-sized divertor tokamak located at the Max-Planck-Institut für Plasmaphysik in Garching, Germany [15]. Starting in 1999, the carbon plasma facing components of ASDEX Upgrade (AUG) were gradually replaced by tungsten (W) components, reaching complete coverage in 2007 [16]. The major radius and the minor radius of the machine are 1.65 m and 0.5 m, respectively, which is half the size of the currently biggest tokamak in the world, JET, in Culham, UK and a quarter of the size of ITER, which is being built in Cadarache, France. 16 toroidal field coils provide a toroidal magnetic field from 1.8 T up to 3 T. Additional coils enable vertical and horizontal positioning of the plasma as well as plasma shaping. Typical operation features a deuterium D-shaped plasma with a pulse length of up to 10 s and plasma currents between $0.4 - 1.2$ MA. The heating systems and plasma diagnostics relevant to this work will be presented in this chapter.

2.2. Heating systems

As mentioned in chapter 1, a central solenoid induce an Ohmic plasma current. This plasma current also heats the plasma and is referred to as Ohmic heating (OH). OH power decreases with increasing temperature and is alone not sufficient to ignite a D-T plasma and, therefore, external heating must be applied [17]. This can be achieved through various heating mechanisms and AUG features several different auxiliary heating systems. The tokamak is equipped with neutral beam injection (NBI), electron cyclotron resonance heating (ECRH), as well as ion cyclotron resonance heating (ICRH), which allow AUG to easily access the high confinement mode (H-mode) [9]. These systems and their basic principles will be described in the following.

2.2.1. Neutral beam injection

The concept of NBI is to inject high energy neutral particles, since they can cross the magnetic field lines and keep a straight trajectory. At AUG the injected neutral species is usually the same as the plasma main ions, that is, a deuterium beam in a deuterium plasma and a hydrogen beam in a hydrogen plasma. If the kinetic energy of the neutral beam particles is higher than the thermal energy of the plasma, the plasma

will be heated up. The beam neutrals will become ionized when entering the plasma mainly through three collisional processes: ionization by electrons, ionization by ions, and charge exchange. The ionized beam particles, now confined in the plasma, will slow down via Coulomb collisions, and thus transfer their energy to the electrons and ions of the plasma, e.g., heat up the plasma [18].

The generation of the neutral beam itself can be described in three stages. First, an ion beam is generated from an ion source and then accelerated by a high voltage grid. Second, the accelerated ion beam goes through a neutralizer, where the ions are neutralized via charge exchange reactions with a deuterium or hydrogen gas. This process does not neutralize the complete population and the remaining ions are expelled from the beam by bending magnets; the so-called ion dump. The neutrals are unaffected and continue along their original trajectory into the torus. In the ion source, not only D ions are present, but also D_2^+ and D_3^+. Since they have different mass, they will attain different velocities when they go through the acceleration process, and this will give rise to components of the beam with different energies (E, E/2, and E/3).

As previously described, the neutral beam particles undergo charge exchange with the plasma main ions when injected and this leads to the production of thermal deuterium neutrals. These neutrals will travel a bit before being re-ionized, creating a cloud of thermal deuterium neutrals around the neutral beam called the halo. This halo plays an important role when calculating the impurity density from the measured impurity line emission from charge exchange measurements. This will be described in more detail in the next chapter.

At AUG the NBI system can deliver up to 20 MW of power in deuterium from two different injector systems located on opposite sides of the torus (see figure 2.1) making it the machine's most powerful heating system [19]. Both injector systems are equipped with four beam sources, each of which can provide 2.5 MW of power. Injector 1, also called box 1 with beams Q1 – Q4 (yellow in figure 2.1), has a beam energy for deuterium of 60 keV and injector 2 (box 2), with beams Q5 – Q8 (red in figure 2.1), of 93 keV. The radial sources are Q1 and Q4, the tangential sources are Q2, Q3, Q5, and Q8, and the off-axis sources for current-drive are Q6 and Q7. Apart from heating the plasma, the NBI also serves as a source of neutrals for diagnostic purposes. This will be described in chapter 3.

2.2.2. Electron cyclotron resonance heating

ECRH is a heating method in the micro-frequency range that uses high power electromagnetic waves to transfer energy to the plasma. The collisional absorption of the waves, which happens as the accelerated charged particles collide with the plasma particles, scales as $T_e^{-3/2}$ making it ineffective as a heating method [17]. However, the resonant absorption of the waves is able to produce strong heating. Several different resonant frequencies exist in the plasma and in the case of electron heating the frequencies range from $100-200$ GHz. These resonant waves are absorbed by the electrons, which accelerate and in turn collide with other particles, thus heating the plasma. The absorption location is determined by the electron cyclotron frequency $\omega_{c,e} = eB/m_e$. The waves are only resonant at a given magnetic field B and since the magnetic field depends on the major radius, the deposition of the ECRH power is local, but it can be
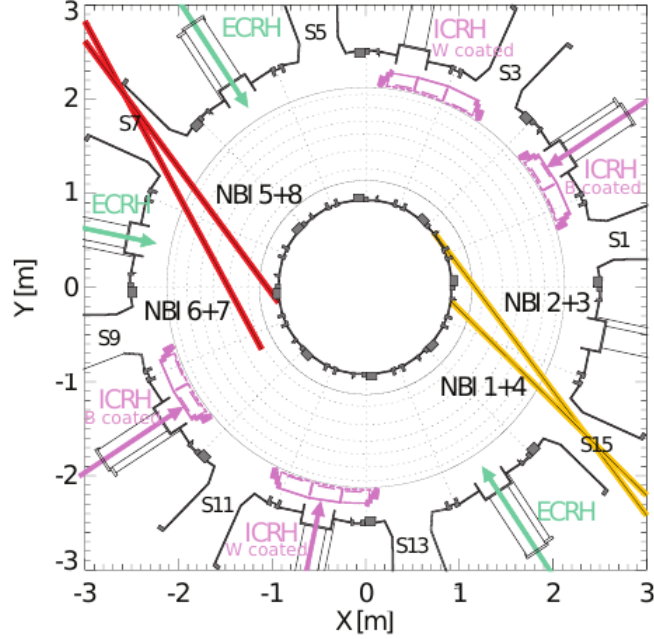
Figure 2.1.: Top-down view of the AUG tokamak displaying its heating systems. The beams from box 1(2) are shown in yellow (red). The ECRH systems are shown in green and the ICRH antennas in purple. Picture taken from [24].

changed by the movement of metal mirrors in the vessel.

AUG has two ECRH systems, each with four gyrotrons making it possible for the systems to provide up to 4 MW of power to the plasma (green in figure 2.1). The two frequency options are 105 GHz or 140 GHz, which correspond to the second harmonics of the electron cyclotron frequency at a magnetic field of -2.0 T and -2.5 T, respectively [20]. Centrally deposited ECRH plays a key role at AUG in avoiding tungsten accumulation [21, 22]. For the experiments performed in this work, centrally deposited ECRH at a frequency of 140 GHz was used unless stated otherwise.

2.2.3. Ion cyclotron resonance heating

A radio frequency heating method is the ICRH, which has the same physical principle as the ECRH, but in this case the target frequency is the ion cyclotron frequency $\omega_{c,i} = ZeB/m_i$, where Z is the ion charge number. This is in the range of 30–120 MHz [17].

At AUG, four ICRH generators each connected to an antenna are installed. Two anntennas are boron coated and two are tungsten coated (purple in figure 2.1). In total, 8 MW of power can be delivered to the plasma [23]. The generators can operate at frequencies of 30 MHz ($B = 2$ T), 36.5 MHz ($B = 2.5$ T), and 40 MHz ($B = 2.7$ T). In deuterium plasmas usually the hydrogen minority heating scheme is used at AUG. The generator frequency used in the experiments in this work was 36.5 MHz. Apart from being a heating source, the ICRH system played a key role in the transport experiments performed in this thesis. This is explained in detail in chapter 5.

2.3. Basic diagnostics

Plasma diagnostics are vital for studying the plasma behavior and its properties. AUG has a broad variety of different diagnostic tools. Two crucial plasma parameters are the electron density and temperature. These can be measured through several different methods, which will be explained in the following two sections. The ion temperature and rotation are two other highly interesting plasma properties. These can be monitored with the charge exchange recombination spectroscopy (CXRS). The whole next chapter is dedicated to this diagnostic method.

2.3.1. Electron density

There are several different diagnostics and methods to determine the electron density at AUG.

Laser interferometry offers line integrated measurements of the electron density and is based on the interaction of an electromagnetic wave with the plasma electrons due to refraction. The refraction index N depends on the electron density:

$$N = \sqrt{1 - \frac{\omega_p^2}{\omega^2}} \text{ with } \omega_p = \sqrt{\frac{e^2 n_e}{m_e \epsilon_0}} \tag{2.1}$$

if the angular frequency of the laser ω ($\omega = 2\pi f$) is higher than the plasma frequency ω_p. A laser beam going through the plasma is phase shifted relative to a reference beam, which does not go through the plasma, and this phase shift $\Delta\phi$ is given by the line integration of the electron density along the length l through the plasma [25]

$$\Delta\phi = \frac{e^2}{2c\epsilon_0 m_e \omega} \int_l n_e dl. \tag{2.2}$$

The DCN interferometry system at AUG is equipped with a deuterium-cyanide laser (DCN) with a wavelength of $195\,\mu\text{m}$, which has 5 horizontal lines-of-sight (LOS) (cyan lines in figure 2.2) and a sampling frequency of $10\,\text{kHz}$ [26].

Lithium beam emission spectroscopy can provide information on the edge electron density [27]. A beam of collimated lithium atoms is injected horizontally into the plasma and the LiI(2p-2s) resonance line at $670.8\,\text{nm}$, which is produced when the neutral lithium atoms collide with the plasma electrons and get excited, can be measured. Because of this, the line emission intensity is dependent on the electron density and can be calculated from the emission profile with the help of a collisional radiative model. Due to the strong attenuation of the beam, measurements of the electron density profile are only possible in the outermost plasma region ($\rho_{pol} > 0.95$). At AUG the lithium beam is injected horizontally above the the midplane (magenta line in figure 2.2) with energies from $30\,\text{keV}$ to $60\,\text{keV}$. The optical head measuring the line emission is equipped with photomultiplier tubes. The spatial resolution is $5\,\text{mm}$. To subtract the background, the beam is chopped meaning it is on for $56\,\text{ms}$ and off for $24\,\text{ms}$ [28].

Thomson scattering (TS) is an active measurement technique for obtaining both the electron density and temperature. It relies on the fact that part of the light from a powerful laser beam is scattered off the electrons in the plasma and can be observed

by polychromators through lines-of-sight perpendicular to the laser. They can measure both the overall intensity and the spectral broadening of the scattered light. The distribution will be a Gaussian, from which the overall intensity is proportional to the electron density and the Doppler width yields the electron temperature [25]. AUG features a core and an edge Thomson system [29] (dashed orange lines in figure 2.2). Four and six high intensity Nd-YAG lasers are operated with a repetition rate of 20 Hz for the core and edge system, respectively. 16 polychromators for the core system and 10 for the edge system are used to detect the scattered laser light.
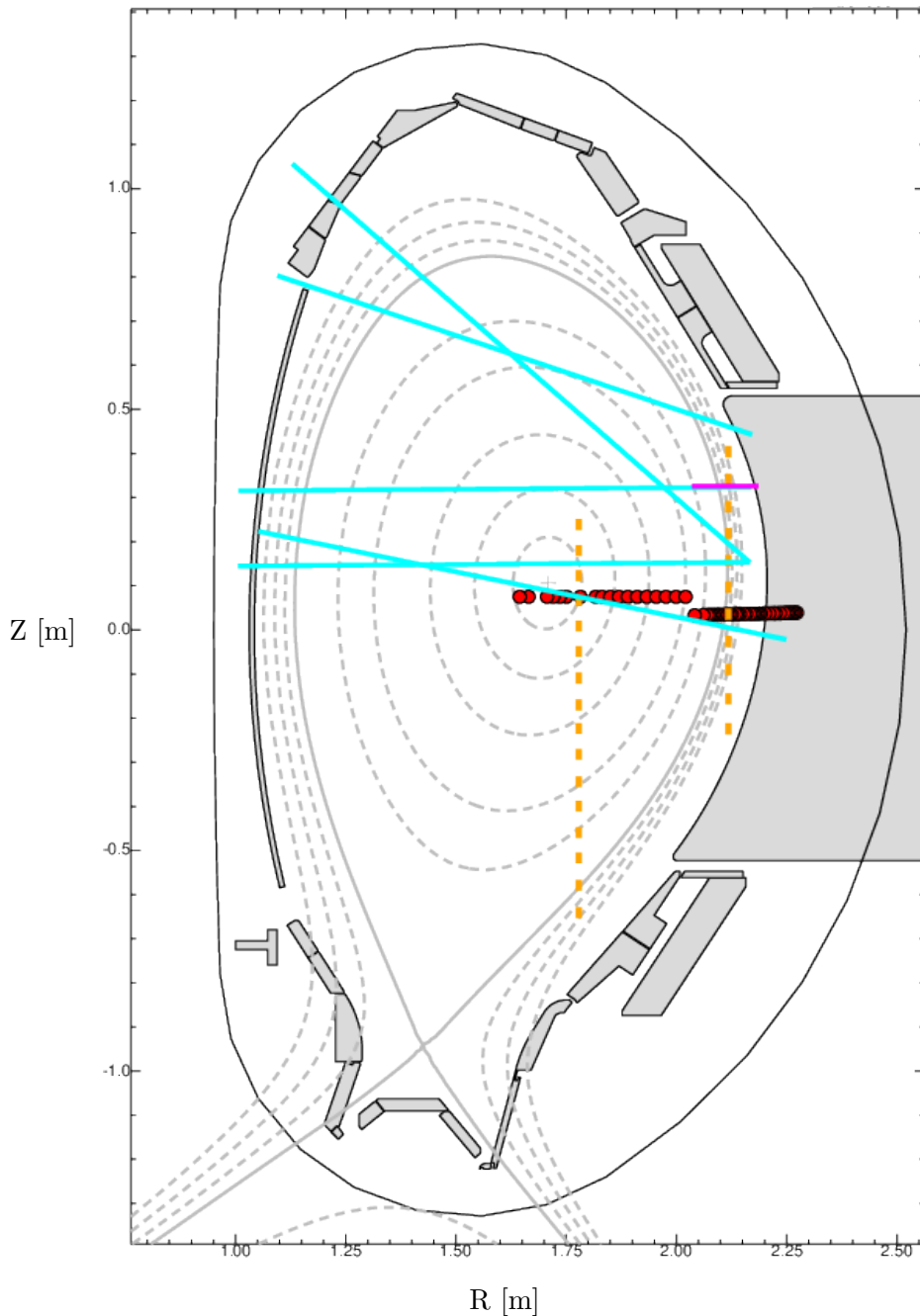
Figure 2.2.: Poloidal cross-section of the AUG tokamak showing some basic diagnostics, which measure the electron density and temperature. The DCN channels are shown in light blue, the edge and core Thomson systems in orange, the ECE system in red, and the lithium beam in magenta.

2.3.2. Electron temperature

Electron cyclotron emission spectroscopy (ECE), which is a passive measuring technique, is effectively the reverse process of ECRH. The electrons gyrating around the magnetic field lines emit cyclotron radiation at the their cyclotron frequency $\omega_{c,e} = eB/m_e$. Since this depends on the magnetic field, which in turn varies with the major radius R, a local measurement of the electron temperature can be obtained. At sufficiently high electron densities the plasma is optically thick at these frequencies and radiates as a black body, which means the Rayleigh-Jeans law can be used to deduce the electron temperature from the intensity of the emitted cyclotron radiation [17]:

$$I = \frac{\omega_{c,e}^2}{8\pi^3 c^2} T_e. \tag{2.3}$$

At AUG, the ECE measurements use a multichannel (60 channels) heterodyne radiometer at frequencies between $89 - 187\,\mathrm{GHz}$, which correspond to magnetic fields from $1.6\,\mathrm{T}$ to $3.4\,\mathrm{T}$ (red dots in figure 2.2). The time resolution is $1\,\mathrm{MHz}$ and the spatial resolution is around $1\,\mathrm{cm}$ [30].

Thomson scattering can, as described in the previous section, also provide measurements of the electron temperature.

Integrated data analysis (IDA) combines measurements of the electron density and temperature from the different systems mentioned above to obtain integrated density and temperature profiles with the use of Bayesian inference analysis [31]. Since different diagnostics measure on different radial and time bases, the measurements are mapped onto a common coordinate and time system. Artifacts in the profiles can arise if the magnetic equilibrium used for the mapping is wrong.

Chapter 3.

Charge exchange recombination spectroscopy

Charge exchange recombination spectroscopy (CXRS) is a diagnostic that measures the ion temperature, flow velocity, and density in tokamaks. The CXRS diagnostic has been the most vital diagnostic for this thesis, and therefore, a complete chapter has been dedicated to it. In this chapter, the basic principle, features of the CXRS spectrum, the calibration procedure, as well as the core CXRS systems at ASDEX Upgrade are described.

3.1. Basic principle

The physical principle of CXRS is, as the name suggests, a charge exchange reaction between an impurity ion A with charge number Z and a neutral particle, in this case a deuterium atom D^0 [32, 33]:

$$A^{Z+} + D^0 \rightarrow A^{(Z-1)+*} + D^+ \rightarrow A^{(Z-1)+} + h\nu + D^+. \tag{3.1}$$
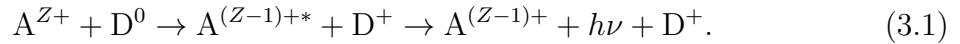
The charge exchange reaction will leave the impurity ion in an excited state $A^{(Z-1)+*}$, which when de-exciting will lead to an emission of a photon $h\nu$ of a characteristic wavelength. This emitted light is measured by the CXRS diagnostic and from the resultant spectrum, the impurity temperature, flow velocity, and density can be deduced. CXRS typically measures the charge exchange between low-Z impurities and the injected neutrals of the NBI. Where the CXRS's lines-of-sight (LOS) intersect the beam line, a localized measurement is obtained. Low-Z impurities are fully stripped throughout the plasma volume and, therefore, enable measurements of a single CX line from the plasma core to the edge. Examples of low-Z impurities that are routinely measured with CXRS are argon, boron, carbon, helium, nitrogen, and oxygen. High-Z impurities are not ideal for CXRS, since they are not fully ionized and normally their concentration is too low for the CXRS measurements. On the left hand side of figure 3.1, an example of a CXRS spectrum measuring the B^{5+} ($7 \rightarrow 6$) line is presented. The line is composed of two different components: the active (magenta) and the passive (blue) signal. The total fit, including both components, is shown in red. The active signal stems from charge exchange reactions with the injected neutrals where the LOS intersect the neutral beam (see schematic drawing on the right hand side of figure 3.1). The passive signal is emitted at the plasma edge and is mainly due to electron and ion impact excitation of the $A^{(Z-1)+}$ ion or charge exchange with the thermal neutral
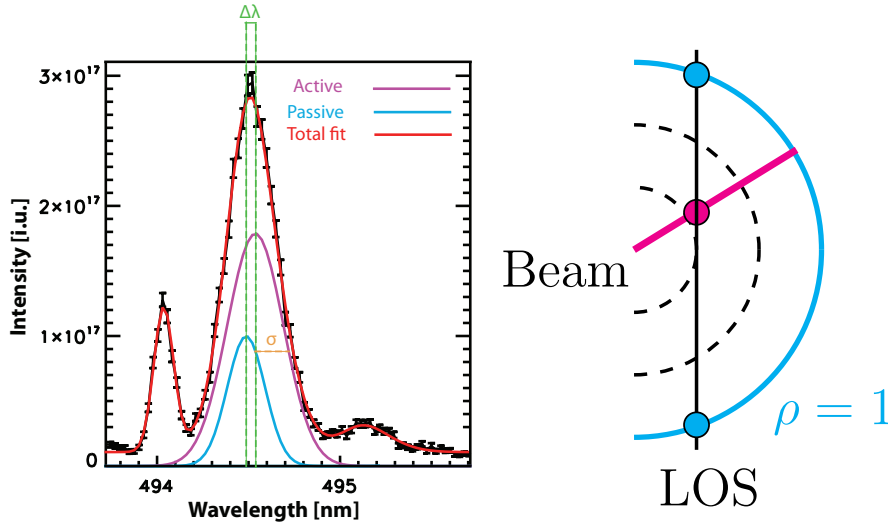
Figure 3.1.: Left: Example of a charge exchange boron spectrum with its active and passive contributions in magenta and blue, respectively. The total fit is shown in red. Right: Schematic drawing showing where the active and passive signals originate from. The intensity unit i.u. = photons/(m^2·sr·nm·s)

deuterium. It is a background to the active signal and, in order to correctly extract local information from the active signal, both must be fitted and the passive signal subtracted. At AUG, the fitting code CXSfit [34] is used to fit the charge exchange spectra.

Assuming the impurity ions are thermalized, that is they have a Maxwellian velocity distribution, the emission line has a Gaussian shape[1]

$$I_{CX,Z}(\lambda) = I_0 \sqrt{\frac{m_\alpha c^2}{2\pi T_\alpha \lambda_0^2}} \cdot \exp\left(-\frac{m_\alpha c^2}{T_\alpha} \frac{(\lambda - \lambda_0)^2}{\lambda_0^2}\right), \tag{3.2}$$

where $I_{CX,Z}$ is the line shape function, I_0 is the measured maximum of the radiance, m_α and T_α the mass and temperature of the species α, λ_0 the theoretical wavelength of the measured line, and c the speed of light. The temperature T_α is determined from the Doppler broadening of the spectral line and it is proportional to the width of the distribution (marked as σ in figure 3.1):

$$T_\alpha = \frac{m_\alpha c^2}{\lambda_0^2} \cdot \sigma^2. \tag{3.3}$$

We assume $T_\alpha \approx T_i$ since the energy equilibration time between impurities and main ions is short compared to local transport time scales. Therefore, the deduced temperature is equivalent to the main ion temperature T_i.

From the Doppler shift of the wavelength ($\Delta\lambda$ in figure 3.1), the flow velocity $\vec{v}_{rot,\alpha}$ of the impurity α projected onto the LOS can be calculated:

$$\frac{\Delta\lambda}{\lambda_0} = \frac{\vec{v}_{rot,\alpha} \cdot \vec{e}_{LOS}}{c}, \tag{3.4}$$

---

[1] Temperatures are given in eV.

where $\vec{e}_{LOS}$ is the unit vector along the LOS.

Finally, the relation between the measured line intensity $I_{CX,Z}$ and the impurity density n_Z is the following:

$$I_{\text{CX,Z}}(\lambda) = \frac{h\nu}{4\pi} \sum_i \sum_j \langle \sigma v \rangle_{i,j} \int_{LOS} n_{\text{Z}} n_{0,i,j}(l) \mathrm{d}l, \qquad (3.5)$$

where $h\nu$ is the energy of the photon, $\langle \sigma v \rangle_{i,j}$ is the effective CX emission rate coefficient for a given spectral line λ with the neutral population from the beam $n_{0,i,j}$ for a given beam energy component i and a given principle quantum number j of the beam. If one assumes that the impurity density is constant along the intersection of the LOS and the beam volume, n_Z can be taken out of the integral and equation (3.5) becomes:

$$n_{\text{Z}} = \frac{4\pi}{h\nu} \frac{I_{\text{CX,Z}}(\lambda)}{\sum_i \sum_j \langle \sigma v \rangle_{i,j} \int_{LOS} n_{0,i,j}(l) \mathrm{d}l}. \qquad (3.6)$$

How the impurity density is calculated at AUG is described in more detail in section 3.5 below.

3.2. CXRS systems at ASDEX Upgrade

AUG features several different CXRS systems covering both the core and the edge of the plasma, including both the low field side (LFS) and high field side (HFS) [35, 36]. For this work, the core systems have been the most important ones, and, therefore, they will be described in the following. A top-down overview of the geometry of the two core systems can be seen in figure 3.2. In total, these systems have 72 LOS that are used for CXRS and a typical integration time of 10 ms [35, 36]. The two core systems are located on opposite sides of the torus and, hence, view two different NBI sources, with beam energies of 60 keV (Q3 in box I shown in green in figure 3.2) and 93 keV (Q8 in box II shown in magenta in figure 3.2). The spatial and maximal temporal resolution of the system utilizing the 60 keV beam are $1.0 - 2.5$ cm and 3.5 ms [35], while for the system utilizing the 93 keV beam they are $1.0 - 1.5$ cm and 2.5 ms [36]. The core system viewing Q8 features two identical spectrometers, called COR and CUR, each measuring 25 LOS. A top-down picture of one of these spectrometers is shown on the left hand side of figure 3.3. The light collected by each optical head is transmitted by $400\,\mu$m optical fibers and guided into one of the spectrometers. The optical fibers are stacked vertically in front of a variable entrance slit of the spectrometer. The incoming light is parallelized onto the grating using a Lecia lens with a focal length of 280 mm. The grating itself has 2400 grooves/mm and its angle position can be changed via a sine drive. After the grating, the diffracted light is refocused by a second Lecia lens with a focal length of 180 mm, before entering the Princeton Instruments ProEM CCD camera [37]. The CCD chip is 512×512 $16\,\mu$m big and the maximal readout frequency of the camera is 10 MHz. Each LOS/fiber has a defined region in pixel space on the chip, which will be referred to as channel.
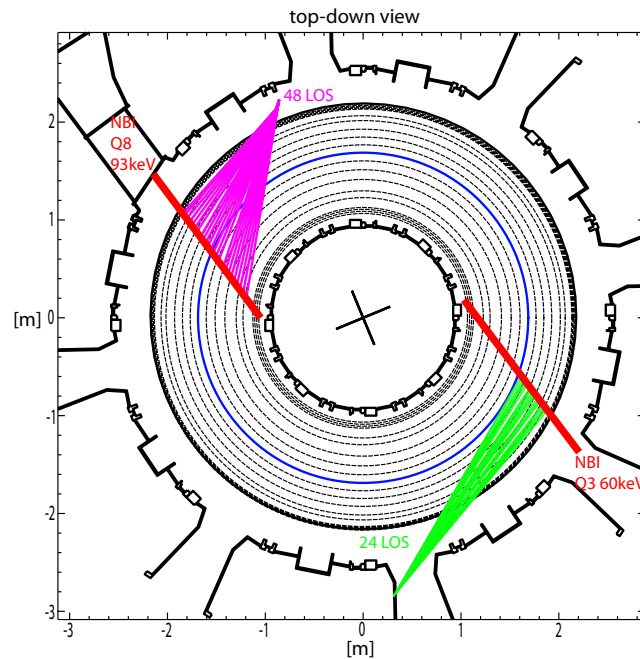
Figure 3.2.: Top-down view of the core CXRS systems at AUG. The core system viewing source Q3 in beam box I is displayed in green and the one viewing source Q8 in beam box II in magenta.
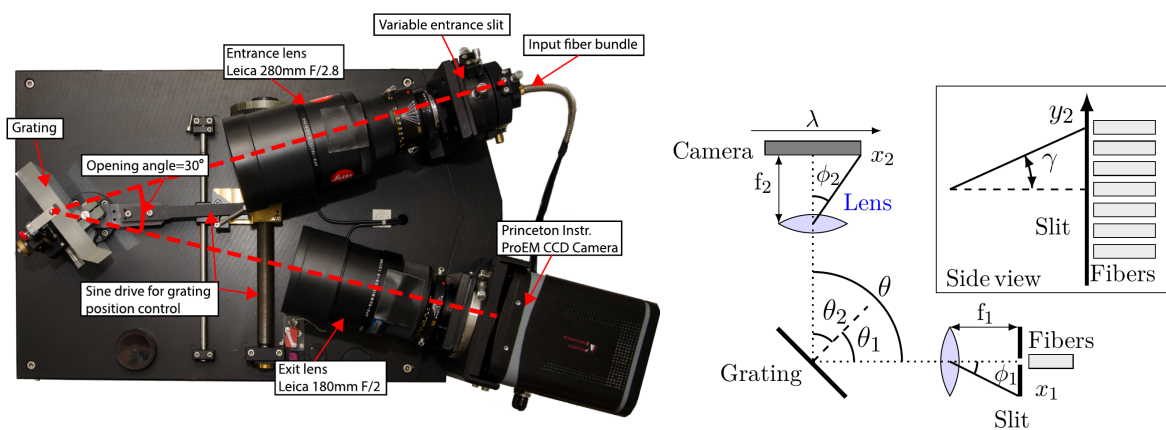

Figure 3.3.: Left: Top-down picture of one spectrometer of the core systems. Right: Schematic top-down view of the Czerny-Turner spectrometer.

3.3. System calibrations

To gain precise knowledge about the impurity ion temperature, flow velocity, and density the system must be absolutely calibrated. These calibrations include wavelength calibration, instrument functions of the spectrometers, and the absolute intensity calibration of the entire system, and will be described in this section.

3.3.1. Wavelength calibration

A precise wavelength calibration is needed to accurately determine the flow velocity. The grating equation of the Czerny-Turner spectrometer is given by the wavelength axis of the spectrometer [38]:

$$ng\lambda = \cos\gamma\sin(\theta_1 + \phi_1) + \sin(\theta_1 + \phi_1). \tag{3.7}$$

In equation (3.7), n is the diffraction order, g is the number of grooves/mm of the grating, and λ is the wavelength. The quantities describing the geometry of the spectrometer are γ, which is the vertical angle, θ_1 and θ_2, which are the incident and diffraction angles, and ϕ_1 and ϕ_2, which are the horizontal angle of the entrance slit and the image plane. These quantities are depicted on the right hand side of figure 3.3 along with the horizontal distances x_1 and x_2 from the optical axis to the slit plane and to the image plane, respectively. Furthermore, these horizontal distances can be defined as $\tan\theta_1 = x_1/f_1$ and $\tan\theta_2 = x_2/f_2$, where f_1 and f_2 are the foci of the entrance and exit lenses, respectively. The chosen geometry and grating define the central wavelength λ_0 at the optical axis ($\gamma = \phi_1 = \phi_2 = 0$):

$$\lambda_0 = \frac{\sin\theta_1 + \sin\theta_2}{ng}. \tag{3.8}$$

By differentiating the grating equation (3.7) with respect to x_2 for a fixed central wavelength one obtains the dispersion relation:

$$\frac{\partial\lambda}{\partial x_2} = \frac{\lambda_0}{f_2}\frac{\cos\gamma\cos(\theta_2 + \phi_2)\cos^2\theta_2}{\sin\theta_1 + \sin\theta_2}. \tag{3.9}$$

The image of the vertical slit on the image plane for one emission line, thus, has a parabolic shape because of the dependence of the wavelength λ on the vertical displacement of the fibers away from the optical axis γ, which can be seen on the left of figure 3.4. Assuming small angles ($\gamma \ll 1$ and $x_2 \ll f_2$) and performing a Taylor expansion up to the second order of equation (3.7) results in:

$$x_2 = \frac{\sin\theta_1 + \sin\theta_2}{2f_2\cos\theta_2}y_2^2, \tag{3.10}$$

hence, the parabolic shape ($x_2 \sim y_2^2$). The different spectrometer channels are connected to each other through this parabola. Additionally, small displacements and damages to the fibers can result in deviations from this curve (black crosses in figure 3.4), and these displacements have to be determined at different wavelengths. By measuring multiple lines at different wavelengths, the parabola for the spectrometer can be deduced. Neon lamps have been used to measure the exact wavelength position
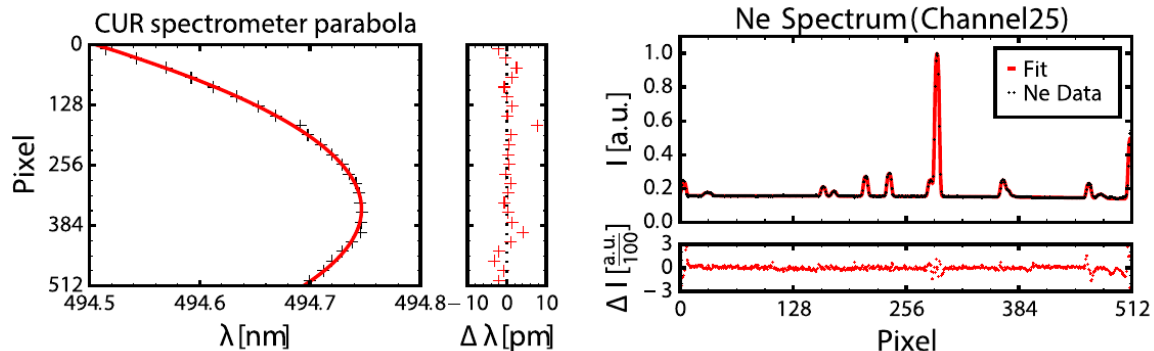
Figure 3.4.: Left: Parabola of the CUR spectrometer at 494.498 nm. Theoretical position in red and measured positions in black crosses. Right: Measured neon spectrum at 495 nm with fit shown in red.

for each channel. To reduce systematic errors, an additional calibration is performed after every plasma discharge. This accounts for possible air temperature or pressure changes which can affect the wavelength calibration or for mechanical uncertainties of the sine drive. A neon lamp is automatically switched on after every discharge on one dedicated channel and the measured spectrum is fitted. Such a fit is displayed on the right of figure 3.4. More importantly, this enables the wavelength, i.e. the measured impurity, to be changed on a shot-to-shot basis while still maintaining a precise wavelength calibration.

3.3.2. Instrument function

The entrance slit in front of the fibers of the spectrometer has a finite width, which leads to the instrumental broadening; hence, the measured line shape is a convolution of the Doppler broadening and the instrument function, and to correctly determine the ion temperature the instrument function must be well known. To find a balance between the amount of light collected and the width and shape of the instrument function, the width of the entrance slit is changeable. The chosen slit width is about $100 \, \mu$m. The instrument functions for the core systems are not perfectly described by a single Gaussian (see figure 3.5). But it was found that the measured line broadening is dominated by the Doppler broadening, hence, no significant difference in the measured velocities and temperatures have been observed when using a Gaussian approximation of the instrument function. For the sake of accuracy of the complete wavelength calibration for every individual channel, however, the exact instrument function, that is its non-Gaussian line shape, is taken into account.

3.3.3. Intensity calibration

The absolute intensity calibration enables the conversion from the measured counts of the line intensity to photons for every wavelength. Only when the number of photons is known, can the absolute impurity density be calculated. These calibrations are performed with an Ulbricht sphere, which is a spherical integrating light source with
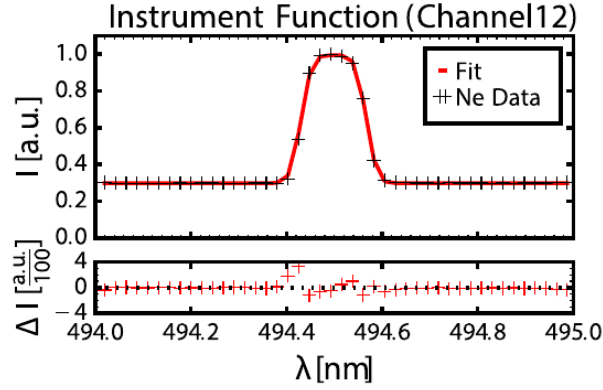
Figure 3.5.: Non-Gaussian shaped instrument function at 494.498 nm of channel 12 of the COR spectrometer.

known radiance as a function of wavelength. The spectral radiance of the sphere can be seen in figure 3.6a. First, each channel of the spectrometer is calibrated, which is connected to the optical head fibers. By scanning the wavelength from 400 nm to 700 nm and measuring the resulting count rates a radiance curve for each fiber is obtained (see figure 3.6c). Second, the sphere is placed in front of each optical head in the vessel and the measurement procedure is repeated. The radiance curve of an optical head fiber can be seen figure 3.6b. This can only be done when we have access to the torus which means before and after each experimental campaign. The dip seen at 600 nm in figure 3.6b is caused by fiber absorption at this particular wavelength. In this manner, the whole system is cross-calibrated meaning that channels can be interchanged without the need to redo the calibrations and also changes in the calibrations can be isolated to either the in-vessel optical head fibers or the spectrometer fibers. By comparing the radiance curve of the optical head fibers with the spectrometer fibers, a transmission curve of the in-vessel optics and relay fibers can be obtained for every LOS. The transmission have a small wavelength dependence and varies from 40 % at 400 nm to 60 % at 650 nm, which can be seen in figure 3.6d. Over the course of the campaign, the optical in-vessel components deteriorate, which normally results in a lower radiance measured at the end of the campaign compared to the beginning of the campaign. This is typically on the order of 10 %.

3.4. Corrections to CXRS measurements

Atomic effects may affect the charge exchange spectra and can cause small errors in the measurements if they are not properly taken into account. These include the charge exchange cross-section effect, the gyro-motion effect, and corrections due to Zeeman splitting. These different effects will be described in the following.

The fact that the charge-exchange cross-sections are energy dependent gives rise to an apparent wavelength shift and line broadening of the spectrum that are not associated with the true ion temperature and velocity [39]. Ions moving towards the beam have a slightly higher collision velocity than ions moving away from the beam.
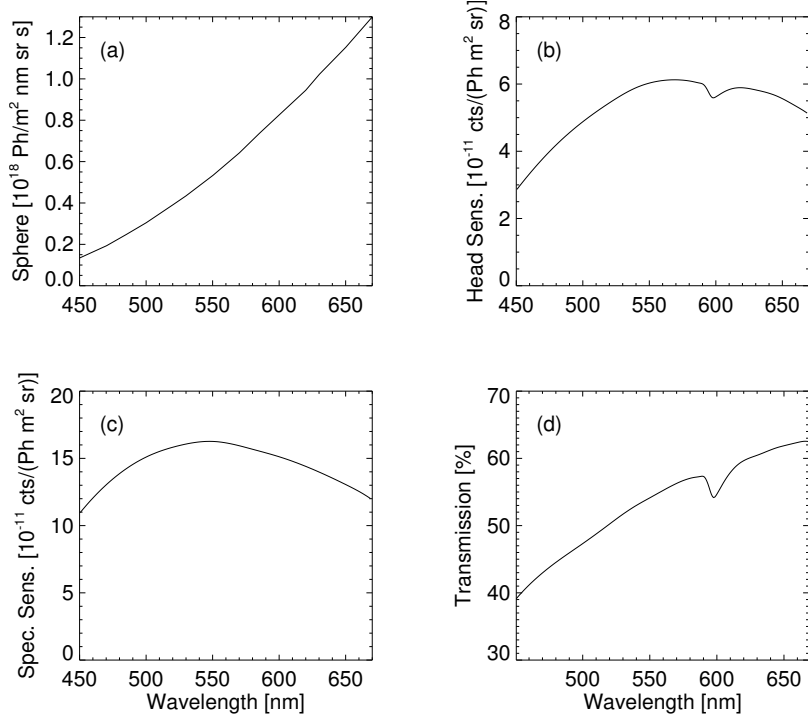
Figure 3.6.: (a) Spectral radiance of the Ulbricht sphere used for the intensity calibrations. (b) Intensity calibration of the in-vessel optical fibers and (c) of the corresponding spectrometer channels. (d) The transmission resulting from (b) and (c).

These ions, therefore, sample different regions of the energy-dependent charge-exchange cross-section and, therefore, have different probability to undergo a charge exchange reaction. This effect can distort the measured spectra by increasing the observed line intensity on one side of the spectrum, while it is decreased on the other side. The extent of the distortion depends on the beam geometry, the beam injection energy, and the ion temperature. For typical AUG plasmas ($T_i < 5\,\mathrm{keV}$), this effect is normally smaller than $2\,\%$ and have, thus, been neglected in the analysis.

An additional atomic effect, called the gyro-motion effect [40], can also distort the spectra. In the charge exchange process, the impurity ion will interact with the beam neutrals and end up in an excited state. This excited state has a finite lifetime τ, and before the impurity ion de-excites and emits a photon it will gyrate a distance $\omega\tau$. Therefore, an apparent vertical velocity arises, which will depend on $\omega\tau$, and this will cause a line shift. Since the LOS for the core diagnostics are almost parallel to the magnetic field lines within the beam volume, the gyro-orbit effect can be neglected in this analysis.

The Zeeman effect [41] causes a splitting of a spectral line into several components in the presence of a magnetic field. These components have shifted wavelengths and all of them together result in a line which is still Gaussian, but with a broader line shape. This leads to an overestimation of the ion temperature if not corrected for. The measurements from the AUG CXRS diagnostics employ correction curves to account for the Zeeman effect. After the CXRS data is fitted for the apparent temperature, the true temperature is deduced by interpolating along these curves. This is routinely
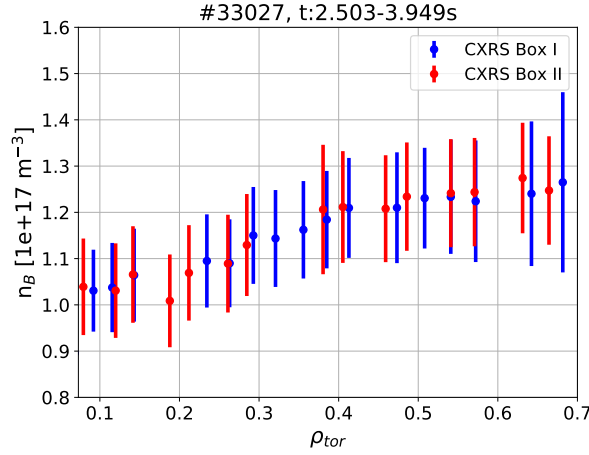
Figure 3.7.: Steady-state boron density profile for the two CXRS core diagnostics. The profile from box I was multiplied by a factor of 0.88.

done for all AUG CXRS diagnostics.

3.5. Impurity density

The calculation of the impurity density through equation (3.6) has been performed with the in-house CHICA code [42]. To calculate the impurity density, CHICA takes the electron density, electron temperature, ion temperature, the measured CXRS line intensity, and the plasma equilibrium as inputs. The resultant impurity density profile depends strongly on these input profiles, especially the electron density, hence they have to be well known. Another important factor for the calculations is the geometry of the beams. The beam geometries have been constrained using beam emission spectroscopy (BES) measurements with different LOS as well as thermal images of the beam impact points on the inner wall. The cross-check of the calculated impurity density profiles between the CXRS systems on box I and box II, which have different geometries and energy components, provides confirmation that these calculations are done correctly. Differences in absolute magnitude of $10-20\%$ are often seen between the diagnostics and are attributed to calibration errors and unavoidable deterioration of the in-vessel optical components during the experimental campaign. However, for transport analyses it is the gradient, e.g. the profile shape, that is important and, as can be seen in figure 3.7 and Ref. [36], both systems reproduce the same profile shapes. Note that in figure 3.7, a correction factor of 0.88 was applied to the NBI box I CXRS system to match the absolute value of the impurity density profiles. Linear fits of the two datasets in the radial window $\rho_{tor} = 0.4-0.6$ are performed and the correction factor is determined from the ratio of the radial averages of the two linear fits. This is a standard method for combining the two datasets.

The neutrals in the beam have three different energy components ($i = 1,2,3$) as well as a halo ($i = 4$ in equation (3.6)). Furthermore, the beam and the beam halo can be in different excited states j. The beam halo atoms is a cloud of deuterium neutrals around the injected neutral beam, which are produced from charge exchange interac-

tions between the injected neutral particles and the thermal plasma deuterium ions. The neutral beam densities $n_{0,i,j}$ in equation (3.6) can be indirectly measured with beam emission spectroscopy (BES) or calculated with a beam attenuation code. Three different beam attenuation codes are currently implemented in CHICA: FIDASIM [43], FAST and COLRAD. All three codes use the same beam geometries, but are differently implemented. The product of two Gaussians are used to describe the fall-off of the neutral density perpendicular to the beam in the COLRAD and FAST codes. To account for the beam divergence, the Gaussians are described by vertical and horizontal widths, which increase as a function of distance along the beam. In FIDASIM, fixed beam divergences and foci of the particle distributions are used to describe the beam geometry. FIDASIM is a Monte Carlo code which simulates the whole D_α spectrum and as a part of this simulation, it calculates the neutral densities of all beam energy components in the first four excited states. Since FIDASIM is a Monte Carlo code, it is computationally expensive and too time consuming too run for a whole discharge.

The other beam attenuation codes featured in CHICA are two pencil codes called FAST and COLRAD. As described above both codes use the same beam model, but COLRAD calculates the halo population more properly than FAST, which has turned out to be crucial for determining the right shape of the impurity density profile. Additionally, the physics implemented in FAST is a bit reduced compare to COLRAD and FIDASIM. For example, FAST only calculates the neutral density in the $j = 1,2$ states and it does not include electron impact excitation when estimating the beam attenuation along the beam line.

COLRAD solves the collisional radiative model for the beam and halo neutrals of each energy component. All calculations are performed along the beam line, hence the name pencil code, and are then extended perpendicularly outwards with the Gaussian description mentioned above. By solving a system of coupled rate equations, COLRAD can calculate the neutral density in the states with principal quantum number $j = 1 - 10$. The collisional rate coefficients are given by excitation, de-excitation, and ionization by electron, hydrogen, and impurity ion impact, and charge-exchange reactions with impurities and main ions. The source of the j-th state of halo neutrals in COLRAD stems from the losses caused by charge-exchange of the beam with the main ion background. From the equilibrium solution of the collisional radiative model, the source of the halo neutrals in the j-th level is calculated. For each position along the beam path, the characteristic fall-off length for charge exchange and ionization reactions of the halo cloud are calculated. To then decide the extent and shape of the halo population perpendicular to the beam path, the relative strength of these two processes is used.

The different codes have been thoroughly benchmarked against one another and the BES. Through this benchmark it has become clear how important a correct estimation of the halo cloud is for the final impurity density profile. FIDASIM and COLRAD agree well with each other and the discrepancies seen for FAST is mainly due to the simplified halo calculation. In this work, mainly COLRAD has been utilized to calculate the neutral density, since it handles the halo more properly than the FAST code and it is significantly faster than FIDASIM. But to check that COLRAD and FIDASIM deliver the same neutral density and impurity density profile, FIDASIM has been run for a limited time window for each profile.

After the neutral density is calculated it is multiplied with the effective charge exchange emission rate $\langle \sigma v \rangle$ for a given spectral line. The charge exchange emission rates are derived from the cross-section data from the ADAS database [44]. Cross-sections are used that include cascade processes from higher excited states down to the energy level of the sought transition. To obtain an effective charge exchange emission rate, one has to integrate over the velocity space and then divide by the relative velocity of the neutrals and the impurities:

$$\langle \sigma v \rangle = \frac{\int\limits_{-\infty}^{\infty} \mathrm{d}\vec{v}_1 \int\limits_{-\infty}^{\infty} \mathrm{d}\vec{v}_2 \exp\left(\frac{-m\vec{v}_1^2}{2T}\right) \delta(\vec{v}_2)\sigma(v)v}{\int\limits_{-\infty}^{\infty} \mathrm{d}\vec{v}_1 \int\limits_{-\infty}^{\infty} \mathrm{d}\vec{v}_2 \exp\left(\frac{-m\vec{v}_1^2}{2T}\right) \delta(\vec{v}_2)}. \tag{3.11}$$

In equation (3.11), $v = |\vec{v}_1 - \vec{v}_2|$ denotes the relative velocity between the beam neutral $\vec{v}_2$ and the impurity $\vec{v}_1$. The velocity of the impurity follows a Maxwellian distribution. Equation (3.11) is for beam impact charge exchange, hence the delta function which represents the velocity distribution of the beam. For the halo we deal with thermal-thermal charge exchange impact which means that the delta function in equation (3.11) is replaced by a Maxwellian velocity distribution of the halo population. $\langle \sigma v \rangle$ is an average over the velocity distribution, hence, the denominator in equation (3.11). The effective charge exchange emission rates vary for the different energy components and excited states of the beam neutrals. Even though the $j = 2$ populations of the beam and halo neutrals are smaller than the ground state one, the effective charge exchange emission rate is bigger resulting in that the $j = 2$ population has a non-negligible effect on the overall impurity density. The $j = 2$ effective charge exchange emission rates are orders of magnitude bigger than the ground state rates. In the end, the far most significant contribution to the calculated impurity density comes from the first energy component in the $j = 1$ state, which provides $45 - 60\%$ and $55 - 75\%$ of the total signal for the 60 keV beams and 93 keV beams, respectively. The second largest contribution stems from the halo in the $j = 2$ state, adding up to $15 - 35\%$ for the 60 keV beams and $10 - 20\%$ for the 93 keV beams. Depending on which plasma parameters we are operating at, the second energy component in the ground state adds up to 15% for the 93 keV beam. All the other populations contribute less than 10% to the total calculated impurity density. Since there are no charge exchange cross-sections in the $j = 3$ state accessible, the neutral populations in this state are not calculated. These populations are, however, estimated to have a very small impact on the total impurity density, probably even within error bars.

Note that in equation (3.6) the impurity density is assumed to be constant along the intersection of the LOS and the neutral beam volume. This assumption is well met in the plasma core where the gradient lengths are small, but is not valid for the CXRS LOS that intersect the edge pedestal inside of the beam volume, where we have strong gradients and LOS geometries which are not tangential to the flux surfaces. This is the case for the outermost LOS of both core systems ($\rho_{tor} > 0.85$). For these LOS, special analysis is required that has not been performed here and to avoid any effect of uncertain gradient on the profiles, the analysis region is restricted to $\rho_{tor} < 0.75$.

3.5.1. Uncertainties on the impurity density

The calculation of the experimental boron density via equation (3.6) is subjected to several different uncertainties. The first one is the error on the measured CXRS line intensity, which is well known and characterized. The second one is the uncertainty on the atomic data that goes into the effective charge exchange emission rates $\langle \sigma v \rangle$, which is estimated at $15-20\%$. The effective emission rates are dominated by the interaction energy, which is constant in our case, and do only vary weakly with the electron density, the ion, and the electron temperatures. Changes due to the electron density, the ion, and the electron temperatures along the beams are minimal and, therefore, this uncertainty does not significantly impact the error on the overall profile shape, which is of interest in our case. The third and final one is the uncertainty in the determination of the neutral beam density. This in turn depends on the uncertainties of the beam stopping rates, the beam geometry as well as the measured electron density. The same argument as above applies to the beam stopping rates, i.e. they do not significantly affect the profile shape error bar and have, therefore, been neglected. The beam geometry is well diagnosed and benchmarked for the two different NBI systems by cross-checking that the same answer is obtained when using different beam combinations. The electron density n_e has the biggest impact on the attenuation of the neutral beam. If the standard deviation on the electron density was known, this uncertainty could be added to the overall uncertainty on the neutral beam density. However, the electron density is deduced from an integrated data analysis (IDA) framework [31], where the measured electron densities from several different diagnostics have been combined into one profile using Bayesian inference and this procedure does not produce a standard deviation, but rather confidence bands on the electron density, which cannot be used in a standard error propagation scheme. Therefore, this last source of error is not routinely included in the overall uncertainty on the impurity density.

3.6. Conclusion

In this chapter the basic principle of the CXRS diagnostic was explained along with the description of the core CXRS systems at AUG and the calibration procedures. The main quantity of interest for this work is the impurity density and the last section gave a detailed explanation to how this can be calculated from the measured line intensity. The framework of deriving the boron transport coefficients, which will be described in chapter 5, heavily rely on the shape of the boron density profile. If this is not correctly calculated the deduced transport coefficients will be wrong. The shape of the profile is also important when calculating the normalized boron density gradient. In the next chapter, the equation connecting the parameters describing the transport, that is the transport coefficients, with the measured impurity density will be presented. This equation is the foundation on which all further analysis of this thesis stands. Furthermore, an introduction to the theory of particle transport in tokamak plasmas will be given as well as a summary of the present status of the field of impurity transport.

Chapter 4.

Impurity transport

The helical magnetic field in a tokamak confines the plasma particles. In an ideal case these particles would only move along these magnetic field lines and, hence, stay confined in the plasma. However, in real plasmas cross-field transport occurs due to two main sources: collisions and turbulence. Collisions cause friction between the different plasma species. Classical transport is the transport which is driven by friction forces perpendicular to the magnetic field and neoclassical transport refers to the transport stemming from the friction forces along the curved magnetic field lines given by the toroidal geometry. Turbulent transport, on the other hand, arises from micro-instabilities in the plasma. The magnitude of the radial transport determines the confinement properties of the plasma and, therefore, the understanding of the underlying transport processes is of utmost importance for the future development of a nuclear fusion reactor.

In this chapter, we will start with a short derivation of the radial transport equation, which is the basis for all further analysis of this thesis, and then continue with a quick overview of the theory of particle transport including, classical, neoclassical and turbulent transport. This is followed by a brief review of the present status of the impurity transport field. At the end of the chapter, how plasma instabilities effect impurity transport will shortly be addressed.

4.1. The radial impurity transport equation

The integral form of the conservation law of particle density n_Z of an impurity in an ionization stage Z reads

$$\frac{\partial}{\partial t} \int_V n_Z \mathrm{d}V = - \oint_{\partial V} \vec{\Gamma} \cdot \mathrm{d}\vec{\mathcal{S}} + \int_V \mathcal{S} \mathrm{d}V \qquad (4.1)$$

for any volume V. In this context V denotes the volume inside an arbitrary flux surface ∂V. $\mathcal{S}$ is the source and sink term, which is comprised of processes such as ionization, recombination, and charge exchange between neighboring charge states and Γ is the particle density flux. We are interested in the transport perpendicular to the magnetic flux surface, the so-called radial transport, since the much faster transport parallel to the magnetic field causes practically a constant density n_Z on a magnetic flux surface. The following derivation of a flux surface average of equation (4.1) follows the steps in Ref. [13]. We will label the flux surfaces by the coordinate r, which is defined as:

$$r = \sqrt{\frac{V}{2\pi^2 R_{axis}}}, \qquad (4.2)$$

where, again, V is the volume enclosed by the flux surface and R_{axis} is the major radius. This definition will allow us to express the transport equation in cylindrical coordinates and we, thus, approximate the plasma to be circular. Furthermore, the unit vector $\vec{r} \equiv \nabla r / \|\nabla r\|$ is defined normal to the flux surface pointing outward from the enclosed volume. The surface integral of the flux density then becomes:

$$\oint_{\partial V} \vec{\Gamma} \cdot \mathrm{d}\vec{\mathcal{S}} = \oint_{\partial V} \vec{\Gamma} \cdot \nabla r \frac{\mathrm{d}\mathcal{S}}{\|\nabla r\|}. \tag{4.3}$$

The flux surface average for an arbitrary scalar quantity $\mathcal{F}$ is given as

$$\langle \mathcal{F} \rangle = \left(\frac{\partial V}{\partial r} \right)^{-1} \oint \mathcal{F} \frac{\mathrm{d}S}{\|\nabla r\|}. \tag{4.4}$$

Using equation (4.4) and

$$\int_V \mathcal{F} \mathrm{d}V = \int_0^r \left(\frac{\partial V}{\partial r} \right) \langle \mathcal{F} \rangle \mathrm{d}r, \tag{4.5}$$

equation (4.1) now takes the following form:

$$\frac{\partial}{\partial t} \int_0^r \mathrm{d}r n_Z \left(\frac{\partial V}{\partial r} \right) = - \left(\frac{\partial V}{\partial r} \right) \langle \vec{\Gamma} \cdot \nabla r \rangle + \int_0^r \mathrm{d}r \left(\frac{\partial V}{\partial r} \right) \mathcal{S}. \tag{4.6}$$

By differentiating equation (4.6) with respect to r and using the definition of r in equation (4.2), we arrive at:

$$\frac{\partial n_Z}{\partial t} = -\frac{1}{r} \frac{\partial}{\partial r} r \langle \vec{\Gamma} \cdot \nabla r \rangle + \mathcal{S}. \tag{4.7}$$

The Ansatz for the radial particle flux density Γ is comprised of a diffusive and a convective part:

$$\Gamma = -D(\theta) \|\nabla r\| \frac{\partial n_Z}{\partial r} + v(\theta) n_Z, \tag{4.8}$$

where $D(\theta)$ is the radial diffusivity and $v(\theta)$ the radial convection or drift velocity, both of which depend on the poloidal angle θ. These two quantities characterize the particle transport. The diffusion coefficient is a strictly positive quantity with units $\mathrm{m^2/s}$. The drift velocity can take both positive and negative values and the convention is that $v < 0$ corresponds to an inward drift, hence leading to a peaked density profile. The opposite: $v > 0$ leads to an outward drift and a hollow density profile. Evaluating the product $\vec{\Gamma} \cdot \nabla r$ now yields:

$$\vec{\Gamma} \cdot \nabla r = -D(\theta) \|\nabla r\|^2 \frac{\partial n_Z}{\partial r} + v(\theta) \|\nabla r\| n_Z. \tag{4.9}$$

By substituting equation (4.9) into equation (4.7) we finally arrive at the radial transport equation:

$$\frac{\partial n_Z(r,t)}{\partial t} = \frac{1}{r} \frac{\partial}{\partial r} r \left(D^*(r) \frac{\partial n_Z(r,t)}{\partial r} - v^*(r) n_Z(r,t) \right) + \mathcal{S}. \tag{4.10}$$

D^* and v^* are, thus, flux surface averaged transport coefficients:

$$D^* = \langle D(\theta) \| \nabla r \|^2 \rangle \tag{4.11}$$

$$v^* = \langle v(\theta) \| \nabla r \| \rangle. \tag{4.12}$$

For the sake of readability, the asterisk will be omitted from now on. The source and sink term $\mathcal{S}$ connects the transport equation of each ionization stage Z with the neighboring stage as follows:

$$\mathcal{S} = -(n_e S_Z + n_e \alpha_Z + n_0 \alpha_Z^{cx}) n_Z + n_e S_{Z-1} n_{Z-1} + (n_e \alpha_{Z+1} + n_0 \alpha_Z^{cx}) n_{Z+1}, \tag{4.13}$$

where S_Z is the impurity ionization rate into the ionization stage Z, α_Z is the recombination coefficient for stage Z for radiative and di-electronic recombination, and α_Z^{cx} is the recombination coefficient for charge exchange with the neutrals n_0. All source terms in (4.13) will cancel out except for the ionization and recombination between the neutrals and the singly ionized ion when summing the transport equation (4.10) for all ionization stages, which results in a transport equation that is independent of the charge stage. The transport coefficients D and v are thus averaged coefficients for each ion stage weighted by the fractional abundance of each stage.

In this work, the core transport ($\rho_{tor} < 0.8$) of the non-recycling, low-Z impurity boron ($Z = 5$), which is fully ionized inside the last closed flux surface, is studied. As will be described in the next chapter, the exact nature of the boron source term is not fully understood. Motivated by the steady-state analysis in Ref. [45], it is more feasible to describe the source term in a time independent steady-state such that it becomes a boundary condition on equation (4.10) rather than an unknown function (this will be described in more detail in the next chapter). In this case, the transport equation reduces to:

$$\boxed{\frac{\partial n_Z(r,t)}{\partial t} = \frac{1}{r}\frac{\partial}{\partial r} r \left(D(r)\frac{\partial n_Z(r,t)}{\partial r} - v(r) n_Z(r,t) \right), \quad n_Z(r_{\max}, t) = s(t),} \tag{4.14}$$

where $s(t)$ is the impurity density boundary condition at the edge at $r_{\max}$.

Setting the time derivative in equation (4.14) to zero, that is the impurity density does not vary in time, the equation reduces to the steady-state equation:

$$\frac{1}{n_Z}\frac{\partial n_Z}{\partial r} = \frac{v}{D}. \tag{4.15}$$

Here we can find, for any given n_Z and D, a v such that equation (4.15) is fulfilled, which means that the problem of finding v and D given n_Z is ill-posed. Hence, with only a time-independent impurity density signal at hand separate information on the transport coefficients cannot be obtained. As will be described in the next chapter, we do indeed have a method of obtaining time-dependent information and the aim of this thesis is to measure the boron density n_B and solve equation (4.14) for the transport coefficients D and v in different plasma scenarios and then compare the measured coefficients with the theoretical predictions.

The theory is composed of different contributions from classical, neoclassical, and turbulent transport theory, and it is important to note that the measured coefficients are a sum of these individual contributions. In the following, the different theoretical components will be described.

4.2. Classical transport

The classical transport theory is based on Coulomb collisions of individual charged particles in a homogeneous magnetized plasma. No net radial transport occurs due to collisions between particles of the same species, since they would only exchange positions. In a pure deuterium ion and electron plasma, the classical transport would be very low. However, if impurities are introduced in the plasma, the Coulomb collisions cause friction forces between the main ions and the impurity ions, which lead to a radial flux, hence, classical transport is induced. Classical transport can be described by a simple model using a random walk Ansatz, i.e. diffusive transport. The gyrating particle is displaced perpendicular to the magnetic field line with a step size of a Lamor radius[1] ρ_L and the time in between two steps is characterized by the inverse of the collision frequency ν. The classical diffusion coefficient D_{CL}^{α} for a species α can therefore be estimated as:

$$D_{CL}^{\alpha} \approx \frac{\rho_{L,\alpha}^2 \nu_\alpha}{2}. \tag{4.16}$$

Classical transport is, however, very weak and does not take the geometry of the helical magnetic field into account. In order to do that, one has to consider neoclassical transport. A complete overview of classical transport can be found in Ref. [46].

4.3. Neoclassical transport

If one takes the phenomena arising from the curvature of the magnetic field into account in the collisional model, an additional neoclassical flux arises [47]. The physics of neoclassical transport in a tokamak depends on the magnitude of the collisionality ν_*. The collisionality is the ratio of the electron-ion collision frequency to the particle bounce frequency of the trapped particle and it is defined as:

$$\nu_* = \nu_{ei} \frac{R q_s}{v_{th} \epsilon^{3/2}}, \tag{4.17}$$

where R is the major radius, q_s is the safety factor, ν_{ei} the electron-ion collision frequency, v_{th} the thermal velocity, and $\epsilon = r/R$ the inverse aspect ratio. Three regimes of collisionality exist (see figure 4.1): the banana regime ($\nu_* < 1$), the plateau regime ($1 < \nu_* < \epsilon^{-3/2}$), and the Pfirsch-Schlüter regime ($\epsilon^{-3/2} < \nu_*$). The neoclassical fluxes are a sum of the fluxes of the contributions from these individual regimes.

In the banana regime, at low collisionalities, trapping of particles can occur due to the $1/R$ dependence of the toroidal magnetic field. Since the strength of the magnetic field in tokamaks varies along the major radius (see figure 1.2), particles traveling along the magnetic field lines will pass from regions with lower B at the LFS to regions with higher B on the HFS. Depending on the ratio of the parallel and perpendicular velocity components, a maximum magnetic field strength exists, for which particles are reflected before they reach the innermost point of the flux surface and then return along the field line; hence they are trapped in banana-shaped orbits. The trapping

---

[1]The Lamor radius is defined as: $\rho_L = \frac{m v_\perp}{qB}$, where $v_\perp$ is the velocity perpendicular to B.
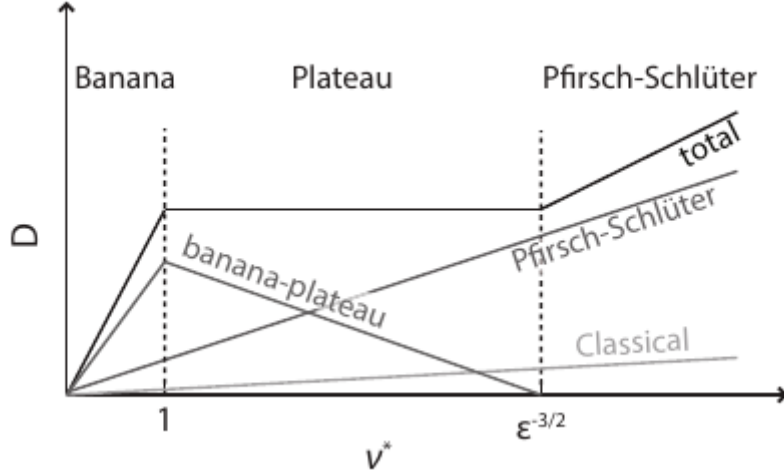
Figure 4.1.: The three neoclassical regimes: banana regime at low collisionalities, the plateau regime at intermediate collisionalities, and the Pfirsch-Schlüter regime at high collisionalities. Figure taken from [45].

condition reads:

$$\left.\frac{v_\parallel}{v_\perp}\right|_{\text{LFS}} < \sqrt{\frac{B_{\text{HFS}}}{B_{\text{LFS}}} - 1}. \tag{4.18}$$

The particles can be trapped or de-trapped due to collisions and the modification to the classical diffusion coefficient is determined by the width of the banana orbit ω_b and the collision frequency for de-trapping ν_b:

$$D_{BP} \approx \frac{\omega_b^2 \nu_b}{2} = \frac{q^2}{\epsilon^{3/2}} D_{CL}. \tag{4.19}$$

At high collisionalities the banana trapping is negligible and we enter the Pfirsch-Schlüter regime. The gradient and curvature of the magnetic field lines in the toroidal configuration give rise to the diamagnetic current, causing charge separation, a vertical electric field and the ejection of particles on the outboard side via the $E \times B$ drift. However, the charge separation is compensated due to the helical structure of the magnetic field lines and the parallel Pfirsch-Schlüter current arises to suppress the charge separation. A small fraction of the vertical electric field remains due to the finite resistivity along the field lines. The related outward directed $\vec{E} \times \vec{B}$ drift then leads to a net radial transport. The diffusion coefficient for this regime reads:

$$D_{PS} \approx 2q^2 D_{CL}. \tag{4.20}$$

The collisionality regime between the banana and the Pfirsch-Schlüter regime is called the plateau regime. The name comes from the fact that in this regime the diffusion coefficient is almost independent of the collisionality forming a plateau, which can be seen in figure 4.1. Since the temperature profile in tokamaks typically is peaked, the core of the plasma features high temperatures and low collisionalities making it typically in the banana regime for the impurity ions. The edge of the plasma, on the other hand, has lower temperatures and higher collisionalities and the impurity ions

are, therefore, usually in the Pfirsch-Schlüter regime.

The convective part of the transport summarizes all off-diagonal elements of the transport metric. The total neoclassical drift velocity is the sum of the drift velocities of the different regimes and it depends on the gradients in the main ion density and temperature:

$$v_X = D_X Z \left(\frac{\mathrm{d} \ln n_D}{\mathrm{d}r} + \alpha_T \frac{\mathrm{d} \ln T_i}{\mathrm{d}r} \right), \qquad (4.21)$$

where X denotes the contribution of each regime (CL, BP, or PS). α_T is the collisionality dependent temperature gradient factor and it depends on the mass ratio between collision species, plasma parameters and geometry [48, 49]. At the low collisionalties, that are envisaged for ITER [50], α_T is negative [13]. In the case of negative gradients in the main ion density and temperature, the drift velocity is comprised of an inward part proportional to the main ion density and an outward part proportional to the temperature gradient. The outward contribution to the drift velocity plays a screening role known as *temperature screening* and it reduces the impurity peaking arising from the first convective term. α_T also depends on Z and the effectiveness of the temperature screening effect is stronger for heavier impurities [13].
The toroidal geometry, additionally, leads to an interaction of the inductive toroidal electric field used to generate the plasma current, with the trapped particles in the banana orbits. In the presence of this electric field, the trapped particles are accelerated when traveling in the direction of the magnetic field and decelerated when they are on the other side of the banana orbit. Thus, the electric field displaces the particles in the banana orbits and a net inward drift is observed which leads to a peaking of the density profiles. This net inward drift is called the neoclassical *Ware Pinch* [51]

$$v_{ware} = -k_{ware}(\nu) \frac{E_\parallel}{B_\perp}, \qquad (4.22)$$

where the factor $k_{ware}(\nu)$ depends on the collisionality. Since the Ware pinch produces an inward drift, it will cause the density profile to peak.

4.3.1. Experimental observations of neoclassical impurity transport

It is commonly known, from observations in several different tokamaks, that the neoclassical particle transport alone cannot explain the measured transport coefficients. A short summary of comparisons between experimental results and neoclassical transport predictions will be given in the following.
The neoclassical diffusivity is predicted to be a function of the collisionality and to decreases with impurity charge Z [49]. The Z-dependence has experimentally been observed for impurities with $Z < 18$ at AUG [48], however, for higher Z a discrepancy was found. The neoclassical diffusion coefficient normally ranges from $10^{-3}\,\mathrm{m^2/s}$ to $10^{-1}\,\mathrm{m^2/s}$. In the central region of the plasma ($\rho_{tor} < 0.3$), the neoclassical diffusion coefficient has been observed to be on the order of the experimental one for low-Z impurities at AUG [48] and also at JET for the mid-Z impurity beryllium [52]. It has also been observed that the diffusivity can be either neoclassical or anomalous in

this region depending on the heating scheme [53], becoming anomalous when central ECRH heating is added. However, in the core confinement region ($\rho > 0.3$), the neoclassical diffusivity is almost always one order of magnitude smaller than the measured one, meaning the transport is anomalous [53, 52, 54, 55, 56, 57, 58, 59, 60]. In the edge transport barrier (ETB) at AUG, the transport coefficients are also found to be neoclassical [61] and are described by the Pfirsch-Schlüter term [62].

In general, the neoclassical convection is predicted to be directed inward leading to a peaked density profile [49]. Several experimental studies have shown that the measured drift velocity in the core region of the plasma is much larger, in absolute values, than the neoclassical prediction [63, 52, 54, 55, 56, 59, 60]. Strong variations in the direction of the measured convection is seen in different tokamaks due to different operational regimes.

The discrepancy between the neoclassically calculated transport coefficients and the experimentally measured ones in the particle transport channel suggests that neoclassical theory cannot fully described the perpendicular transport. Further investigation, therefore, focuses on turbulent transport.

4.4. Turbulent transport

Neoclassical theory cannot fully explain the experimental observations of impurity transport. All transport exceeding the predictions of neoclassical theory is called anomalous, although the term turbulent transport is frequently used, since turbulence has been identified as its underlying mechanism. Plasma turbulence is created by micro-instabilities in the plasma and many types of instabilities can arise in tokamak plasmas. They are excited once the temperature and/or density gradients reach a critical limit. The micro-instabilities create microscopic turbulence eddies which are able to transport particles, heat, and momentum perpendicular to the field lines. On the ion Larmor radius scale, the two dominant electrostatic instabilities are the ion temperature gradient (ITG) mode and the trapped electron mode (TEM).

4.4.1. The ion temperature gradient instability (ITG)

The ion temperature gradient instability (ITG) [64, 65, 66] is triggered when the ion temperature gradient exceeds a critical threshold. The ∇B drift is proportional to the particle's temperature, which implies that hotter particles will, with respect to colder particles, drift further. Due to the ∇B drift, a temperature perturbation causes a perturbed drift velocity which leads to a charge separation. The charge separation gives rise to an electric field which results in an $\vec{E} \times \vec{B}$ flow. On the high field side (HFS), the direction of the temperature gradient is reversed with respect to the magnetic field gradient, which means that the $\vec{E} \times \vec{B}$ flow will reduce the initial perturbation (see left side of figure 4.2). On the other hand, at the low field side (LFS), where the temperature gradient and magnetic field gradient point in the same direction, the $\vec{E} \times \vec{B}$ flow will enhance the perturbation, hence, the plasma is unstable (see right hand side of figure 4.2). The mode will, therefore, always develop on this unstable side and this region of the plasma is dubbed to have bad curvature. This instability can grow exponentially
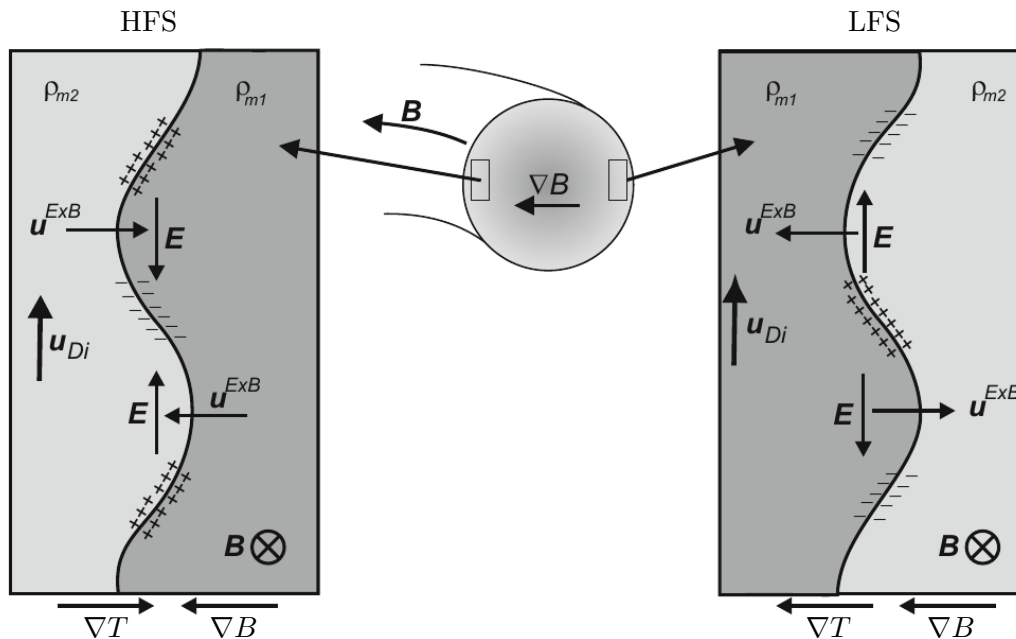
Figure 4.2.: Visualization of the ITG instability. Due to the temperature gradient in the plasma, a perturbation will be stabilized on the HFS and destabilized on the LFS. Picture modified from [67].

due to the positive-feedback loop. The scale lengths of ITG mode are of the order of the ion Larmor radius.

4.4.2. The trapped electron mode instability (TEM)

In the description of the ITG mode, the electrons are assumed to be adiabatic. By including electron dynamics other modes such as the trapped electron mode (TEM) [68, 69, 70] arise. In a tokamak, the inhomogeneity of the magnetic field will cause trapping of particles on the LFS which then can lead to radial transport. The TEM is driven by electron density and temperature gradients. The situation is analogous to the ITG case, but here the slow average motion along the field line is due to the trapping of the electrons, while this slow motion for the ions is caused by their inertia. The scale lengths of the TEM instability is the same as for the ITG instability.

4.4.3. Turbulent particle transport

By examining the general expression for the radial particle flux:

$$\Gamma = n \left(-D \frac{\partial \ln n}{\partial r} + v \right) \tag{4.23}$$

it becomes clear that the flux is comprised of a diagonal term namely the diffusion D, and an off-diagonal term, the convection v. Gyrokinetic theory, for example, can be used to decompose the particle flux, for both electrons and impurities, and analyze the underlying microscopic mechanisms of particle transport caused by ITG and TEM modes.

For impurities the quasi-linear radial particle flux can then be written in the form:

$$\frac{R\Gamma_n}{n} = D_n \frac{R}{L_n} + D_T \frac{R}{L_{T_i}} + D_U u' + RV_{pn} \tag{4.24}$$

and is, thus, composed of the diagonal diffusion term and the off-diagonal convective terms: thermo-diffusion, roto-diffusion, and pure convection. Here, the normalized logarithmic gradient of a plasma quantity X is defined as:

$$\frac{R}{L_X} = -\frac{R}{X}\frac{\mathrm{d}X}{\mathrm{d}r}, \tag{4.25}$$

where R is the major radius.

The first term on the right hand side of equation (4.24) is the diagonal diffusive flux, which is proportional to the normalized logarithmic density gradient $\frac{R}{L_n}$. As the diffusion coefficient D is strictly positive, it is always directed outward.

The second term is the off-diagonal thermo-diffusion, which contributes to the total convection or pinch velocity. It is proportional to the normalized logarithmic temperature gradient $\frac{R}{L_T}$ and originates from the energy dependence of the curvature and ∇B drifts. The thermo-diffusion part can change direction depending on the most unstable mode [71]. For impurities, the thermo-diffusion is directed outward when ITG is the dominant mode and inward for TEM.

The roto-diffusion flux is the third term in equation (4.24) and it is proportional to the normalized toroidal velocity gradient:

$$u' = -\frac{R^2}{v_{th}}\frac{\mathrm{d}\Omega_\phi}{\mathrm{d}r}, \tag{4.26}$$

where v_{th} is the thermal velocity and Ω_ϕ is the angular toroidal rotation velocity. This term is not present in the electron particle flux, since the light electrons have a high thermal velocity which makes rotational effects negligible. Compared to the electrons, this effect cannot be neglected for the heavy impurities and, the heavier the impurity the more prominent is the effect. Similar to the diagonal diffusion, this term is caused by the $\vec{E} \times \vec{B}$ drift in the presence of a rotational velocity gradient. Just like in the thermo-diffusion case, this contribution to the total pinch velocity can change sign or direction whether ITG or TEM is the dominant mode [72]. For impurities, it is directed inward for TEM and outward for ITG.

The last term, the pure convection, appears due to a combination of different mechanisms [73, 71, 72]. The mechanisms are the $\vec{E} \times \vec{B}$ compression, which is independent of charge, the curvature and ∇B drift, which decreases with increasing charge, and parallel dynamics, which depend on Z/A, where A is the mass of the impurity. When monotonic q_s-profiles are present the pure convection is directed inward, but the piece related to parallel dynamics can, depending on the most unstable mode, change direction. Exact equations for the diagonal and off-diagonal coefficients of the turbulent particle flux can be found in Ref. [73].

4.5. Comparing theoretical transport modeling with the experiment

For a complete picture, when comparing experimental results with theoretical predictions, the turbulent, neoclassical, and classical parts must be taken into consideration. For the diffusion, drift velocity, and normalized impurity density gradient it then naturally follows:

$$D_{theory} = D_{turb} + D_{neo}, \tag{4.27}$$

$$v_{theory} = v_{turb} + v_{neo}, \tag{4.28}$$

$$\frac{R}{L_{n\,theory}} = -\frac{R(v_{turb} + v_{neo})}{D_{turb} + D_{neo}}, \tag{4.29}$$

where the subscript *turb* and *neo* stands for the turbulent and neoclassical component, respectively. From now on and throughout this thesis, the classical part is included in the neoclassical contribution. Since the neoclassical transport is small, the normalized density gradient can be approximated with just the turbulent part. As mentioned above, the turbulent transport is composed of several contributions and the turbulent normalized impurity density gradient, representing the steady-state situation, is a sum of these individual terms:

$$\frac{R}{L_{n_{turb}}} = -\left(\frac{D_T}{D_n} \frac{R}{L_{T_i}} + \frac{D_U}{D_n} u' + \frac{RV_{pn}}{D_n} \right) = -\left(C_T \frac{R}{L_{T_i}} + C_U u' + C_P \right). \tag{4.30}$$

In this work the neoclassical contribution (including the classical piece) are calculated with the code NEO [74, 75]. The turbulent part is modeled with the gyrokinetic code GKW [76]. GKW makes the connection between the microscopic instabilities and the macroscopic quantities. The measurable macroscopic quantities, i.e. gradients, are inputs to the code.

4.5.1. Experimental studies on turbulent electron and impurity transport

The study of impurity transport can already be dated back to the early 1980s [77, 78, 79, 80]. As the realization of the importance of controlling the impurity transport has increased, transport studies have received more and more attention worldwide. In the past years, steady-state and transient impurity transport studies of both low-Z and high-Z impurities have been conducted in a broad variety of plasma conditions in several different tokamaks around the world.

As already briefly reviewed in section 4.3.1, comparing the measured transport coefficients with neoclassical calculations has been done extensively in the past. As more and more studies revealed discrepancies between the neoclassically predicted transport and the measurements more effort has been put into developing the theory of the turbulent transport as well as the simulation codes to calculate it. As the computers are getting more and more powerful, the computationally expensive turbulent transport simulations are now becoming a part of the standard analysis. As mentioned in section

4.1, a steady-state analysis can only provide information on the ratio of the diffusion and convective coefficients (see equation (4.15)). Therefore, this type of analysis is applied in situations where no time-dependent density signal is at hand. However, the importance of determining the transport coefficients separately can be understood considering that this also allows more complete comparisons with the theoretical predictions of impurity transport models. This lends itself directly to the goal of increasing our confidence in the prediction of the diffusion of helium, which is a critical parameter in determining the impact of the central helium source produced by fusion reactions. Moreover, accurate investigations dedicated to low-Z impurities are of critical importance in the validation of impurity turbulent transport models. This is an important element in the prediction of the impurity density profiles in a fusion reactor plasma, also for high-Z impurities. In present experiments the transport of heavy impurities is much more dominated by the neoclassical convection [81], in contrast to light impurities which are more dominated by turbulent transport [45, 60, 55]. However, at the very low collisionalities of a reactor, the role of turbulent transport is expected to become significantly more important also for heavy impurities and the neoclassical transport is expected to be less important [82].

A lot of research has been dedicated to electron particle transport. It has been observed that under certain conditions the electron density profile peaks when applying heating to the electron channel [57, 83]. This can be explained by a change of the turbulence regime. The electron density gradient changes with the real frequency ω_r of the most unstable mode [83, 84, 57]. In an ITG dominant regime, that is a positive value of ω_r, the addition of ECRH power leads to an increased peaking of the electron density, a decrease in ω_r, and to a transition from ITG to TEM (negative ω_r). This transition in density peaking is connected to the off-diagonal thermo-diffusion term which flips direction (sign) going from inwards to outwards [85]. If already in a TEM dominant regime, increasing the ECRH power will cause the peaking of the electron density to decrease. This phenomenon is called "density pump-out" [83]. The peaking obtains its highest values in the TEM regime near the transition from ITG to TEM. This behavior has been observed in AUG H-mode plasma experiments as well as being quantitatively predicted by theoretical simulations [83, 86, 84, 57] and is illustrated in figure 4.3.

Measuring the impurity particle transport is, however, more challenging. The simple approach, when no time-dependent impurity density signal is available, is to perform a steady-state analysis, but this type of analysis can only provide the ratio of the diffusion and convective coefficients (see equation (4.15)). In order to carry out a transient impurity transport study, the studied impurity has to be injected into the plasma in some manner. The most common ways of injecting impurities for a time-dependent transport study are with gas puffing [60, 55, 87, 88, 58] or laser blow-off [53, 89, 54, 90]. Via these approaches, both low- and high-Z impurities can be investigated. High-Z impurities are often measured with the soft X-ray diagnostic whereas low-Z impurities are measured with CXRS. However, it should be noted that via these methods the studied impurity is added to the plasma and this can, in some cases, further complicate the analysis due to the recycling mechanisms of the injected impurity. In this
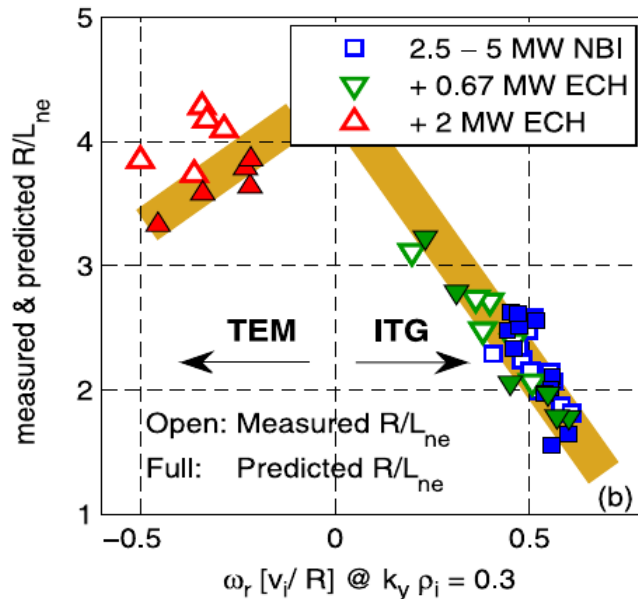
Figure 4.3.: Predicted and measured electron density gradient as a function of the frequency of the most unstable mode showing a non-monotonic behavior. Picture taken from [85].

work, however, a novel method of inducing a time perturbed boron density, which is an intrinsic impurity at AUG, has been developed and utilized to uniquely determine the transport coefficients D and v with high radial resolution in H-mode plasmas. This method will be presented in the next chapter, but before we present a summary of the impurity transport field.

4.5.2. Overview of previous impurity transport results

Some examples of impurity transport studies conducted in the past 20 years at different machines are: [91, 59, 88, 92] at Alcator C-Mod, [93, 48, 53, 61, 58, 45, 94, 95] at AUG, [87, 60] at DIII-D, [96, 97] at MAST, [98, 99, 100, 54, 55, 90, 101] at JET, [102] at KSTAR, [63, 52] at TCV, and [56, 103, 104] at Tore Supra. A brief review of the results from some of these studies will be given in the following. Focus has been put on transport studies that deduce D and v individually and also include a direct comparison with turbulent transport theory.

At Alcator C-Mod, calcium laser blow-off experiments were performed in ICRH-only heated L-mode plasmas [59, 88]. In these discharges, the influence of the plasma current on the transport coefficients was investigated. It was observed that the edge diffusion decreased and the edge convection increased (going from more negative to less negative) with increasing plasma current. The experimentally deduced transport coefficients were compared to heat flux matched turbulent transport simulations carried out with the code GYRO. Even though the total heat flux Q_{tot} was matched between the simulation and the experiment, the simulated coefficients exceeded the measured

ones by a factor of two. The predicted diffusion was higher and the predicted convection was more negative than the experimentally measured ones.

Experiments were performed at DIII-D, puffing fluorine into NBI heated, ELM-suppressed H-mode plasmas [60]. In this study it was observed that the turbulent diffusion, deduced with the TGLF code, was of the right order of magnitude. The radial profile, however, did not match well, resulting in an over-prediction in the central region and an under-prediction in the edge region. The turbulent drift velocity was in all cases more negative than the measured one.

Low Z-impurity experiments in L-Mode [97], as well as in L-mode and in H-mode [96] were conducted at MAST. In these studies helium and nitrogen were puffed. Additionally, the transport of the intrinsic impurity carbon was measured. The neoclassical calculations were performed with the code NEO and the quasi-linear gyrokinetic simulations with the codes GKW and GS2. In Ref. [96], it was observed that the helium transport is anomalous from mid-radius to the plasma edge in L-mode, but in the H-mode plasma the transport was dominated by neoclassical theory. This study was expanded to also include nitrogen and carbon in Ref. [97]. The transport of carbon and nitrogen in L-mode was similar and the transport coefficients of the different impurities showed little difference. The diffusion of helium agreed with the ones from the other two impurities up to mid-radius, but was slightly lower at the edge. The helium convection also showed similar behavior up to mid-radius and was then less negative meaning it had a more peaked density profile towards the edge of the plasma. For carbon and helium, there was an agreement of the particle diffusion with the neoclassical predictions in the center of the plasma. The turbulent transport simulations were, therefore, only carried out for the edge region. Including the result of these simulations resulted in an agreement between the experimental and theoretical transport coefficients over the whole analyzed spatial region.

At Tore Supra, nickel was injected into the plasma via laser blow-off for a transient transport analysis [104]. In these experiments the deposition location of the two ECRH gyrotrons were varied. This mainly affected the diffusion coefficient in the center of the plasma ($r/a < 0.2$), which is one order of magnitude larger ($0.1\,\mathrm{m^2/s}$ compare to $0.01\,\mathrm{m^2/s}$) in the case where the gyrotrons deposited their power at an outer location ($r/a = 0.58$). Thus, the discharge with deposition location further in ($r/a = 0.35$) featured the lowest diffusion in the center. Outside of $r/a > 0.2$ the diffusion profile is basically identical in all cases and goes up to $10\,\mathrm{m^2/s}$ at the edge. The changes in the v profile due to the different deposition locations were not outside the error bars and the convection was negative (peaked nickel density profiles) in all cases. The code NCLASS was utilized to predict the neoclassical transport and the code QuaLiKiz to predict the turbulent transport. The neoclassical calculations under predicted the experimental results in all cases. The discharge with the innermost ECRH deposition location was modeled with QuaLiKiz. The results of these simulations showed a quantitative agreement for both D and v. The sensitivity analysis of the quasi-linear simulation did, however, deliver a region of large uncertainty (two orders of magnitude in D). It should also be noted that these gyrokinetic simulations with QuaLiKiz did not include

the roto-diffusion term, which plays a more important role for nickel ($Z = 28$) than for other lighter impurities, for example, helium or boron (see discussion in section 4.4.3).

Another time-dependent impurity transport study, where the ECRH deposition location was altered, was performed at AUG. In these experiments, the studied impurity was argon, which was puffed into L-mode plasmas [58]. In contrast to the study at Tore Supra [104], both the diffusion and drift velocity profiles changed drastically when changing the deposition location of the gyrotrons. For a central deposition location ($\rho = 0.23$), an increase in the diffusion and a rise of a positive drift velocity around the deposition location was observed. When comparing the results with neoclassics, computed with the code NEOART, the central diffusivity reached neoclassical levels for the discharges with off-axis ECRH heating. Quasi-linear gyrokinetic simulations were performed with the code GS2. Here, only the ratio v/D was deduced for the radial window $0.4 < \rho < 0.6$. It was found that the theoretical v/D underestimated the experimental result by a factor of two in the cases with the most central and off-axis deposition locations. In the discharge with mixed deposition location, an agreement in v/D between the quasi-linear runs and the experiment was found.

Also transient transport studies of impurities with even higher Z such as tungsten have been conducted. At AUG, the transport of the intrinsic impurity tungsten was studied in H-mode plasmas by looking at the tungsten modulation induced by the sawteeth [95]. Also in these experiments the influence of the wave heating (ECRH and ICRH) was investigated. It was observed that the tungsten drift velocity increased, from negative to positive, with increasing ECRH and ICRH power, whereas the diffusion coefficient was independent of the power level. The modeling was preformed with the code NEO for the neoclassical calculations and the code GKW for the gyrokinetic simulations. The experimental diffusion coefficients were found to be at the neoclassical level, and when including the gyrokinetic results, the diffusion was over predicted. The trend seen in the convection with increasing heating power was qualitatively reproduced by the modeling. However, the theory failed to predict the outward convection seen in the experiment. The neoclassical values were, thus, more negative than the experimental ones and when including the turbulent result, the total theoretical v became even more negative.

The studies reviewed above are all single transport experiment at different machines, using different measuring and analysis techniques, as well as various neoclassical and turbulent codes, which in turn include different physics pieces. Therefore, it should come as no surprise that the results are quite diverse. A more systematic approach to validate the theory with the experimental results is to perform many transport experiments, all in the same tokamak, in an identical manner and, hence, gather larger datasets of, ideally, different impurities at the same time. The same analysis procedure and codes should then be applied to the whole database. In such a way, reliable conclusions can be drawn about the transport of the impurities and the predictive capabilities of the codes. At AUG, a few such steady-state studies have been carried out in the past looking at helium [45] and boron [45, 72, 57]. In these boron studies an analogous behavior to what we saw for the electron transport was also found [45,

72, 57]. The boron density gradient has been observed to peak when increasing the ECRH heating, whereas the profile is flat or even hollow in NBI heated plasmas. When modeling these experimental observations without taking the off-diagonal roto-diffusion term into account a discrepancy was found and the simulation predicted a much more peaked boron density profile [72]. Including the roto-diffusion in the simulation resulted in a better agreement, however, the gyrokinetic simulation could still not fully capture the hollowness of the density profiles. In the study of Ref. [72], also a clear correlation between T_e/T_i and the different off-diagonal contributions was noticed. Both the thermo-diffusion and the roto-diffusion went from being directed outward (positive value) to inward (negative value) as T_e/T_i increased, going from ITG to TEM. The pure pinch was always negative (inward direction).

Studies conducted at other machines have also observed discrepancies between theory and experiment for hollow low-Z impurity density profiles. A transport study at JET analyzing a large database of H-mode carbon steady-state profiles [105] showed that the gyrokinetic simulations, performed with the code GKW, quantitatively reproduced the experimental carbon density profiles when $T_e/T_i < 1$, provided that roto-diffusion was taken into account in the quasi-linear simulations. As in the AUG studies mentioned above, at $T_e/T_i > 1$ the quasi-linear simulations systematically predict peaked carbon profiles for the experimental hollow carbon profiles. A couple of non-linear gyrokinetic simulations confirmed these results.

Other studies at JET have also reported this behavior. Theoretical results from the Weiland multi-fluid model as well as quasi-linear and non-linear gyrokinetic simulations with the GENE code were compared with previously conducted transport experiments at JET [106], studying the impurities argon, carbon, neon, and nickel. The fluid and the gyrokinetic simulations both predicted the same impurity behavior and these theoretical predictions could qualitatively reproduce the experimental findings for argon, neon, and nickel. However, for carbon, the experimentally hollow or peaked profiles could not be reproduced by the theoretical simulations. In the most recent JET study on impurity transport [101], experimental L-mode steady-state helium, beryllium, carbon, nitrogen, and neon profiles where compared with gyrokinetic simulations. The experimental helium, beryllium, and neon profiles were all peaked, whereas the carbon and nitrogen profiles were flat or hollow. The gyrokinetic simulations utilizing the code GENE, predicted peaked profiles for all the studied impurities and, thus, also failed to capture the behavior of the hollow carbon and nitrogen profiles.

In summary, impurity transport is at the moment a hot topic in the fusion community and it is not to be expected to cool down in the near future, since more studies, at different tokamaks, are reporting on the same discrepancy between the theory and the experiment, namely for the hollow low-Z impurity density profiles. There are examples where good agreement is achieved, but many examples where it is not. Intense work is ongoing on finding an explanation to why the theory fails. The studies observing this behavior at AUG and JET mentioned above were all steady-state studies, which only delivered the ratio v/D. In order to put further constrains on the theory, we need to pinpoint if the problem lies in the predicted diffusion, convection, or perhaps both. For

this purpose, transient impurity transport studies on large databases of observations and, ideally, on multiple impurities are vital. This is a direct motivation for this work, which can disentangle the diffusivity and convection of boron for the first time at AUG with the help of a newly developed modulation technique. In the next chapter this technique along with the method of deducing the transport coefficient from the experimental data is introduced. This technique combines the advantages of a transient transport analysis performed on modulated signals over many periods, as often applied for heat transport studies [107, 108], with the high radial resolution enabled by the CXRS. To demonstrate how the method works, one experimental example will be shown and compared to neoclassical and turbulent theory. In chapter 6 the whole database of measured boron transport coefficients are presented along with a detailed theory comparison in the hope of shedding some light upon the previously observed discrepancies.

4.6. Effect of plasma instabilities on impurity transport

In addition to the transport mechanisms already discussed, various plasma instabilities may have a substantial effect on the transport of impurities. Some examples of common plasma instabilities are MHD activities like sawtooth crashes in the center of the plasma and ELMs in the edge region. The study of the impact of MHD activity on impurity transport has received some attention in the past years [48, 109, 110, 94] and in the study of Ref. [61] the ELMs are utilized to individually deduce the edge transport coefficients of several different impurities. However, as these events take place on different spatial and temporal scales than collisional and turbulent transport, we can consider them as perturbations to the background profiles. Therefore, in this work, we are not considering the plasma instabilities's impact on the boron transport. Sawteeth are present in our experiments, but the region of interest for our analysis does not include the domain within the sawtooth inversion radius. Furthermore, the direct effect of the ELMs is also outside the scope of this work, since the aim is to characterize the core transport.

Chapter 5.

Novel method on boron density modulation

As mentioned in the previous chapter, in order to disentangle D and v from one another we need a time-dependent boron density signal. In this work, a new method of obtaining such a signal at AUG was discovered and thoroughly tested. Additionally, a numerical framework for solving the transport equation, which is tailored to the specific shape of the boron density signal, was developed and benchmarked. Both the methodology and the numerical framework are described in the following chapter. Parts of this chapter are published in [111].

5.1. Methodology

5.1.1. Boron density modulation with ICRH

At AUG, it was observed that a modulation of the power of the boron- and tungsten-coated ICRH antennas results in a modulation of the boron density in the plasma. This can be clearly seen in figure 5.1, where the ICRH power is presented in blue and the resultant boron modulation signal in red for one CXRS channel at $\rho_{tor} = 0.76$. The boron modulation is stronger at the edge than in the core and the edge also responds more quickly than the core to the change in the ICRH power, which indicates a change in the boron source from the edge plasma or SOL rather than a change in core transport. Moreover the measurement of the boron influx at the limiters also increases when the power of the antennas is modulated, consistent with this picture. Therefore, this technique can be used for core boron transport studies. The exploration and exploitation of this possibility is the subject of this work.

It was discovered already in the 1980s that the operation of ICRH antennas can cause an increased influx of metallic impurities [112, 113], which arises due to the RF sheath potentials in the Faraday screen gaps [114, 115]. The ICRH concept in this work is similar to the work in Ref. [116], in which the tungsten transport at the edge was studied by modulating the power of the ICRH antennas. The ICRH system at AUG has been updated, since that work was conducted, and is now comprised of four antennas in pairs of two: two 2-strap boron-coated and two 3-strap tungsten-coated antennas [117]. In this study, all the ICRH antennas are operated in phase and the ICRH heating scheme used is the hydrogen minority heating with a frequency of the ICRH generators of 36.5 MHz.

A feasibility study was conducted to better understand the boron source and if the

technique can be used for transport studies. At AUG, boron is considered to be an intrinsic impurity due to the regularly performed boronizations, during which the vessel wall is covered with a thin layer of boron [118, 119]. It has been observed that the boron modulation signal is strongest when the experiments are performed in a freshly boronized machine. This suggests that the ICRH power modulation affects the boron coating on the antennas and/or the wall which originates from the boronization and not the boron of the antenna itself. This hypothesis is strengthened by the fact that a strong modulation signal is also achieved when only modulating the tungsten-coated ICRH antennas. Furthermore, only a modulation of the ICRH power has an impact on the boron density, since attempts at modulating the ECRH at various power levels did not result in a boron modulation. The feasibility study also demonstrated that this technique is applicable in a broad variety of H-mode, lower single null (LSN) plasma conditions. Apart from that the method is insensitive to the plasma current, magnetic field, and plasma parameters. So far, the ICRH modulation has only been observed to affect the boron content in the plasma; helium, carbon, and nitrogen show no modulation behavior. On the other hand, the concentrations of these impurities were very low, making a possible modulation perhaps beyond detection. All in all, this method may be applicable in other machines which have carbon walls or also utilize boronization as a wall conditioning technique.

A requirement for the feasibility of this technique is a steady plasma background, which means keeping the electron density and the ion and electron temperatures constant such that the transport coefficients D and v are not time-dependent during the modulation. From the feasibility experiments it is clear that the amplitude of the measured boron density modulation scales with the ICRH power, but increasing the ICRH power also causes a bigger modulation of the ion and electron temperatures. Therefore, one has to choose a power level at which a clear modulation of the boron density is observed, while the modulations of the other quantities are kept as low as possible. From the study it was concluded that a power level of $1\,\mathrm{MW}$ of ICRH is sufficient to modulate the boron density up to $10\,\%$ at the edge while keeping the modulation of the ion and electron temperatures to less than $4\,\%$. Different modulation frequencies were tested and also here a balance between a clear boron modulation signal and the perturbation to the plasma background has to be maintained. The modulation frequency range chosen for the heating power is $8-10\,\mathrm{Hz}$. The choice of frequency directly translates to the perturbation seen in the boron density, which is clearly visible in figure 5.1.

5.1.2. Numerical scheme

Solving equation (4.14) for the impurity density n_Z given a D and v is called the *forward problem*. However, the situation at hand is the opposite: the measured boron density n_B is known and the corresponding D and v profiles should be deduced. This is the *inverse problem*. This task, unlike the simple forward problem, is non-trivial since the problem itself is ill-posed, thus small errors in the measured data are greatly amplified in the solution. One way of regularizing the problem is to impose smooth D and v profiles. The boron density n_B is measured at discrete radial locations $(r_l)_{l=1,...,N_{los}}$ and time points $(t_k)_{k=1,...,N_t}$, where r_l denotes the radial and t_k the time measurement positions. t_k depend on the integration time of the CXRS diagnostic and r_l on the geometry
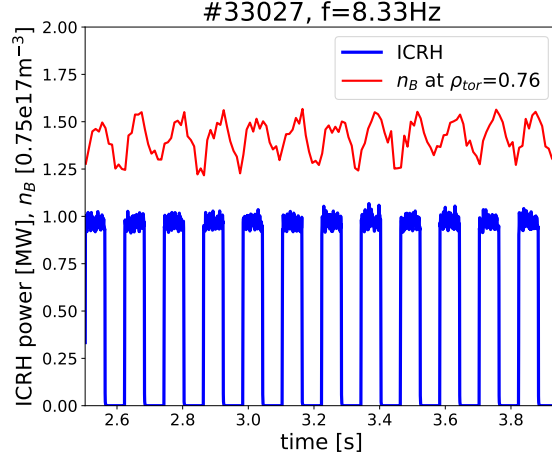
Figure 5.1.: ICRH power modulation with a frequency of 8.33 Hz (blue) and the resultant modulation of the boron density at $\rho_{tor} = 0.76$ (red).

of the LOSs and their intersection volumes with the NBI. This yields the measured data points $n_B^{l,k} = n_B(r_l, t_k)$, such that there is no continuous representation of $n_B(r, t)$ available from which the v and D profiles can be calculated directly as in Ref. [120]. Therefore, smooth v and D profiles have to be found such that the resulting simulated local densities n_S evaluated at the measurement points $n_S(r_l, t_k)$ are in good agreement with the measured data $n_B^{l,k}$. This inverse problem can be cast in the formalism of a minimization. By inserting some initial D and v profiles in equation (4.14) a forward calculation is performed yielding a simulated density $n_S(r, t)$. The simulated density is evaluated at the discrete measurement points resulting in $n_S(r_l, t_k)$ such that the difference between the measured and simulated density at the respective points can be expressed by $|n_S(r_l, t_k) - n_B^{l,k}|$. By varying the input D and v profiles a new value of $|n_S(r_l, t_k) - n_B^{l,k}|$ is obtained and this process is iterated until a minimum of the difference is found. In this way, the D and v profiles corresponding to the measured boron density $n_B^{l,k}$ is acquired. This minimization procedure can mathematically be written as:

$$\min_{D,v,s} \frac{1}{2} \sum_{l} \sum_{k} \left| \frac{n_S(r_l, t_k) - n_B^{l,k}}{\sigma_B^{l,k}} \right|^2 \quad \text{w.r.t equation (4.14)}, \tag{5.1}$$

where $\sigma_B^{l,k} = \sigma_B(r_l, t_k)$ are the standard deviations of the densities at the measurement points r_l and t_k. Since the measured boron signal is periodic (see figure 5.1), a robust Ansatz for the reconstructed density $n_S(r, t)$ as well as the boundary condition $s(t)$ which fits the measured data particularly well is

$$n_S(r, t) = n_0(r) + a(r) \cos(\omega t) + b(r) \sin(\omega t)$$
$$s(t) = s_0 + a_0 \cos(\omega t) + b_0 \sin(\omega t). \tag{5.2}$$

In equation (5.2), n_0 is the steady-state density and $\omega = 2\pi f$, where f is the frequency of the modulation. The boron source term $s(t)$ is assumed to have the same time dependence as the density n_S. This Ansatz is used when solving the inverse problem

(5.1) and inserting the Ansatz in equation (5.1) yields

$$\min_{D,v,s_0,a_0,b_0} \frac{1}{2} \sum_l \sum_k \left| \frac{(n_0(r_l) + a(r_l)\cos(\omega t_k) + b(r_l)\sin(\omega t_k)) - n_B^{l,k}}{\sigma_B^{l,k}} \right|^2. \tag{5.3}$$

By also inserting the Ansatz in the radial transport equation (4.14), three equations are obtained: one for the steady-state $n_0(r)$

$$\frac{1}{r}\frac{\partial}{\partial r}\left[r\left(D(r)n_0'(r) - v(r)n_0(r)\right)\right] = 0 \tag{5.4}$$

and two for the modulation part $a(r)\cos(\omega t) + b(r)\sin(\omega t)$

$$\omega a(r)r + \frac{\partial}{\partial r}\left[r\left(D(r)b'(r) - v(r)b(r)\right)\right] = 0 \tag{5.5}$$

$$-\omega b(r)r + \frac{\partial}{\partial r}\left[r\left(D(r)a'(r) - v(r)a(r)\right)\right] = 0. \tag{5.6}$$

Inserting the boundary condition $s(r)$ in the transport equations yields

$$n'(0) = 0, \ n(r_{max}) = s_0 \tag{5.7}$$

$$a'(0) = 0, \ a(r_{max}) = a_0 \tag{5.8}$$

$$b'(0) = 0, \ b(r_{max}) = b_0, \tag{5.9}$$

where r_{max} is the last data point of the experimental data. Finally, the Neumann boundary conditions for D and v, which resolve the singularity at $r = 0$, can be expressed as follows:

$$v(0) = 0, \ v'(0) = 0, \ v'(r_{max}) = 0 \tag{5.10}$$

$$D'(0) = 0, \ D'(r_{max}) = 0, \ D \geq 0. \tag{5.11}$$

Equations (5.3) – (5.11) represent the complete mathematical description of the minimization problem. The model can be reduced to the steady-state and the modulation at the frequency ω, which corresponds to a Fourier transform in time at the modulation frequency. Thus, no time discretization is necessary.

In this work, equation (5.1) is solved with SLSQP (Sequential Least SQuares Programming) [121], which is a quasi-Newton method, yielding the reconstructed density n_S by solving equation (4.14) for various D and v profiles as well as the source term s, which is composed of the coefficients s_0, a_0, and b_0. The implementation of the problem has been set up in Python using the Scipy minimization library [122]. Second order finite differences are used for solving the transport equation; the derivation of the discretization scheme is outlined in appendix A.2. The D and v profiles are represented with arbitrary order B-splines, which enforce smoothness of the solution and is therefore a way of applying a regularization to the ill-posed problem. The minimization is thus performed over the B-spline knots of D and v as well as the coefficients s_0, a_0, and b_0. An example of the measured (left) and reconstructed (right) boron density is presented in figure 5.2, showing very good agreement. This becomes even clearer when studying the left hand-side of figure 5.3, which displays the difference between the simulated and measured boron density $|n_S - n_B|$. No additional modulation at the modulation
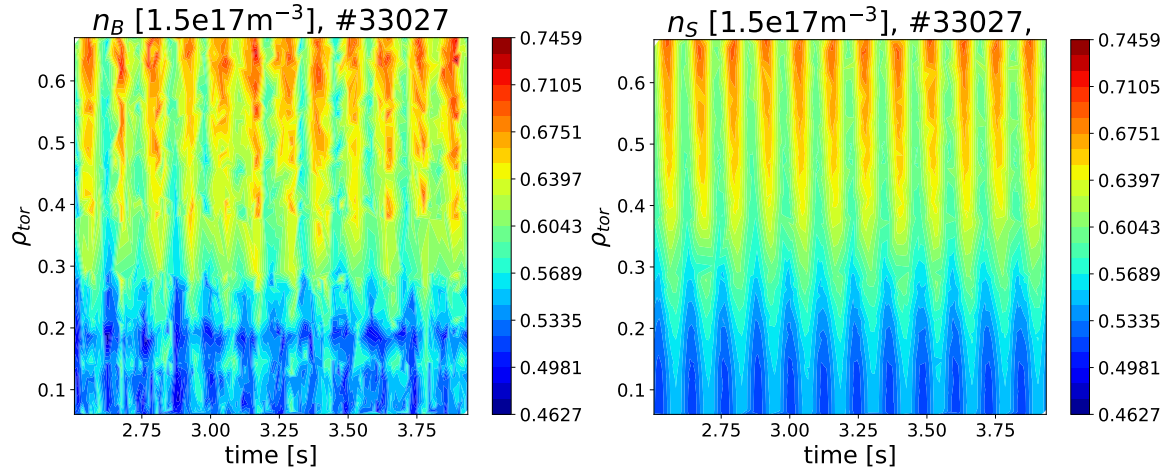
Figure 5.2.: Left: Contour plot of the measured boron density. Right: Contour plot of the reconstructed boron density. Note that the two plots have the same colorbar.

frequency of 8.33 Hz or any other frequencies can be seen and hence, the Ansatz from equation (5.2) is, for this problem, very well suited. This claim is further confirmed by computing a Fourier decomposition of the measured boron density n_B at $\rho_{tor} = 0.21$ (blue curve on the right hand-side of figure 5.3), which only displays a peak at the modulation frequency at 8.33 Hz, hence no higher harmonics are present in the central region of the plasma. In orange the same quantity at $\rho_{tor} = 0.76$ is shown. At this location near the plasma edge, additional smaller peaks are visible at the second and third harmonics, indicated by the black dash-dotted lines. These peaks are, however, one order of magnitude smaller than the peak at the first harmonics, i.e. 8.33 Hz, and barely distinguishable from the noise. Furthermore, the Fourier decompositions of the differences between the simulated and measured boron density $|n_S - n_B|$ at $\rho_{tor} = 0.21$ and $\rho_{tor} = 0.76$ are plotted with dashed green and red lines, respectively, and this quantity shows no additional frequency peaks outside of the noise. In the dataset presented here, sawteeth are present with a frequency of 16 Hz and an inversion radius of $\rho_{tor} \approx 0.25$. This corresponds to 1.6 sawtooth cycles for every CXRS integration time. The experimental data inside of $\rho_{tor} < 0.25$ is, hence, a sawtooth average, and therefore, the sawtooth frequency cannot be seen in the right plot of figure 5.3.

5.1.3. The deduced transport coefficients and experimental results

The experimental data presented in this chapter is from an H-mode plasma with a toroidal magnetic field of 2.5 T at the magnetic axis, a plasma current of 0.8 MA, and an edge safety factor q$_{95}$ of 5.2. The heating scheme was as follows: 5 MW of constant NBI, 0.5 MW of constant ECRH, and 1 MW modulation of the ICRH power as described in section 5.1.1. Time traces of the heating powers can be seen in figure 5.4c. The modulation frequency of the ICRH power, and consequently the frequency of the boron modulation, was 8.33 Hz, which can be seen in figure 5.1.

As mentioned in section 5.1.1, for this technique to be valid the modulation of the background plasma should be kept to a minimum. Consequently the amplitude of the
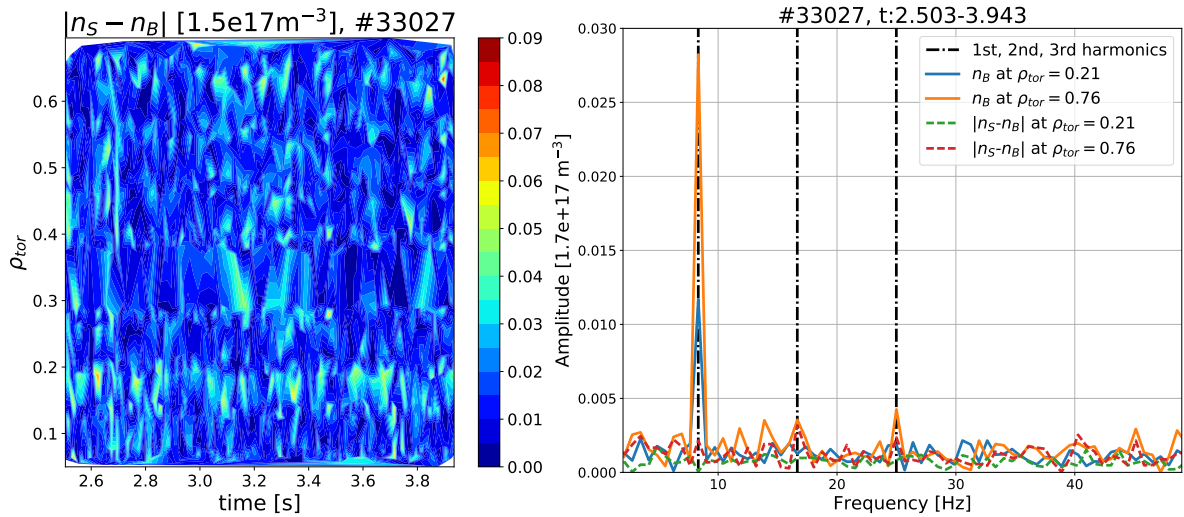
Figure 5.3.: Left: Contour plot of the difference between the simulated and measured boron density $|n_S - n_B|$. Right: Fourier decomposition of the measured boron densities n_B at $\rho_{tor} = 0.21$ in solid blue and at $\rho_{tor} = 0.76$ in solid orange as well as the difference $|n_S - n_B|$ at $\rho_{tor} = 0.21$ in dashed green and at $\rho_{tor} = 0.76$ in dashed red. Lines indicating the first, second, and third harmonics in dash-dotted black.
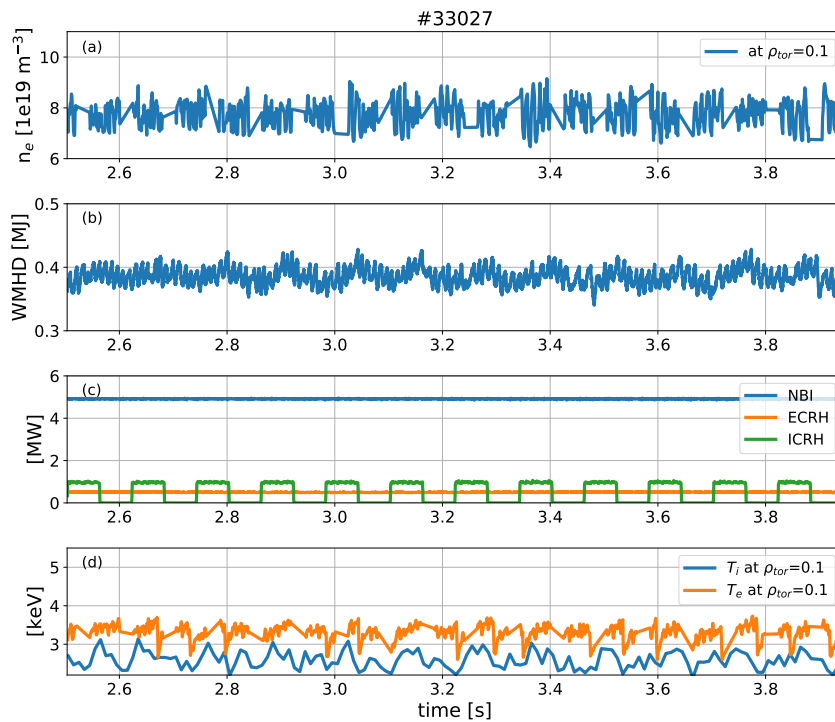

Figure 5.4.: Time traces of the (a) electron density at $\rho_{tor} = 0.1$, (b) plasma stored energy (WMHD), (c) NBI, ECRH, and ICRH powers, and (d) electron and ion temperatures at $\rho_{tor} = 0.1$ for the discharge 33027.
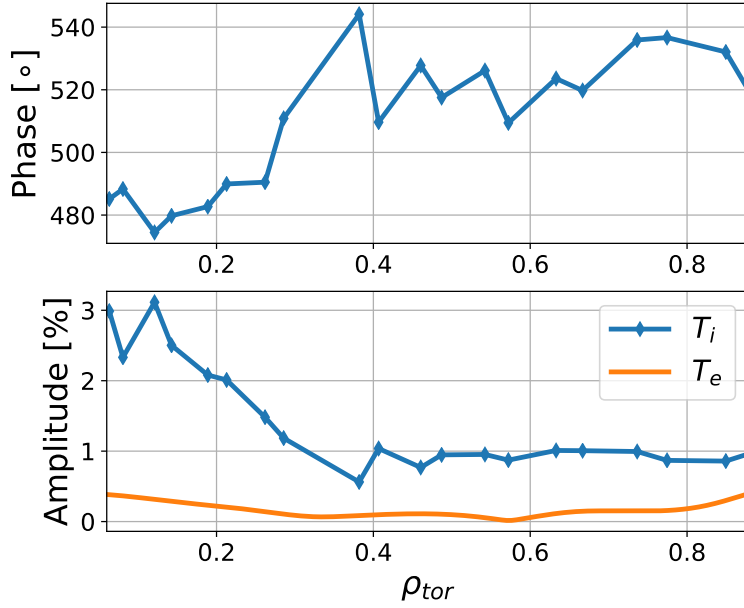
Figure 5.5.: Phase and amplitude of the modulation of T_e (orange) and T_i (blue) at the modulation frequency 8.33 Hz. The phase for T_e is not shown as it is within the noise level.

modulation of the electron density n_e ($< 1\,\%$), electron temperature T_e ($< 1\,\%$), and ion temperature T_i ($3\,\%$) at the radial location $\rho_{tor} = 0.1$ were examined. Time traces of these signals as well as of the plasma stored energy (WMHD) are shown in figure 5.4 a,b, and d. Note that these $<1\,\%$ and $3\,\%$ temperature modulations are near the plasma center where the ICRH is deposited and where the perturbation is the largest. The amplitude profiles of the T_e (orange) and T_i (blue) modulations are shown in figure 5.5 and one can see that they are consistent with direct heating by the ICRH as they peak in the center and have a minimum in phase (T_i only) at this location as well. The phase for T_e is not shown as it is within the noise level and, therefore, not meaningful. We define our region of interest to start at $\rho_{tor} = 0.25$, since these quantities are $< 1\,\%$ outside of this location. The even smaller perturbation observed in the n_e profile (not shown) is a very good sign that transport is not changing as a result of the applied perturbations.

The steady-state boron density profile n_0 as well as the phase and amplitude profiles of the boron modulation are presented in figure 5.6. The red points are the mean experimental data points. By fitting the experimental data $n_B(r_l, t_k)$ (left hand side of figure 5.2) with the function presented in equation (5.2), the phase and amplitude profiles can be calculated from the coefficients $a(r)$ and $b(r)$, where the amplitude is given by $\sqrt{a(r)^2 + b(r)^2}$ and the phase by $\arctan(a(r)/b(r))$. This will give a phase in units of radians, but it is more intuitive to have the phase in units of seconds, since it represents the propagation time of the modulation. The conversion from radians to seconds can be obtained by dividing the phase, in radians, with $2\pi f$, where f is the frequency of the modulation. The steady-state profile is simply given by $n_0(r)$ in
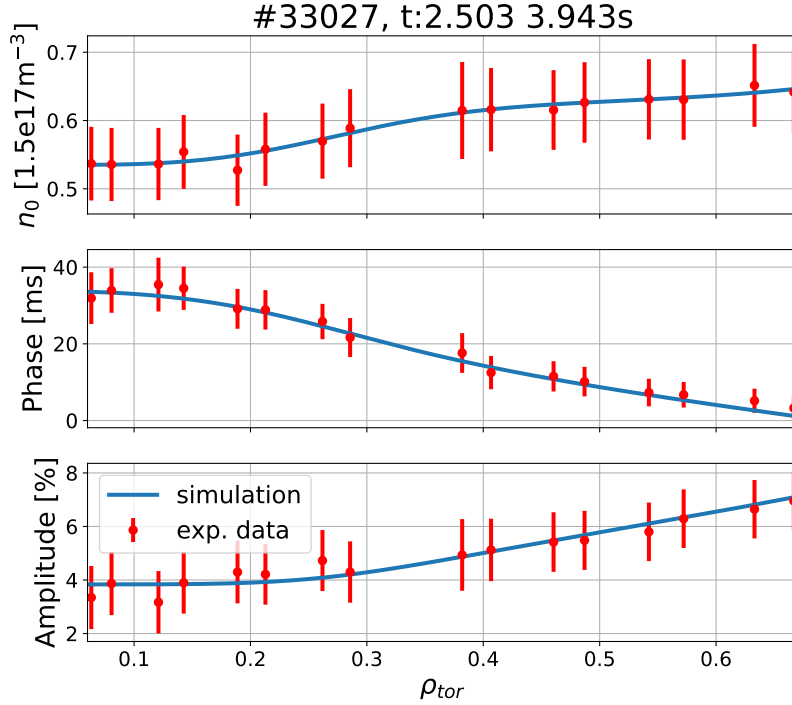
Figure 5.6.: Steady-state, phase, and amplitude profiles of the measured data (red) and the simulation (blue). The blue lines are not fits to the red data points, but rather the results of the minimization.

equation (5.2). By performing the same exercise on the reconstructed data shown on the right hand side of figure 5.2, these quantities can be extracted and are represented by the blue lines in figure 5.6. Hence, the blue lines are not fits to the red data points, but rather the results of the minimization. The agreement is very good, which is a sign of the correctness of the method used. One can note several things when studying figure 5.6. First, in this particular case the steady-state boron density profile is hollow. Second, the phase shift indicates how fast the modulation propagates into the core. In this case the phase shift is about 35 ms. Third, the amplitude modulation is strongest at the edge where the boron source is located, which also becomes clear by looking at figure 5.2. In this case, the amplitude of the modulation is 7 % at $\rho_{tor} = 0.7$. The corresponding transport coefficients are presented in figure 5.7. The top plot shows the D profile and the bottom plot the v profile. As mentioned in the previous chapter, the sign convention of v is the following: a hollow density profile means an outward drift velocity e.g. $v > 0$. The opposite ($v < 0$) corresponds to an inward directed drift velocity, which means a peaked density profile. The experimental v profile is positive meaning an outward drift and this agrees with the hollow steady-state n_0 profile in figure 5.6.

5.2. Uncertainty analysis

The measurement data $n_B(r_l, t_k) = n_B^{l,k}$ is subjected to an error such that each data point is normally distributed $\mathcal{N}(n_B^{l,k}, \sigma_B^{l,k})$ with standard deviation $\sigma_B^{l,k}$. The relative
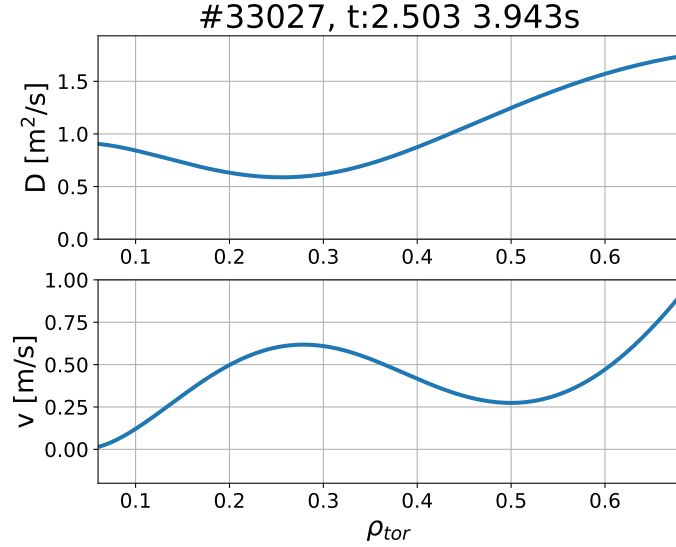
Figure 5.7.: Transport coefficient profiles: D (top) and v (bottom).

error on the boron density is difficult to assess (see discussion above) and, therefore, the error on the boron intensity $I_B^{l,k}$ is used for $\sigma_B^{l,k}$. To assess the uncertainties on the measured transport coefficients, a full Monte Carlo approach is used, where this multi-variate normal distribution of the experimental data $\mathcal{N}(n_B^{l,k}, \sigma_B^{l,k})$ is assumed. $N_S = 10000$ random samples are drawn from this distribution and every sample goes through the simulation procedure described in section 5.1.2, thus resulting in a posterior distribution. The posterior distribution itself, however, is not normally distributed even though the samples were drawn from a normal distribution. The reason for this is because the transport equation is non-linear. The uncertainty bands of the D (top) and v (bottom) profiles shown in figure 5.8 are pointwise confidence intervals of 95 % of the posterior distribution. These confidence intervals of the D and v profiles, therefore, only represent a statistical error. Other non-statistical uncertainties most certainly also play a role, but require a full Bayesian framework, which is outside the scope of this work.

5.3. Method validation

With the new ICRH modulation technique multiple modulation cycles can be measured and analyzed together on top of an otherwise constant background plasma (see figure 5.2). This is a big advantage compared to other techniques such as laser blow-off and gas puffing, which commonly determine the transport coefficients by analyzing only one single cycle, for example, one individual laser blow-off. The method presented here reduces the relative noise and has a lower statistical uncertainty.
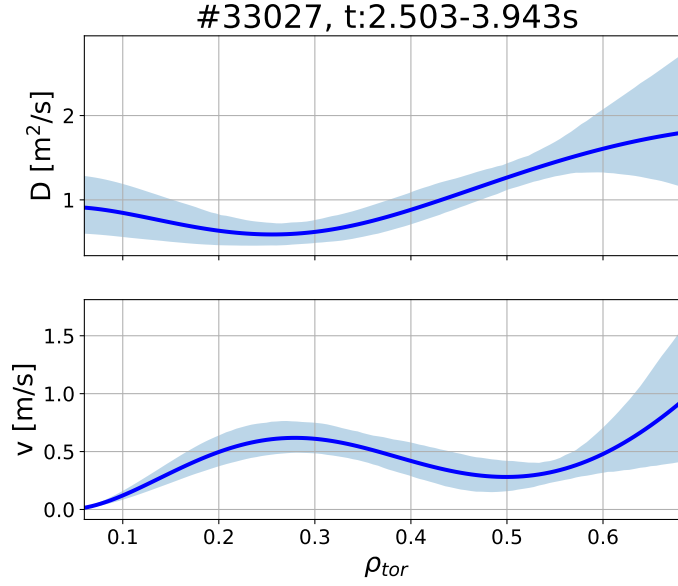
Figure 5.8.: D (top) and v (bottom) profiles including uncertainty bands deduced with a Monte Carlo approach.

5.3.1. Method of manufactured solutions

Before using the numerical simulation tool to calculate the transport coefficients, it is important to build trust in its reliability and make sure the solver has been implemented correctly. This can be done by checking whether the simulation tool accurately reproduces an analytical solution. This approach is called the Method of Manufactured Solutions [123][124]. The procedure is straight-forward: suppose the D and v profiles have been found. The transport equation can then be solved analytically for the steady-state $n_0(r)$ by integrating equation (4.15) from r to r_{max}:

$$\int_r^{r_{max}} \frac{v(r')}{D(r')}\mathrm{d}r' = \int_r^{r_{max}} \frac{1}{n_0(r')}\frac{\partial n_0(r')}{\partial r'}\mathrm{d}r'$$
$$= [\log(n_0(r'))]_r^{r_{max}} = \log(n_0(r_{max})) - \log(n_0(r)). \quad (5.12)$$

Expanding both sides yields:

$$\Rightarrow \exp\left(-\int_r^{r_{max}} \frac{v(r')}{D(r')}\mathrm{d}r'\right) = \frac{n_0(r)}{n_0(r_{max})} = \frac{n_0(r)}{s_0} \quad (5.13)$$

$$n_0(r) = \exp\left(-\int_r^{r_{max}} \frac{v(r')}{D(r')}\mathrm{d}r'\right)s_0. \quad (5.14)$$

By inserting analytical D and v profiles in equation (5.14), an analytical expression for $n_0(r)$ can be calculated. The analytical $n_0(r)$ is compared to the the $n_0(r)$ obtained by inserting the same analytical D and v profiles into the second order finite difference solver for the transport equation. If the two different approaches give the same $n_0(r)$, the radial transport solver has been correctly implemented. This test was performed and the normalized analytical steady-state $n_0(r)$ (blue) and the steady-state $n_0(r)$ obtained from the solver (orange) are presented in figure 5.9. The agreement is perfect
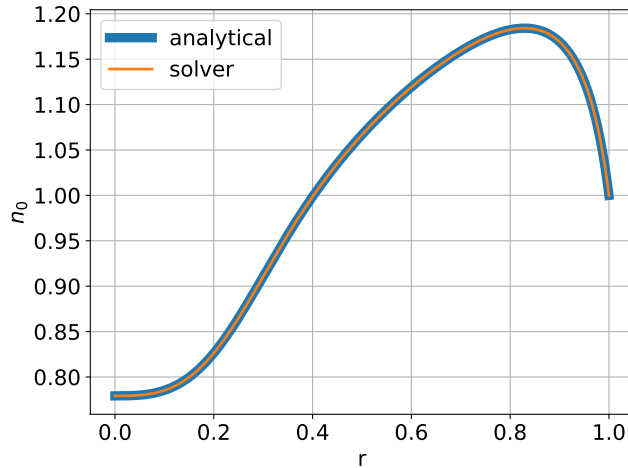
Figure 5.9.: Code verification with the the Method of Manufactured Solutions. The blue curve represents the normalized analytically calculated steady-state n_0 and the orange curve is the steady-state acquired from our radial transport solver.

and it can, thus, be concluded that the radial transport solver has been correctly implemented.

5.3.2. Feature resolution

To investigate what features can be resolved in the transport coefficient profiles with the AUG CXRS diagnostics, further method validation was performed. Synthetic D and v profiles were given to the radial transport solver and the steady-state n_0 density, phase and amplitude profiles were calculated (see section 5.1.3 on how the phase and amplitude are calculated). In the following examples, the frequency of the modulation was 10 Hz.

First, the D and v profiles (blue lines called *True* in figure 5.10) were scaled with a factor of 1.3 (dashed orange lines in figure 5.10). Additionally in red, example experimental data points with typical error bars are plotted for the steady-state density, phase, and amplitude to display what kind of features we are able to measure with our CXRS systems. It should be noted that our CXRS diagnostic has three times as many data points, but for the sake of clarity only a few are shown. As already discussed in the introduction, scaling both the D and v profiles with the same factor does not influence the steady-state density profile, since it depends on the ratio v/D, but it does affect the phase and amplitude profiles. When increasing the transport coefficients, the phase shift decreases meaning the modulation propagates more quickly from the edge into the core. In this example, multiplying the transport coefficients by a factor of 1.3 results in a change of the phase shift from 40 ms to 30 ms. Additionally, the amplitude of the modulation is less damped compared to the case with the smaller D and v profiles. Hence, scaling the transport coefficients with a larger factor would result in a faster inward propagation and less damping. Judging from the error bars on the phase and amplitude in figure 5.10, a change resulting from a smaller factor than 1.3 in the transport coefficients cannot be distinguished outside of the error bars with the CXRS
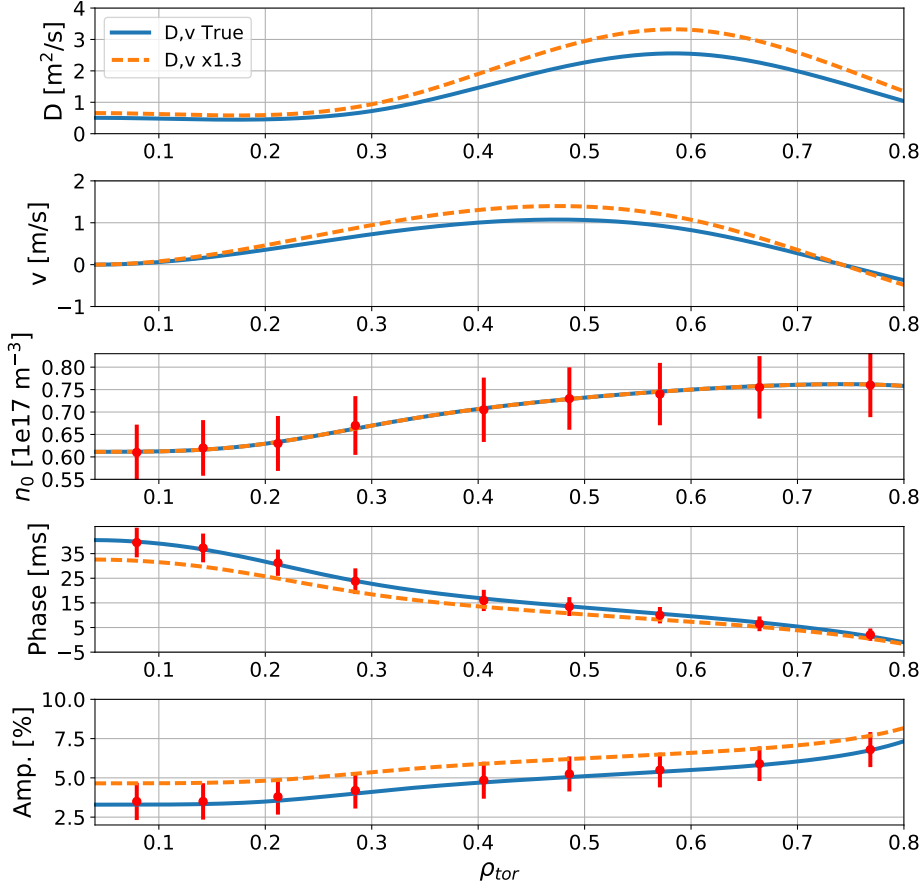
Figure 5.10.: Synthetic D and v profiles and the resulting steady-state, phase, and amplitude profiles. Dashed orange lines: Blue D and v (called D, v True) profiles multiplied by a factor of 1.3. Example experimental data points and error bars in red to display what kind of features we are able to measure with our CXRS systems. A change resulting from a smaller factor than 1.3 in the transport coefficients cannot be distinguished outside the error bars with the CXRS diagnostic.

diagnostic.

The second task was to investigate how a potential MHD mode could affect the profiles. Such a mode could, for example, enhance the transport locally and, thus, give rise to a sharp localized peak in the D profile. The resultant steady-state density, phase and amplitude profiles from such hypothetical D profiles (keeping the v profile constant) are shown in figure 5.11. The blue lines correspond to the same profiles shown in figure 5.10. For the dashed magenta lines, a sharp Gaussian peak in D has been added around $\rho_{tor} = 0.33$, to simulate a 3/2 neoclassical tearing mode (NTM) [125]. This sharp rise in the D profile leads to a flattening of the steady-state profile n_0 at $\rho_{tor} = 0.33$ as well as in the phase and the amplitude profiles. This flattening is still within the experimental error bars for the steady-state and the amplitude, but on the borderline for the phase. It is also interesting to investigate how the sharpness of such a peak affects the profiles. The result of such an investigation is displayed in figure 5.12. The blue lines are, again, the original profiles and the width of the added Gaussian peak has consequently been increased for the dashed green, magenta, and orange lines. One can see that increasing

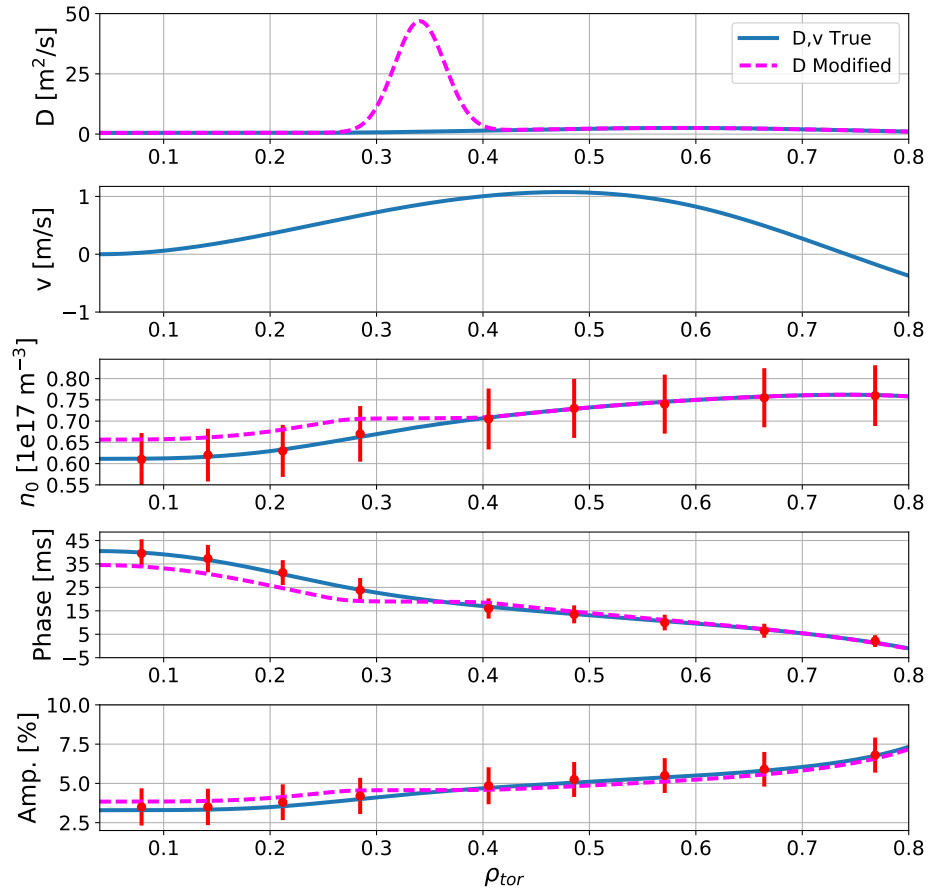Figure 5.11.: Synthetic D and v profiles and the resulting steady-state, phase, and amplitude profiles. To simulate a MHD mode, a peak in the D profile has been added (dashed magenta lines) on top of the original profile (blue lines). The v profile was kept constant. Example experimental data points and error bars in red to display what kind of features we are able to measure with our CXRS systems.

the width also leads to a flattening of the steady-state, phase, and amplitude profiles. Here, the green case is well within the experimental error bars, the magenta case is borderline for the steady-state and phase, but the orange case is outside the error bars for the steady-state and phase. It is obvious to see that such a small feature in the dashed green steady-state profile can probably not be distinguished from the blue case within the error bars, whereas it should not be a problem to distinguish between the orange and the blue cases. However, given the width of the peak in the magenta and orange case, the peak cannot be classified as localized anymore. The fact that a very large change in the D or v profile only leads to small changes in the experimental data, that is in the steady-state, phase, and amplitude, stems from the ill-posedness of the inverse problem. This further strengthens the argument that when solving such an inverse problems, some kind of regularization must be applied in order to heal the ill-posedness. To conclude, it would be difficult to distinguish a mode outside of the error bars with our CXRS systems, since such a mode has to cause a peak with a very high diffusion and/or be very broad, in which case the mode would not be localized anymore.

5.3.3. STRAHL benchmark

As an additional check, our radial transport solver was benchmarked against the impurity transport code STRAHL [126], which solves the forward problem. The final D and v profiles from our solver were given to STRAHL as inputs to cross check the simulated steady-state density n_0 and the phase and amplitude of the modulation (see section 5.1.3 on how the phase and amplitude are calculated). As can be seen in figure 5.13, there is an excellent agreement in all quantities between the two codes. However, the radial transport solver developed in this work was able to perform one forward calculation in a few milliseconds, whereas STRAHL, which deploys an additional computational expensive time discretization using the Crank-Nicolson scheme, needs several seconds for the same task. In fact, in some cases the complete minimization procedure is finished in the same time it takes STRAHL to complete one forward calculation. The fact that the inverse problem can be solved in a few seconds makes it possible to carry out the brute force uncertainty estimation, described in section 5.2, in a couple of hours. For such an analysis STRAHL would require several days.

5.3.4. Alternative methods

Apart from solving the inverse problem, there exist other simpler yet flawed methods of calculating the transport coefficients. These methods are here briefly reviewed and compared to the method previously outlined in this chapter.
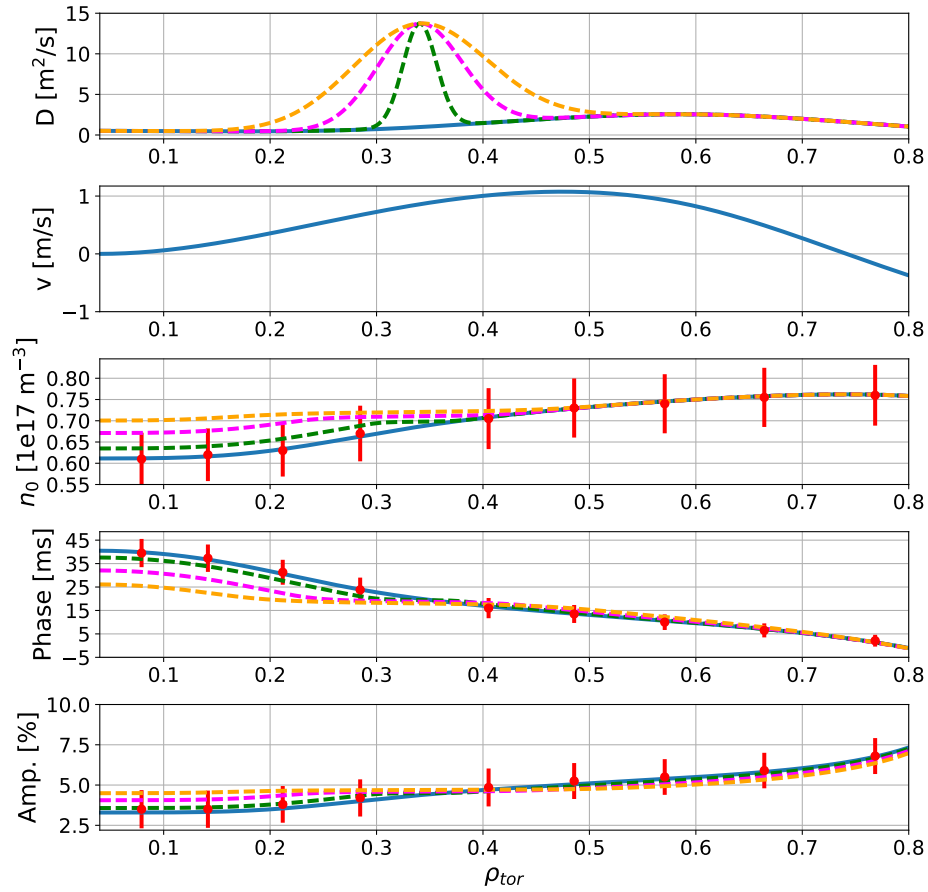
Figure 5.12.: Synthetic D and v profiles and the resulting steady-state, phase, and amplitude profiles. To simulate a MHD mode, peaks in the D profile with different widths have been added (dashed green, magenta, and orange lines) on top of the original profile (blue case). The v profile was kept constant. Example experimental data points and error bars in red to display what kind of features we are able to measure with our CXRS systems.
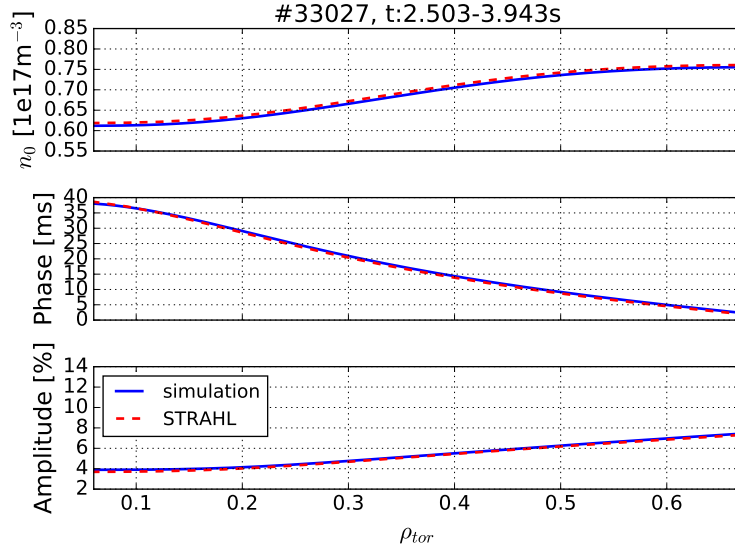
Figure 5.13.: Result of the benchmark of our radial transport solver (blue) with the impurity transport code STRAHL (red). There is a very good agreement in all quantities between the two codes.

Direct inversion

Starting from equations (5.5) and (5.6), analytical expressions for D and v can be derived:

$$D(r) = -\frac{\omega \int_0^r a(\tilde{r})\tilde{r} \; \mathrm{d}\tilde{r}}{r \left(b'(r) - \frac{n_0'(r)}{n_0(r)}b(r)\right)} = \frac{\omega \int_0^r b(\tilde{r})\tilde{r} \; \mathrm{d}\tilde{r}}{r \left(a'(r) - \frac{n_0'(r)}{n_0(r)}a(r)\right)} \tag{5.15}$$

$$v(r) = \frac{n_0'(r)}{n_0(r)}D(r) = -\frac{\omega \; n_0'(r) \int_0^r a(\tilde{r})\tilde{r} \; \mathrm{d}\tilde{r}}{r \left(n_0 b'(r) - n_0'(r)b(r)\right)}. \tag{5.16}$$

The full derivations of equations (5.15) and (5.16) are outlined in appendix A.1. Unfortunately equations (5.15) and (5.16) require three continuous functions, the steady state profile $n_0(r)$ and the real and complex part of the modulated density $a(r)$ and $b(r)$. Given time dependent measurements of the density such continuous profiles can be obtained by several forms of regression. The most common way is spline interpolation with an additional smoothing constraint which can be chosen arbitrarily. Unfortunately this does not, in any way, guarantee that the collection of n_0, a, b actually is a solution to the radial transport equation, which is the key requirement in the derivation of equations (5.15) – (5.16). Solving the inverse problem circumvents this problematic point. Since the integral equations (5.15) and (5.16) contain derivatives of the profiles n_0, a, b, the result heavily depends on the smoothness of the corresponding regression fit. This again demonstrates why the problem is ill-posed. Reconstructing a density by the well-posed inverse Ansatz using the B-Spline representation as described in 5.1.2 provides n_0, a, b, which lie close to the measurements, have the sufficient smoothness and are actual solutions to the radial transport equation. The resulting transport coefficients are compared to the ones obtained with the numerical framework in figure 5.14, where the dashed orange lines represent D and v from the analytical expressions and the solid blue lines from the numerical scheme. As can be seen the agreement is perfect,
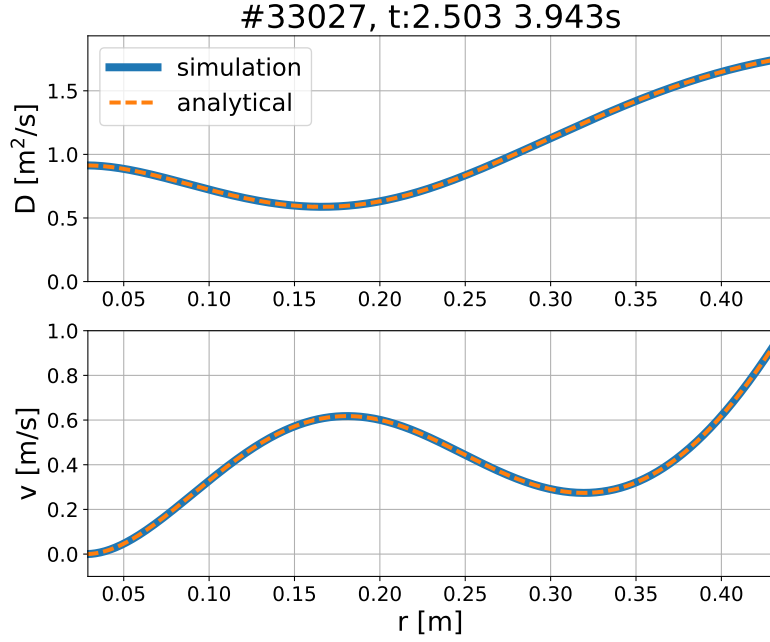
Figure 5.14.: D and v profiles computed with the the numerical scheme (solid blue) and the analytical expressions (dashed orange).

because it is only up to the discretization error of the radial transport solver and the second order finite difference discretization of the integrals in equations (5.15) − (5.16). This reflects back on the fact that both the analytical expressions and the radial transport solver use the same Ansatz for the boron density, and that this Ansatz describes the measured signal extremely well.

Gradient-flux method

Another common method of computing the transport equations is with the so-called "Gradient-flux (GF)" method [58, 87]. This method is based on the fact that the transport equation can be expressed as a linear relationship between the normalized flux $\Gamma(r,t)/n(r,t)$ and the normalized density gradient $\partial_r n(r,t)/n(r,t)$:

$$\frac{\Gamma(r,t)}{n(r,t)} = -D(r)\frac{1}{n(r,t)}\frac{\partial n(r,t)}{\partial r} + v(r), \tag{5.17}$$

where the flux $\Gamma(r,t)$ is computed as:

$$\Gamma(r,t) = -\frac{1}{r}\int_0^r \frac{\partial n(\tilde{r},t)}{\partial t}\tilde{r}\mathrm{d}\tilde{r}. \tag{5.18}$$

The transport coefficients can be acquired by fitting the experimental data with the relation (5.17), where D is obtained from the slope and v from the offset. To compute the derivative and the integral it is, again, necessary to obtain a smooth representation of the experimentally measured density n. Due to the ill-posedness of the problem, the calculated coefficients highly depend on the parametrization of the measured density. Therefore, the Ansatz (5.2) was used also here for the parametrization. The resulting D and v profiles are presented in figure 5.15. The coefficients obtained with the GF
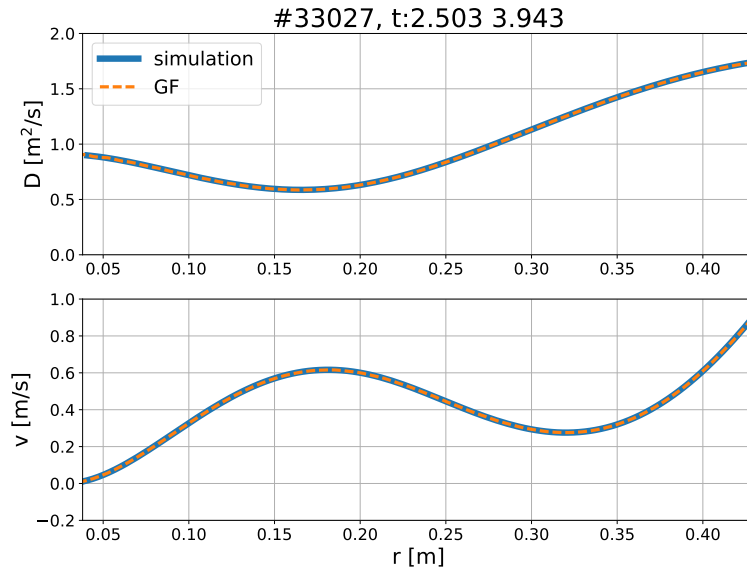
Figure 5.15.: D and v profiles computed with the the numerical scheme (solid blue) and the gradient-flux method (dashed orange).

method (dashed orange) agree well with the ones computed with the numerical scheme (solid blue) when using this parametrization. This further shows that the Ansatz (5.2) describes the measured boron modulation signal very well.

Conclusion

The result of the χ^2-regression, that is, the solution to the minimization problem in equation (5.1), maximizes the likelihood of observing the measured data for a given D and v. This means that given the measured data we find the most likely D and v profiles and this procedure is, hence, also known as the maximum likelihood estimator for normally distributed measurements. This is the reason why fitting data with least square is very popular and works so well. The key difference between the direct inversion and the gradient flux method, on the one side, and the inverse problem, on the other side, is that the former two methods first search for a density that is most likely to fit the data and infers the transport coefficients afterwards whilst neglecting the radial transport equation as a constraint. The latter method, however, directly finds the most likely transport coefficients given the measured data, the radial transport equation, and assuming normal errors. Since we are primarily interested in the transport coefficients the inverse problem is the right method of choice. In combination with the solution to the inverse problem, the direct approaches are, however, perfectly suited methods of validation, as can be seen figures 5.14 and 5.15, but one should be extremely careful when calculating the transport coefficient using only such a method.

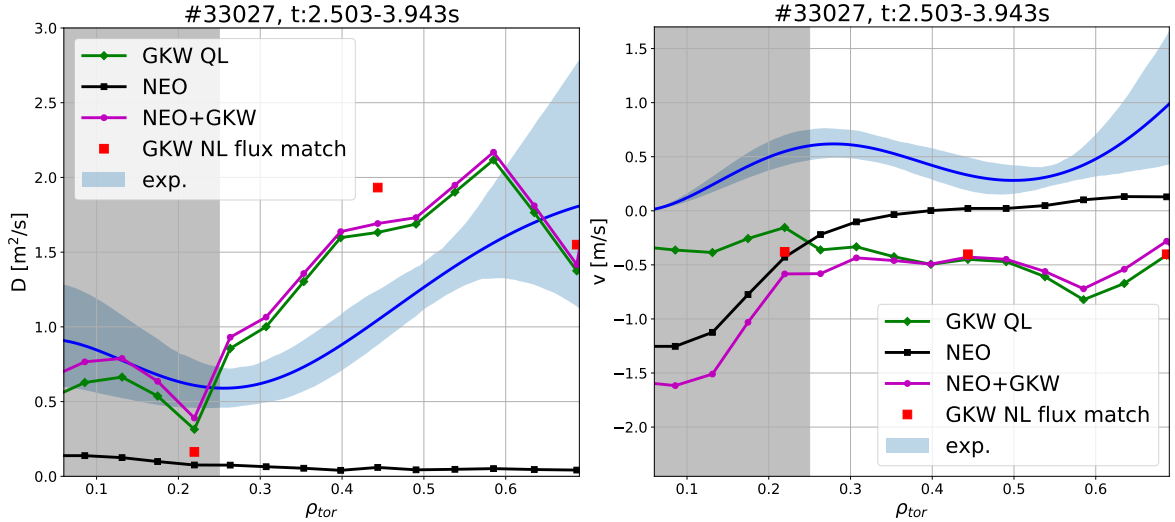Figure 5.16.: Experimental and theoretical D (left) and v (right) profiles. The experimental profiles with their uncertainty bands are depicted in blue, the ones from the quasi-linear GKW run in green diamonds, from NEO in black squares, and the total theoretical profiles in magenta circles. The red squares represent the result of the non-linear GKW run performed with matching of the heat fluxes. Our region of interest starts at $\rho_{tor} = 0.25$, hence, where the gray region ends.

5.4. Comparison to theory

The transport coefficients deduced from the experimental data presented in this chapter are compared with neoclassical calculations, performed with the code NEO [74, 75], as well as quasi-linear gyrokinetic simulations at a turbulent wavenumber $k_\theta \rho_i = 0.4$, computed with the code GKW [76]. How the turbulent component, from the quasi-linear GKW simulation, and the neoclassical component are added together are described in detail in section 6.3.4. The comparison of the theoretical transport coefficients with the experimental ones are shown in figure 5.16, where the experimental coefficients are displayed in blue, the neoclassical in black, the quasi-linear in green, and the sum of the neoclassical and quasi-linear in magenta. Neoclassical diffusion is, as expected, much smaller than the measured values, and hence, the transport is turbulence driven. In this case, the total theoretical D agrees reasonably well (within a factor of 2) with the experimental one, whereas the theoretical v is in the opposite direction. The experimental v profile is positive (outward), which agrees with the hollow steady-state n_0 profile in figure 5.6. Since the theoretical drift velocity is negative, the theory fails to capture this and instead predicts considerably more peaked steady-state profiles than are measured. The uncertainty regions of the D and v profiles in figure 5.16 are calculated as described in section 5.2. The end of the gray region indicates where our region of interest starts ($\rho_{tor} = 0.25$).

To investigate how large an impact the ion temperature modulation has on the transport coefficients calculated by GKW, additional simulations with an averaged maximum and an averaged minimum T_i profile were performed. Maxima and minima of the T_i modulation were identified and from these, average maximum and minimum T_i profiles were created which were then used as inputs to GKW. The resultant transport
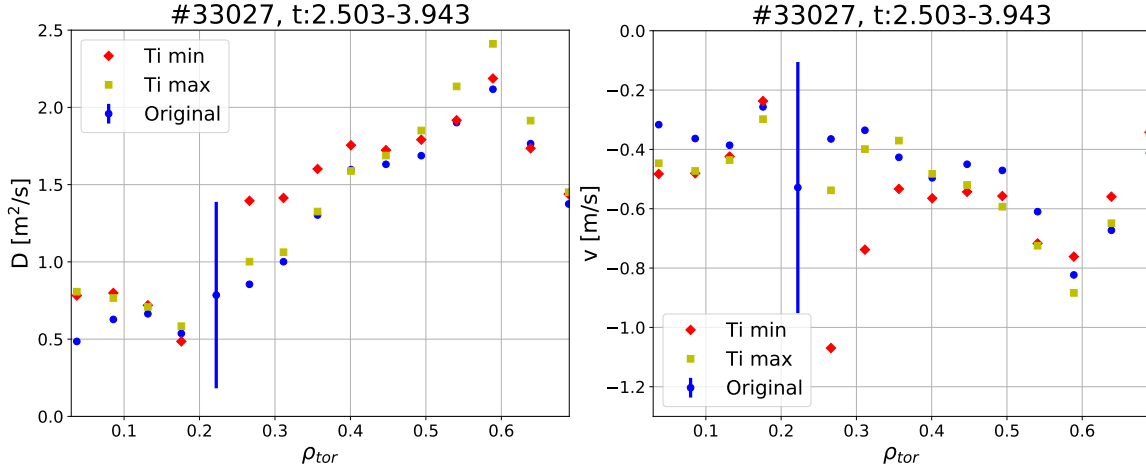
Figure 5.17.: D (left) and v (right) profiles (blue points) from GKW. The error bar at $\rho_{tor} \sim 0.22$ shows how D and v change in the runs with the average maximum and minimum T_i profile at this particular location. The rest of the data points from these additional runs are shown as red diamonds (T_i minimum) and yellow squares (T_i maximum) and show significantly less variation than at $\rho_{tor} \sim 0.22$.

coefficients of the new runs (red diamonds and yellow squares) closely follow the original run (blue) except at $\rho_{tor} = 0.22$. This is indicated by the error bar in figure 5.17. The reason for the different result is that this location is highly sensitive to the choice of the spectrum in the calculation of the quasi-linear transport. Different branches are competitively almost equally unstable, but produce very different impurity transport. It can thus be concluded that, overall, the change in the ion temperature gradient due to the small modulation present does not impact the predicted transport coefficients from GKW.

As a consistency check, non-linear GKW runs, both with and without heat flux matching between theory and experiment, at three radial locations were performed. The results of these runs can be seen in figure 5.18, where D/χ_i (top) and v/χ_i (bottom) profiles are plotted. The quasi-linear results are shown in green, the non-linear without heat flux matching in magenta, and the non-linear with heat flux matching in red. Additionally, the experimental profiles are shown in blue. The experimental χ_i is the anomalous part of the power balance heat conductivity calculated with TRANSP [127] and the turbulent χ_i is calculated by GKW. As can be seen, the non-linear results agree well with the quasi-linear results, except for the data point at $\rho_{tor} = 0.22$, but this comes as no surprise since that point is much more sensitive to the choice of the turbulent wave number (see figure 5.17 and discussion above) and the non-linear result includes all unstable modes, while the quasi-linear one is only based on the most unstable one [82]. For D/χ_i, the experimental result is of order unity. While in the dimensionless parameters D/χ_i and v/χ_i there is a good correspondence between non-linear and quasi-linear results in figure 5.18, some differences are particularly visible when the comparison is performed between the dimensional quantities (D in m²/s and v in m/s) as was done in figure 5.16; the non-linear results with heat flux matching are shown in red in figure 5.16. This is because the ion temperature gradients which have been used to match the heat flux had to be modified with respect to the nominal
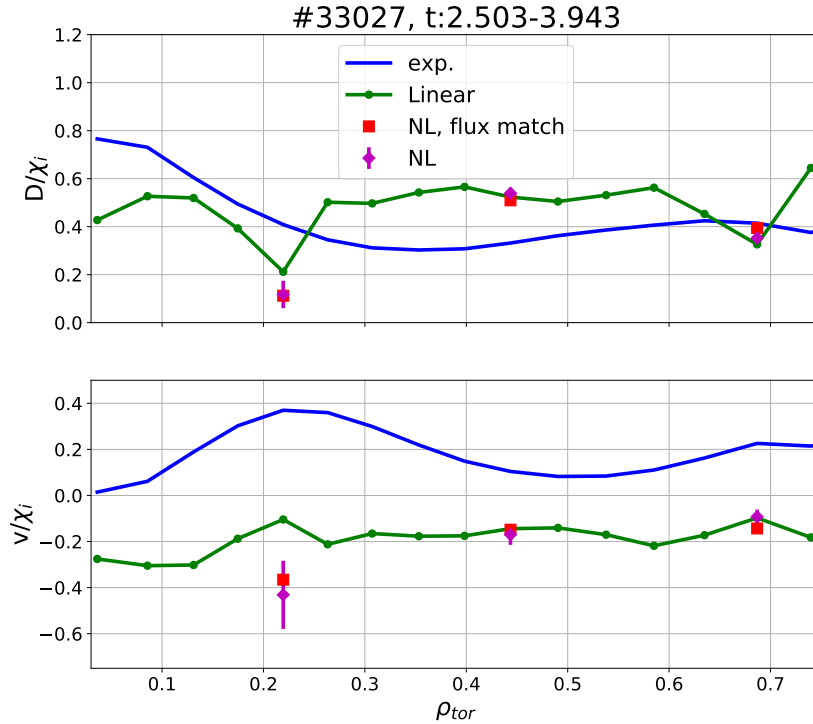
Figure 5.18.: D/χ_i (top) and v/χ_i (bottom) profiles from GKW comparing the results from the quasi-linear (green line) with the non-linear without flux matching (magenta diamonds), and non-linear with flux matching (red squares) runs. The experimental profiles are shown in blue.

values. This is particularly visible for the D values around mid-radius, for which the logarithmic ion temperature gradient had to be decreased by almost 20 %, with a consequent increase of the local value of the corresponding heat conductivity. In contrast, for the inner and outer points, the logarithmic ion temperature gradients had to be increased by less than 10 % in order to match the anomalous part of the ion heat flux computed with TRANSP.

5.5. Conclusion

In this chapter a novel method of inducing a time perturbed modulation of the boron content in the plasma by modulating the ICRH power has been presented. The technique has been thoroughly tested and applied under several different plasma conditions. To illustrate the method one experimental example is shown in detail in this chapter. This method requires CXRS data of good quality, i.e. high spatial and temporal resolution. With a time-dependent boron density signal at hand, the boron transport coefficients D and v in the radial transport equation can be individually determined. It was shown that this task can be done by solving an inverse problem by a quasi-Newton method. The functional form assumed for the boron density is a background steady-state component plus a sum of a cosine and sinus with the frequency of the modulation. Hence, a second requirement is that the boron density signal can be well represented by the sum of a few sinusoidal terms. This implemented framework has

been verified with the Method of Manufactured Solutions as well as benchmarked with the transport code STRAHL. Additionally, the deduced transport coefficients have been compared to other simpler methods like analytical expressions of D and v as well as the Gradient-flux method. The uncertainties of the transport coefficient profiles are estimated with a Monte Carlo procedure, where random samples are drawn from a multi-variate normal distribution of the experimental data. The transport coefficients are assumed to be constant in time, which requires a constant plasma background. This implies that the resultant modulation of the electron density, electron temperature, and the ion temperature should be kept as small as possible. In this example, it was observed that the modulation of the electron density, temperature, and the ion temperature are less than 1% in the radial region of interest ($\rho_{tor} > 0.25$), whereas the boron density modulation amplitude is 4% in the core and 7% at the edge.

The experimental transport coefficients are compared with neoclassical calculations with the code NEO and quasi-linear and non-linear gyrokinetic simulations with the code GKW. Neoclassical D values are well below the experimental ones meaning the transport is turbulence driven. The comparison to gyrokinetic theory shows an agreement within a factor of 2 in D, but the theoretical v has the opposite sign, i.e. predicts a more peaked steady-state boron density profile than measured in the experiment. Additional non-linear GKW runs have been carried out and the non-linear results agree well with the linear ones.

The analysis enables us to measure core boron transport coefficients over a wide range of plasmas with error bars on the order of 30%. Moreover, this technique and solver are directly applicable in other situations as long as the studied impurity can be measured with high spatial and temporal resolution and there exists a way of modulating the impurity density at the edge in such a way that the resultant density signal is of a sinusoidal form. This method has been exploited in different plasma conditions and a database of transport coefficients has been assembled. Whereas this chapter only showed one example, the complete database of transport coefficients will be presented in the next chapter along with a comparison to previous boron transport studies at AUG and with the theoretical predictions.

Chapter 6.

Experimental boron transport results at ASDEX Upgrade

Chapter 5 described a new method of inducing a time-dependent boron density signal and the framework built up to deduce the individual transport coefficients from the measurement. One experimental example was presented in order to show how the method works and the transport coefficients of this particular example were also compared to the theoretically predicted ones. Over the course of this work, this method has been utilized in various plasma experiments and a database of boron transport coefficients has been gathered. This database will be presented in this chapter along with the theoretical predictions from neoclassical and turbulent transport theory. Even though helium and other heavier impurities such as tungsten, originating from the plasma-facing components, are of higher interest for a future fusion reactor, the study of the low-Z impurity boron remains of high interest as it enables us to validate our theoretical understanding of impurity transport, which in turn enables the accurate prediction of how other impurities will behave in a future reactor. This study focuses on the core transport of boron, that is the transport around mid-radius in the confinement region. The correlations between the transport coefficients and plasma parameters will be compared to the theoretical predictions in this plasma region.

6.1. Experimental database

Several plasma discharges, all H-mode plasmas in lower single null (LSN) configuration, were performed during the course of this work to assemble a database of boron transport coefficients. In total the database is comprised of 20 observations. The experiments were performed relatively close to a boronization in order to obtain a good charge exchange signal as well as a clear boron modulation signal. In these experiments the magnetic field was $2.5\,\mathrm{T}$ and the plasma current was either $600\,\mathrm{kA}$ or $800\,\mathrm{kA}$. As described in the previous chapter, to create a time perturbed boron density signal, the ICRH power was modulated with a frequency of $8-10\,\mathrm{Hz}$. In the off-phase the ICRH power was zero and in the on-phase $1\,\mathrm{MW}$. Every observation includes a segment of $6-12$ ICRH duty-cycles during which the other heating sources are kept at a constant level. This means that one segment is 1 to 2 seconds long and this significantly limits the total number of measurements that can be made. For each of these segments, the analysis procedure described in the previous chapter was applied in order to deduce the transport coefficients. In the database, the NBI and ECRH powers were varied between

n_e [1e19 m^{-3}] ($\rho_{tor}=0$)	$5.6-8.5$	R/L_{n_e}	$0.2-3.0$
T_e [keV] ($\rho_{tor}=0$)	$2.9-4.5$	R/L_{T_e}	$4.3-9.2$
T_i [keV] ($\rho_{tor}=0$)	$1.4-4.8$	R/L_{T_i}	$4.0-8.0$
T_e/T_i	$1.0-1.3$	q_{95}	$5.0-7.3$
u'	$-0.2-1.3$	ν_{eff}	$0.4-1.2$
$M=$ deuterium Mach number	$0.09-0.21$		

Table 6.1.: Parameter space of the database at a radial location of $\rho_{tor}=0.5$.
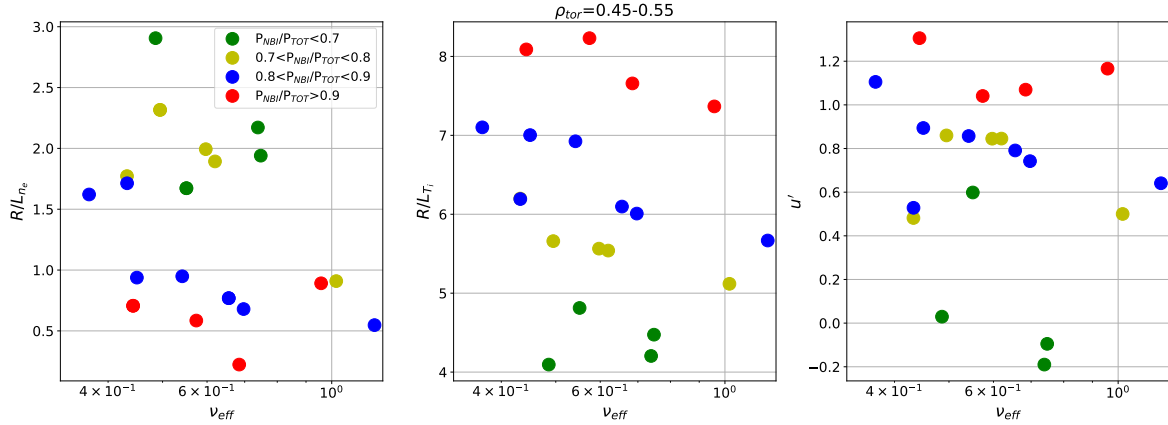
Figure 6.1.: Parameter space explored in the boron database at $\rho_{tor}=0.5$. Normalized logarithmic electron density gradient (left), normalized logarithmic ion temperature gradient (middle), and u' (right) as a function of the effective collisionality.

$2.5-10$ MW and $0-2$ MW, respectively, hence, for the bulk of the database NBI is the main heating source. To enable boron CXRS measurements of good quality at AUG, a minimum of 2.5 MW of NBI power is necessary when performing these experiments. With these variations of the actuators we were able to span the parameter space at $\rho_{tor}=0.5$ presented in table 6.1. The central electron and ion temperatures were varied between $2.9-4.5$ keV and $1.4-4.8$ keV, respectively. The obtained variation in the central electron density was $5.6-8.5\cdot10^{19}$ m^{-3}. In figure 6.1, the covered parameter space at $\rho_{tor}=0.5$ of the database is shown. The effective collisionality ν_{eff}, which is defined as the ratio of the electron-ion collision frequency to the curvature drift frequency (see section 4.3), was varied by a factor of 3 in the database.

In the previous chapter is was explained that for the method to be valid, the modulation of the background plasma should be as small as possible. The induced modulation on the electron density, electron temperature, and the ion temperature were indeed kept below 4 % for the whole database. Sawteeth were present in some of the discharges. In those cases the sawtooth frequency was $16-20$ Hz and the inversion radius $\rho_{tor}<0.25$. Type-I ELMs were present in almost all of the discharges in the database, however, they only affected the pedestal, outside of $\rho_{tor}>0.80$. The ELM frequency was between 100 Hz and 200 Hz meaning that the deduced transport coefficients are ELM-averaged. The electron temperature and density profiles were derived from the IDA framework [31] (see chapter 2), whereas the ion temperature and toroidal rotation velocity were measured with the CXRS diagnostics (see chapter 3). The boron inten-
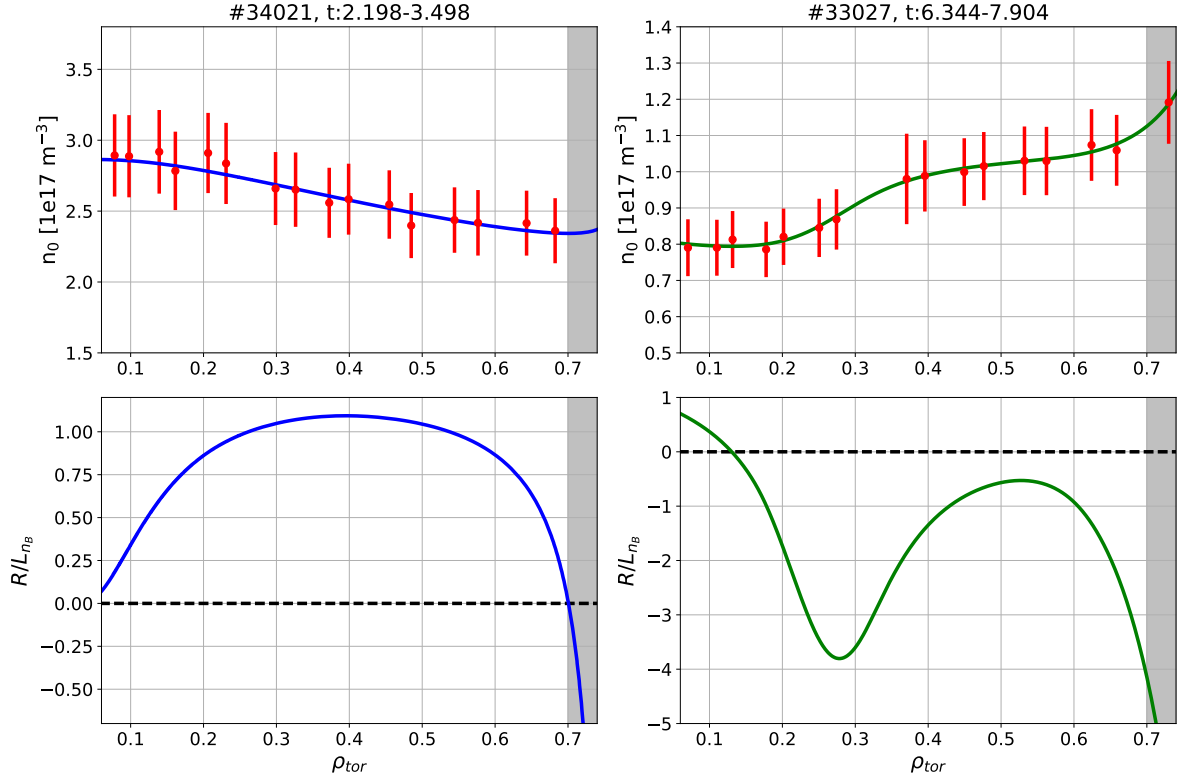
Figure 6.2.: Example steady-state boron profiles (top) and corresponding normalized logarithmic boron density gradient (bottom). The left side shows a peaked profile and the right side a hollow profile. The region of interest is inside $\rho_{tor} < 0.7$ (left of the gray region).

sity was also measured with the CXRS diagnostics and the boron density was then calculated with the CHICA code [42] (see section 3.5).

The measured boron steady-state profiles in the database varied from strongly hollow to peaked ones. Examples of a peaked (blue left) and a hollow (green right) boron profile along with the normalized logarithmic boron density gradients are shown in figure 6.2. The red points are the experimental data. The blue and green curves are the result of the minimization procedure described in chapter 5. In this particular example, the peaked profile was obtained with 2.5 MW of NBI and 1.8 MW of ECRH. The hollow profile had 7.5 MW of NBI and 0.5 MW of ECRH. The region of interest is to the left of the gray region ($\rho_{tor} < 0.7$). However, more data points are present further out and these are used to constrain the edge gradient. The corresponding D (top) and v (bottom) profiles are displayed in figure 6.3, where the same color coding as in figure 6.2 applies: blue corresponds to the peaked profile and green to the hollow profile. The uncertainty bands are computed as described in section 5.2. The diffusion coefficient is considerably higher in the case of the peak steady-state profile compared to the hollow case. Additionally, the peaked steady-state profile results in a negative convection (inward drift) whereas the hollow steady-state profile gives a positive v (outward drift). The fact that the density profile peaks when increasing the ECRH power has also been observed in previous transport studies conducted at AUG [57, 72].
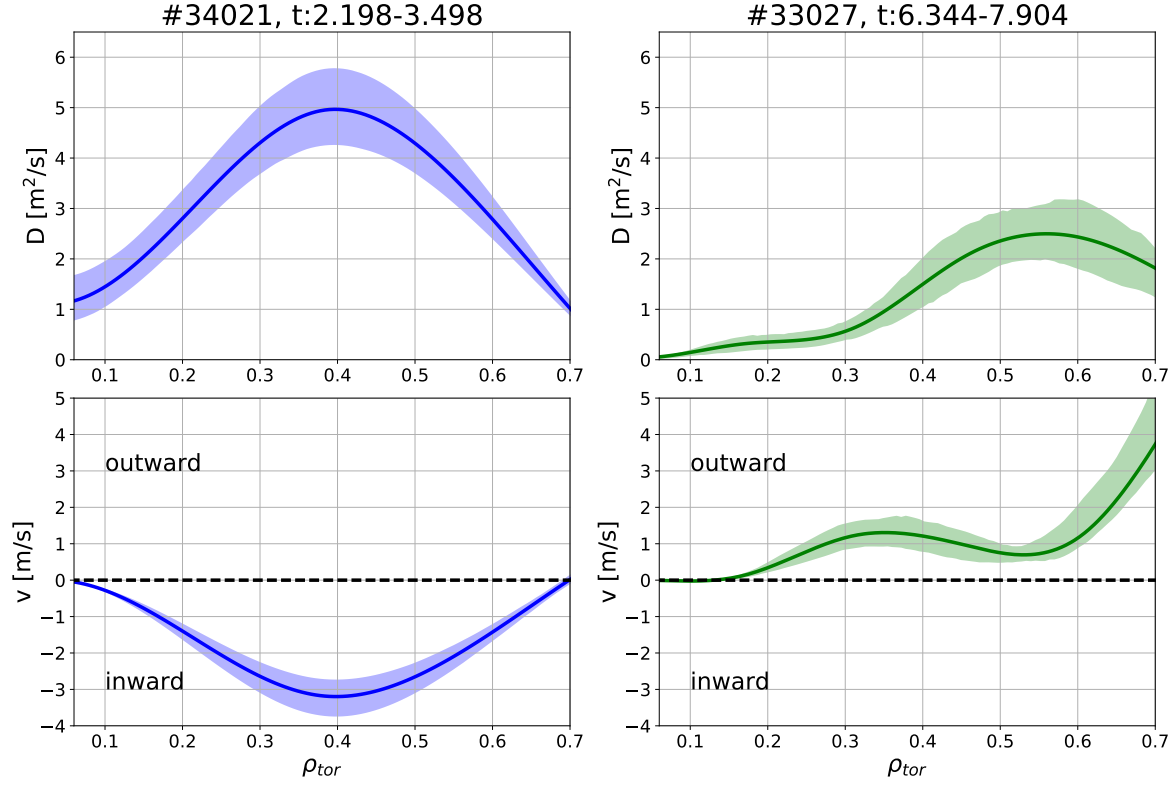
Figure 6.3.: D (top) and v (bottom) profiles of the data with the peaked (left) and hollow (right) boron density profiles in figure 6.2.

Throughout the database, correlations between the transport coefficients and other plasma parameters are observed (see table 6.2) and a few examples are shown in figures 6.4 and 6.5. In these figures, D (left) and v (right) at a radial locations of $\rho_{tor} = 0.3$ (green points) and $\rho_{tor} = 0.5$ (blue points)[1] are plotted as a function of the normalized logarithmic electron density gradient R/L_{n_e} (figure 6.4) and the deuterium Mach number M (figure 6.5); these quantities are computed at the same radial location as the transport coefficients. The Mach number is given by $M = v_{rot}/v_{th}$, where v_{rot} is the toroidal rotation velocity and $v_{th} = \sqrt{2k_B T/m}$ is the thermal velocity. The diffusion coefficient is increasing and the drift velocity is decreasing with increasing R/L_{n_e}. This is observed at both radial locations. For the Mach number, we have the opposite scalings: decreasing D and increasing v with increasing Mach number. As can be seen in table 6.2, strong correlations between the transport coefficients and other plasma parameters such as R/L_{T_i}, u', and T_e/T_i are also present, making it hard to describe the observed behavior with only one single mechanism. This is connected to the fact there exist strong correlations between these plasma parameters, for example, the Mach number itself is strongly correlated with the normalized logarithmic ion temperature gradient and the toroidal velocity gradient. What also can be seen when studying figures 6.4 and 6.5 is that the steady-state boron density profiles in the database are observed to vary from strongly hollow to peaked, with the majority of the profiles being hollow (hollow profile meaning positive drift velocity).

---

[1]The transport coefficients are averages in the ranges $0.25 - 0.35$ and $0.45 - 0.55$, respectively.

	u'	R/L_{T_i}	M	R/L_{n_e}	R/L_{T_e}	T_e/T_i	ν_{eff}	D	v
u'	1.	**0.86**	**0.89**	-0.6	0.4	-0.76	-0.15	-0.66	**0.79**
R/L_{T_i}	**0.86**	1.	**0.88**	-0.7	0.1	-0.64	-0.21	-0.61	**0.9**
M	**0.89**	**0.88**	1.	-0.65	0.22	-0.73	-0.02	-0.69	**0.83**
R/L_{n_e}	-0.6	-0.7	-0.65	1.	0.17	0.57	-0.37	**0.81**	-0.71
R/L_{T_e}	0.4	0.1	0.22	0.17	1.	-0.6	-0.36	-0.27	0.12
T_e/T_i	-0.76	-0.64	-0.73	0.57	-0.6	1.	-0.09	**0.78**	-0.68
ν_{eff}	-0.15	-0.21	-0.02	-0.37	-0.36	-0.09	1.	-0.25	-0.17
D	-0.66	-0.61	-0.69	**0.81**	-0.27	**0.78**	-0.25	1.	-0.63
v	**0.79**	**0.9**	**0.83**	-0.71	0.12	-0.68	-0.17	-0.63	1.

Table 6.2.: Correlation matrix of the different plasma parameters at $\rho_{tor} = 0.5$. Values above 0.7 are highlighted in bold.
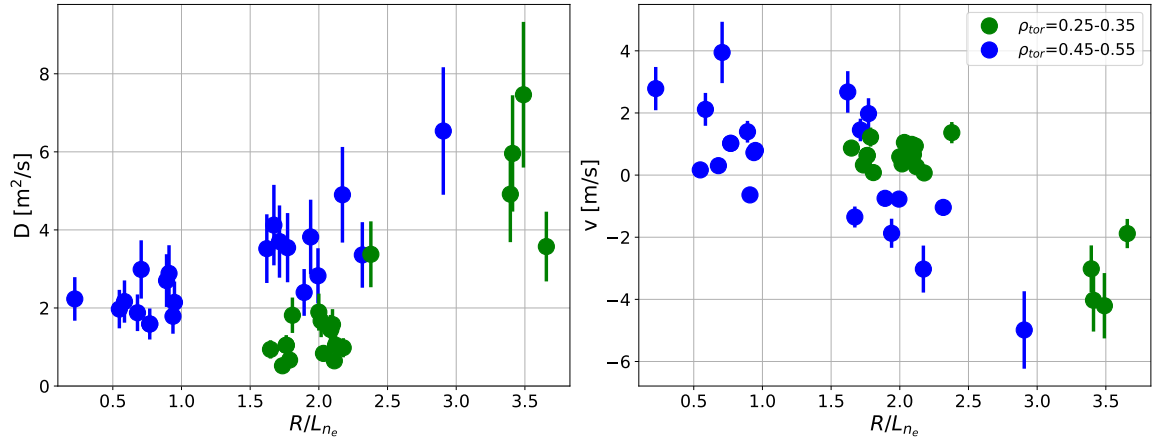

Figure 6.4.: Experimental D (left) and v (right) as a function of R/L_{n_e} at $\rho_{tor} = 0.3$ (green) and $\rho_{tor} = 0.5$ (blue).
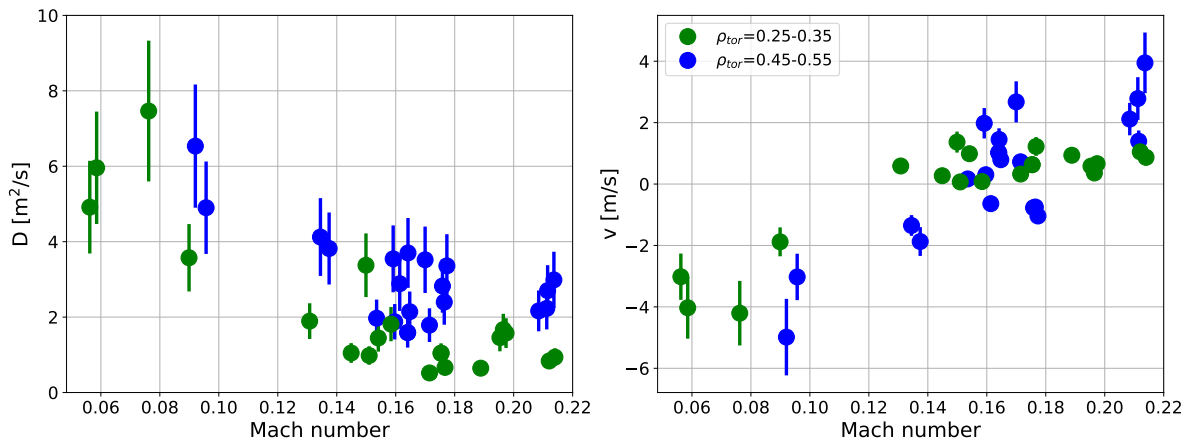

Figure 6.5.: Experimental D (left) and v (right) as a function of the deuterium Mach number at $\rho_{tor} = 0.3$ (green) and $\rho_{tor} = 0.5$ (blue).
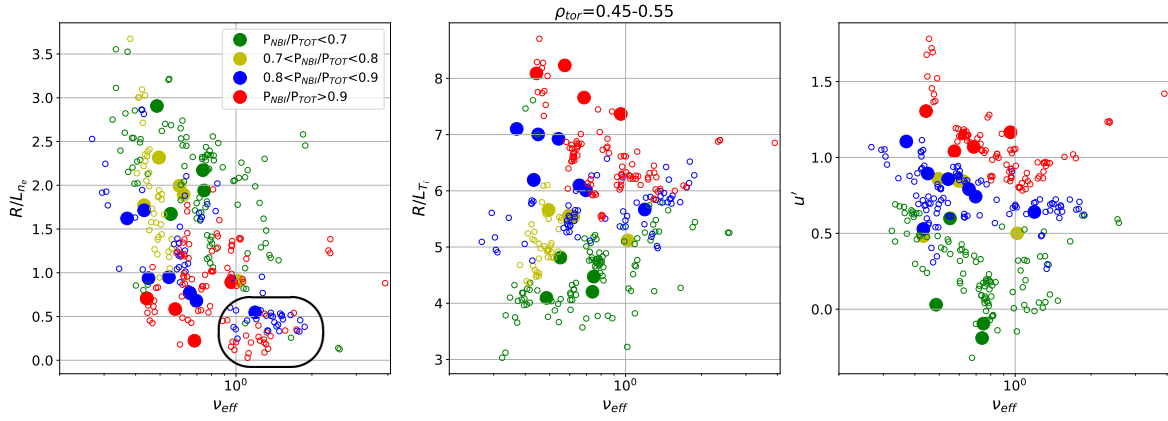
Figure 6.6.: Parameter space explored in the boron database at $\rho_{tor} = 0.5$ (filled symbols) compared to the covered parameter space in Ref. [45] (open symbols). Normalized logarithmic electron density gradient (left), normalized logarithmic ion temperature gradient (middle), and u' (right) as a function of the effective collisionality.

6.2. Comparison to previous boron transport studies at AUG

The analysis of the boron transport database presented in this work has been compared to a previous boron transport studies conducted at AUG, which looked at steady-state conditions [45]. It is worth noting that steady-state studies are able to collect significantly more data points than our transient study. In figure 6.6, the parameter space of the new data (filled symbols), which was presented in figure 6.1, is compared with a previous study (open symbols) [45]. This previous study [45] was able to span a little bit wider range of R/L_{n_e}, R/L_{T_i}, and u' than in the present study. But the largest difference is seen in ν_{eff}, which the old study was able to vary from 0.3 to 4, whereas the study presented here only achieved a variation between 0.4 and 1.2. The covered range of deuterium Mach number is almost the same ($0.09 - 0.21$ in this study versus $0.08 - 0.26$ in the previous study). In figures 6.7 and 6.8 the normalized logarithmic boron density gradient R/L_{n_B} is plotted as function of various plasma parameters for the new database (blue points) and the old database (purple points) at $\rho_{tor} = 0.5$. Since the normalized logarithmic boron gradient is related to the transport coefficients via equation (4.15), the same correlations we saw when studying D and v alone in figures 6.4 and 6.5, can also be observed when plotting R/L_{n_B}. A hollow density profile, thus, corresponds to a positive v and this in turn corresponds to a negative R/L_{n_B}, since $R/L_{n_B} = -R\nabla n_B/n_B = -Rv/D$.

In the present study the normalized logarithmic boron density gradient is always smaller than the normalized logarithmic electron density gradient, meaning that the electron density profile is more peaked than the boron density profile (see left hand side of figure 6.7). This is a highly desirable feature for a fusion reactor, since a impurity density profile that is more peaked than the main ion profile would cause impurity accumulation. For the previous study, this is not always the case (these points are visualized with red symbols in figures 6.7 and 6.8) and there is a larger scatter in the data. The majority of the red data points of the previous study in figures 6.7 and
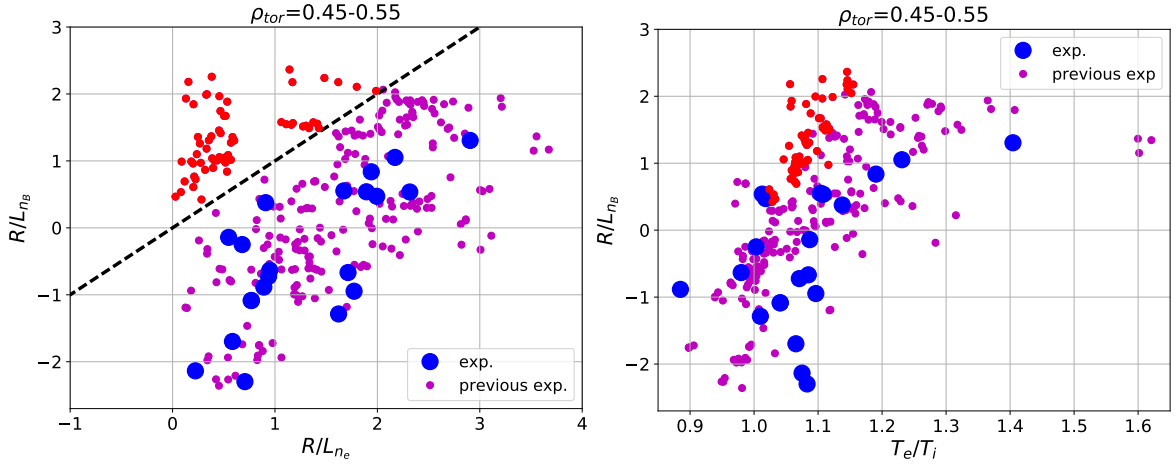
Figure 6.7.: Scatter plots of the normalized logarithmic boron density gradient R/L_{n_B} as a function of the normalized logarithmic electron density gradient R/L_{n_e} (left) and the electron to ion temperature ratio T_e/T_i (right) for the database of this work (blue points) and a previous boron transport study conducted at AUG [45] (purple and red points) at a radial location of $\rho_{tor} = 0.5$. The red data points of the previous study correspond to cases where R/L_{n_B} is bigger than R/L_{n_e}, that is the boron density profiles is more peaked than the electron density profile.

6.8, where R/L_{n_B} is bigger than R/L_{n_e}, for which we do not have an overlap with our dataset, have a relatively high collisionality ($1 < \nu_{eff} < 2$, points encircled in the left plot of figure 6.6) and a high fraction of NBI heating power ($0.8 < \mathrm{P}_{NBI}/\mathrm{P}_{TOT} < 1$). Otherwise, there is a consistency between the new and previous dataset and the same scalings between the normalized logarithmic boron density gradient and the electron to ion temperature ratio (figure 6.7 right), deuterium Mach number (figure 6.8 left), and the toroidal rotation gradient (figure 6.8 right) are observed in both. Additionally, hollow boron density profiles ($R/L_{n_B} < 0$) are obtained at low values of R/L_{n_e} and T_e/T_i and at high values of u' and Mach number. The opposite trends apply for peaked boron density profiles. Comparing R/L_{n_B} of the new database with that of the database in Ref [45], it can be seen that the older study was able to obtain higher values of R/L_{n_B} than in the present study, meaning the previous study measured more peaked boron density profiles. As already mentioned in the previous section, there is a high correlation between several of the plasma parameters (see table 6.2). Since the NBI heating does not only heat the ions but also exerts a torque on the plasma causing it to rotate, there exists a strong correlation between the toroidal rotation gradient and the normalized logarithmic ion temperature gradient (not shown). The NBI heating is also a consequence for the high correlation between the Mach number and the toroidal rotation gradient and, therefore, the similarity between figures 6.8 left and right. As already mentioned, increasing the ECRH power causes the electron density and temperature profiles to become more peaked, implying a strong correlation between the normalized logarithmic electron density gradient and the electron to ion temperature ratio. Hence, the similarity between figure 6.7 left and right.

To validate the understanding of the physical mechanisms responsible for the scalings seen in the database, theoretical simulations of the neoclassical and turbulent transport
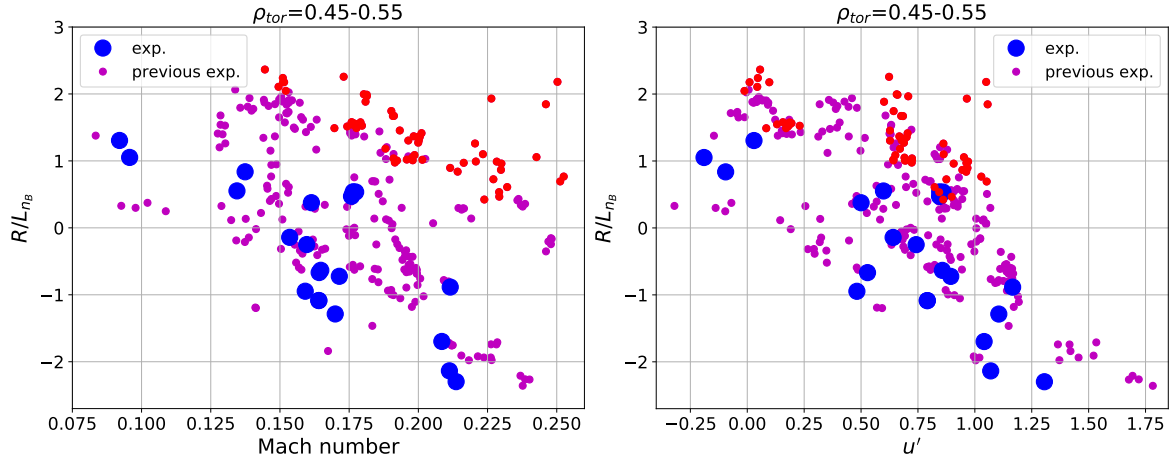
Figure 6.8.: Same as figure 6.7 but for the deuterium Mach number (left) and the toroidal rotation gradient u' (right).

have been performed and are compare to the experimental data in the next section.

6.3. Comparison to transport theory

6.3.1. Neoclassical transport

The neoclassical theory was briefly reviewed in section 4.3. As already discussed there, and also seen in chapter 5 where one experimental example was already compared to theory, the neoclassical transport is expected to be negligible for light impurities. Nonetheless, this should be confirmed for the complete database.

In this work, the neoclassical transport was modeled with the code NEO [74, 75] for all the experimental data points. These neoclassical calculations include rotational effects and boron-boron collisions. The experimental transport coefficients plotted as a function of the ones derived with NEO at $\rho_{tor} = 0.3$ and at $\rho_{tor} = 0.5$ are displayed in figure 6.9. The red dashed lines correspond to the one-to-one line. As expected, the neoclassical D, at both radial locations, are $10-100$ times smaller than the experimental ones. The drift velocity is not well reproduced by the neoclassical simulations either. At $\rho_{tor} = 0.3$ the neoclassical theory predicts peaked boron density profiles (negative v) for the whole database even though the majority of the experimental profiles are hollow (positive v). At $\rho_{tor} = 0.5$ NEO is able to predict hollow profiles in some of the cases where the experimental profiles are hollow, but not for all cases. All in all, the values of the neoclassicaly deduced v are too small compared to the experimental data. It comes to no surprise that the neoclassical theory cannot reproduce the experimental transport coefficients and we, therefore, move on to the turbulent contribution.

6.3.2. Turbulent transport

The turbulent transport, which was briefly discussed in section 4.4, was modeled with the gyrokinetic flux tube code GKW [76]. For the whole database, quasi-linear simulations at a turbulent wavenumber $k_\theta \rho_i = 0.4$ were performed. Non-linear simulations

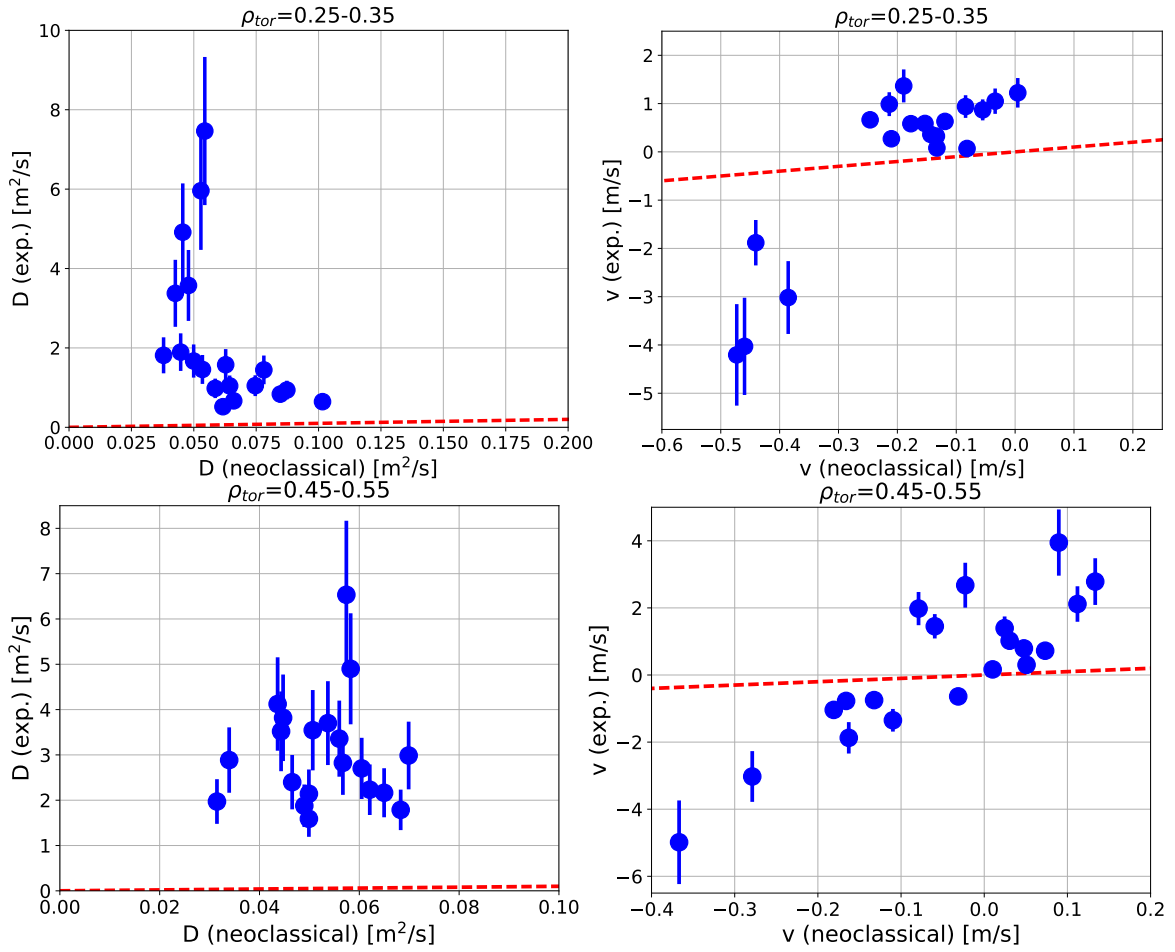Figure 6.9.: Experimental D (left) and v (right) plotted as a function of the neoclassical values at $\rho_{tor} = 0.3$ (top row) and at $\rho_{tor} = 0.5$ (bottom row). The red dashed line is the one-to-one line.

were carried out for one experimental data point (this was presented in chapter 5). As could be seen, the quasi-linear results were in good agreement with the non-linear results and, therefore, quasi-linear simulations for the rest of the database are considered to be sufficient. In these simulations, the plasma is modeled as pure plasma and the boron impurity in trace concentration. This is well met with the experimental data as the concentration of boron is $< 1\%$. The micro-instabilities are, hence, determined by the bulk plasma. Collisions, the experimental flux surface geometry, and centrifugal forces are included in the simulations. From these simulations, the turbulent diagonal part (the diffusion) and the off-diagonal parts (the thermo-diffusion, roto-diffusion, and pure convection) of the impurity particle flux are computed and are then compared to the experimentally deduced transport coefficients.

6.3.3. Turbulent transport terms

In equation (4.30), the expression for the turbulent normalized logarithmic boron density gradient was given. In this equation $C_T R/L_{T_i}$ is the thermo-diffusive term, $C_U u'$ the roto-diffusive term and C_P the pure convective term. These different components at mid-radius are plotted as a function of the frequency of the most unstable mode ω_r in figure 6.10. Negative values of ω_r correspond to a TEM dominant regime whereas positive values of this quantity correspond to an ITG dominated regime. As a can be seen in figure 6.10, almost all the discharges in the database are ITG dominated as ω_r covers a range from 0 to 0.7. The biggest contribution to the boron particle flux is the pure convective term C_P, which is negative for the whole database, that is, it always predicts an inward transport. Its absolute value increases the more one moves in the ITG direction, leading to more peaked profiles. The thermo-diffusion and roto-diffusion both take positive values in the ITG regime and also increase with increasing ω_r. This means that these two terms cause an outward transport, that is, a hollowing of the boron density profile. The absolute value of these quantities is, however, not large enough to fully balance the pure convection, which dominates, and the total predicted flux is directed inward for the majority of the database, meaning peaked boron density profiles as predicted.

6.3.4. Turbulent versus neoclassical contributions

The total theoretical D and v are a sum of both the neoclassical and the turbulent parts. For summing the turbulent and neoclassical transport components the scheme of Ref. [57] is adopted. The turbulent flux levels from the quasi-linear gyrokinetic simulations, which are highly sensitive to the input temperatures and density profiles and their corresponding experimental uncertainties, can vary up to an order of magnitude from the actual experimental turbulent flux and this can lead to an over- or underestimation of the actual transport coefficients if not taken properly into account. Therefore, a normalization with the ion heat conductivity χ_i has been introduced to assure that the turbulent flux levels are renormalized to the ones from the experiment. This scheme assumes that the impurity transport coefficient to the ion heat conductivity ratio is weakly dependent on the turbulent transport level. The two different contributions are, thus, summed under the assumption that the turbulent transport ion
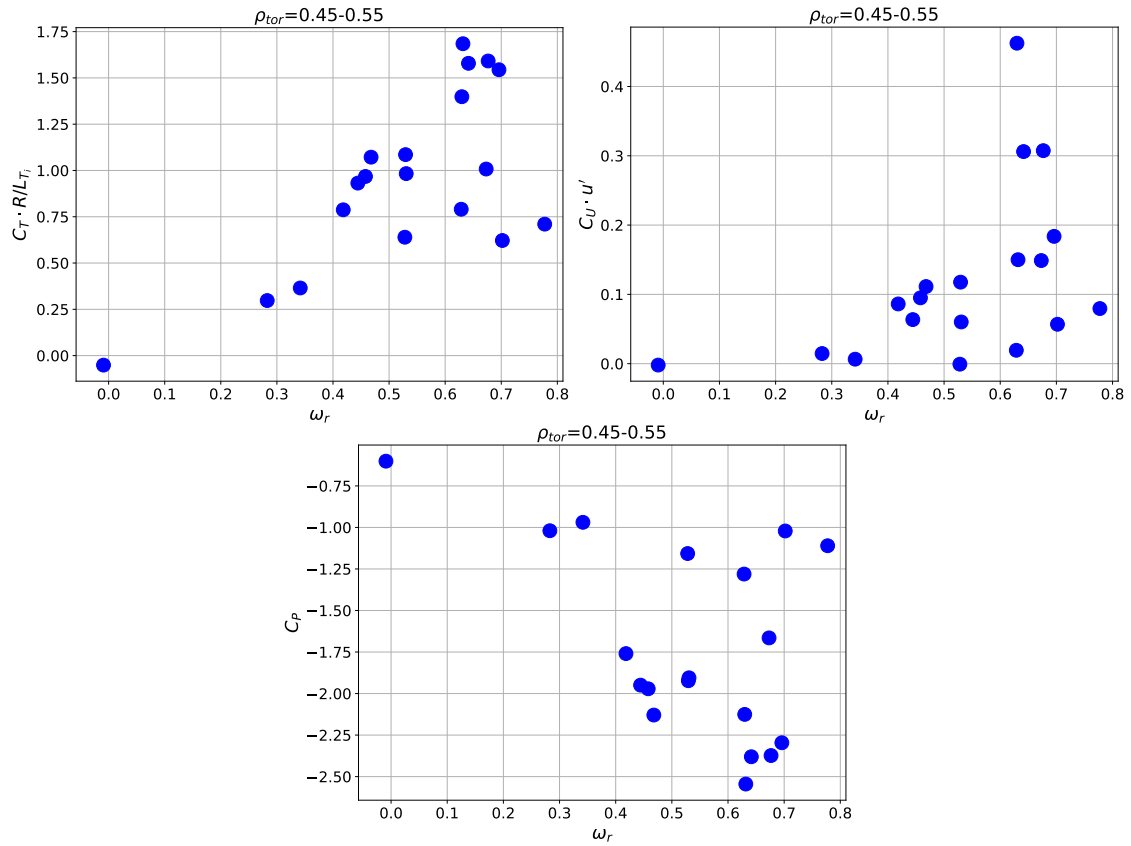
Figure 6.10.: Turbulent contributions to the boron particle transport at $\rho_{tor} = 0.5$ plotted versus the frequency of the most unstable mode ω_r: top left is the thermo-diffusion, top right is the roto-diffusion, and bottom middle is the pure convection. All terms are normalized to the diffusion coefficient D_n.

heat conductivity χ_i^{GKW}, which is calculated by GKW, matches the experimental ion heat conductivity, which is the anomalous part of the power balance ion heat conductivity computed with TRANSP [127] as $\chi_{i,an} = \chi_i^{PB} - \chi_i^{NC}$. For the boron transport coefficients this implies:

$$D_B^{GKW} = D_{n,B}^{GKW} \frac{\chi_{i,an}}{\chi_i^{GKW}}, \tag{6.1}$$

$$v_B^{GKW} = V_B^{GKW} \frac{\chi_{i,an}}{\chi_i^{GKW}}, \tag{6.2}$$

$$D_B^{theory} = D_B^{GKW} + D_B^{NC}, \tag{6.3}$$

$$v_B^{theory} = v_B^{GKW} + v_B^{NC}, \tag{6.4}$$

and the normalized logarithmic boron density gradient:

$$\frac{R}{L_{n_B}} = -\frac{RV_B^{GKW}/\chi_i^{GKW} + RV_B^{NC}/\chi_{i,an}}{D_{n,B}^{GKW}/\chi_i^{GKW} + D_B^{NC}/\chi_{i,an}}. \tag{6.5}$$

We already saw in section 6.3.1 that the neoclassical transport coefficients cannot reproduce the experimental ones. This gives us a hint that turbulence is the main player for driving the transport. That this actually is the case is visualized in figure 6.11, where the total theoretical D (left hand side) and v (right hand side) are compared to the one computed by GKW for two radial locations. The red dashed line is, again, the one-to-one line. For both radial locations, the total theoretical diffusion is almost entirely represented by the turbulent part. As for the drift velocity, there is a very small deviation from the red line meaning that the neoclassical drift has a minor influence on the total v. However, the importance of the neoclassical contribution to the transport is indeed negligible and it can be concluded that the transport is turbulence driven for the whole database in the radial domain which has been studied.

6.3.5. Comparison between modeling and experiment

In this section the experimentally deduced transport coefficients are compared with the ones predicted by theory. For the sake of correctness, the theoretical transport coefficients and the normalized logarithmic boron density gradients contain both the neoclassical and turbulent contributions, even though, the neoclassical part is negligible in the core region of the plasma. The summation has been done according to equations (6.3), (6.4), and (6.5). In figure 6.12 the experimental diffusion coefficient is plotted as a function of the theoretical one at $\rho_{tor} = 0.3$ (left) and $\rho_{tor} = 0.5$ (right). As can be seen, the turbulent theory is able to reproduce the experimental behavior very well except for two points (encircled) with high diffusion at $\rho_{tor} = 0.5$. The good agreement in D for the majority of the database falls in line with what we saw in chapter 5 for one experimental data point. The experimental drift velocity is plotted as a function of the theoretical one at $\rho_{tor} = 0.3$ (left) and $\rho_{tor} = 0.5$ (right) in figure 6.13. At this point we start to see a discrepancy between theory and experiment. At both radial locations, the majority of the data points lie above the one-to-one line, which means that the theoretical v is more negative than the experimental v. Theory, thus,
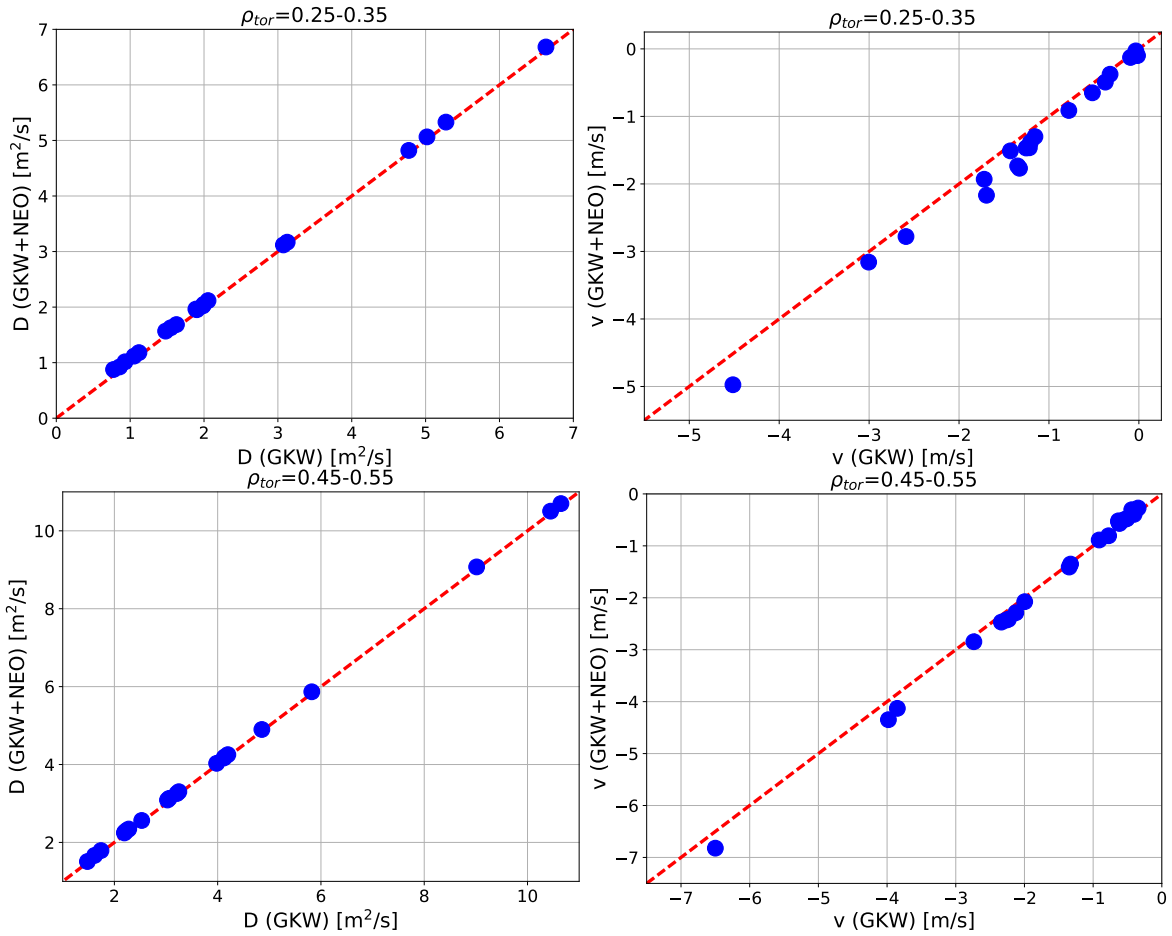
Figure 6.11.: The total theoretical transport coefficient D_B^{theory} (left) and v_B^{theory} (right) plotted as a function of the values from GKW at $\rho_{tor} = 0.3$ (top row) and at $\rho_{tor} = 0.5$ (bottom row). The red dashed line is the one-to-one line.
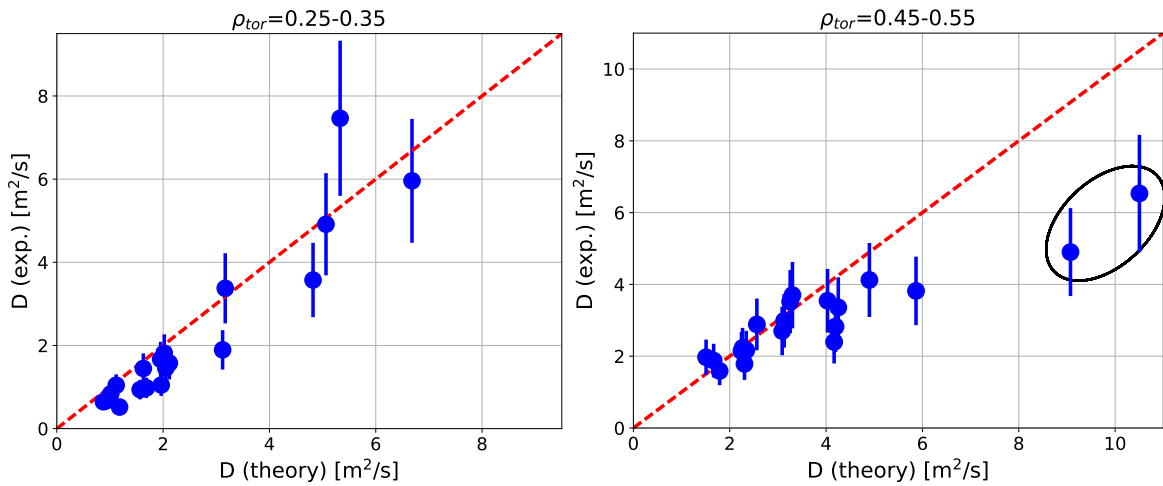

Figure 6.12.: Experimental and theoretical diffusion coefficient at $\rho_{tor} = 0.3$ (left) and $\rho_{tor} = 0.5$ (right). The red lines represent perfect agreement.
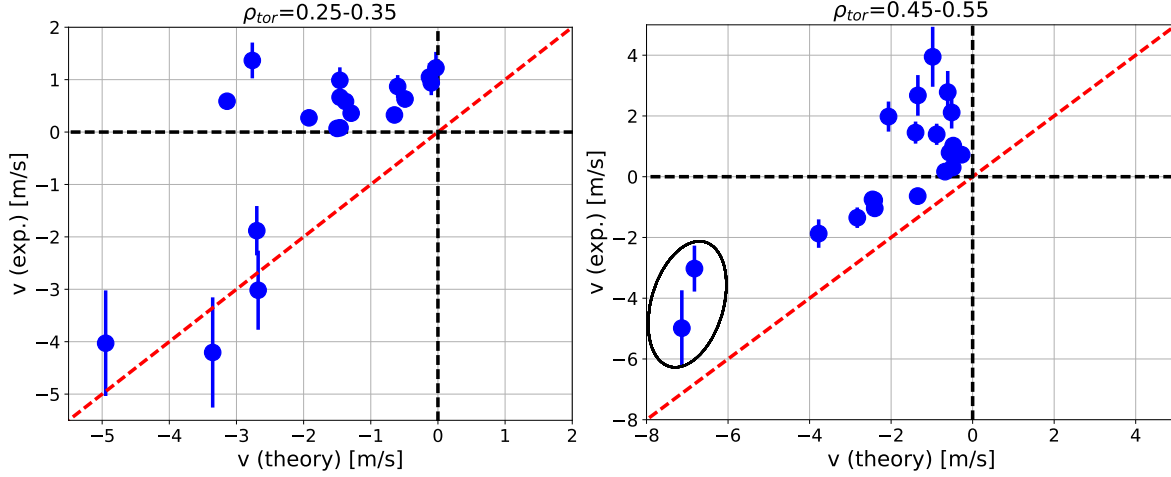
Figure 6.13.: Experimental and theoretical drift velocities at $\rho_{tor} = 0.3$ (left) and $\rho_{tor} = 0.5$ (right). The red lines represent perfect agreement.

predicts a stronger inward drift or more peaked boron profiles than what is actually experimentally measured. It seems that theory is in better agreement with the peaked experimental data (negative v). Thus, the more hollow the experimental profiles are (higher positive value of v), the larger the discrepancy becomes. This behavior was also seen for the example data shown in chapter 5. That this is the case, becomes more obvious when studying figure 6.14, where the difference between the experimental and theoretical drift velocity is plotted versus the experimental drift velocity at $\rho_{tor} = 0.5$. It should be noted that the two data points with very large negative drift velocity which are encircled in the plot on the right hand side of figure 6.13 are not present in figure 6.14. Furthermore, these two cases correspond to the encircled points with the very high diffusion on the right hand side figure 6.12. A more detailed discussion about these two cases is given below.

This disagreement in v is then directly translated to the disagreement seen for the normalized logarithmic boron density gradient in figure 6.15. The left hand side of figure 6.15 shows the comparison between experiment and theory at a radial location of $\rho_{tor} = 0.3$ and the right hand side at $\rho_{tor} = 0.5$. At $\rho_{tor} = 0.5$, the database of the steady-state boron transport study of Ref. [45] has been included in purple. Just as for the drift velocity, at both locations for the majority of the database, there is a large deviation from the one-to-one line and the theoretically calculated R/L_{n_B} predicts more peaked boron density profiles (positive values of R/L_{n_B}) than what is measured in the experiment (negative values of R/L_{n_B}). It is important to note that R/L_{n_B} can only give information about the ratio v/D and just because there is a good agreement between experiment and theory for this quantity, does not mean that the predictions of both D and v are correct. For example, the two points with the largest values of R/L_{n_B} on the right hand side of figure 6.15 are both close to the one-to-one line and, thus, it seems like we have a good agreement between experiment and theory for these two cases. However, for these two points, D is over predicted and the absolute value of the theoretical v is larger than the experimental v, leading to a "false" good agreement in R/L_{n_B}. Hence, the importance of transient transport studies, which can disentangle D
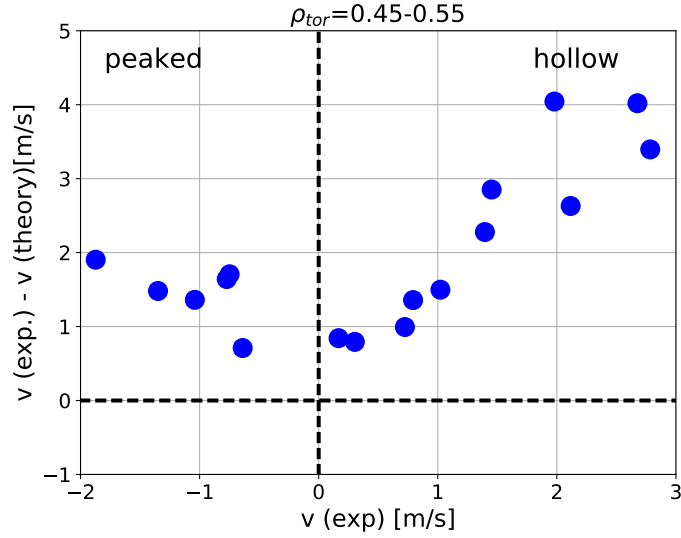
Figure 6.14.: The difference between the experimental and theoretical drift velocity plotted versus the experimental drift velocity at $\rho_{tor} = 0.5$.

and v from each other. As already pointed out in section 6.2, at $\rho_{tor} = 0.5$ the previous study was able to measure a bit more peaked boron density profiles than the present study, but otherwise the same parameter space in R/L_{n_B} is covered. More importantly, both the old and new study show the same discrepancy between theory and experiment.
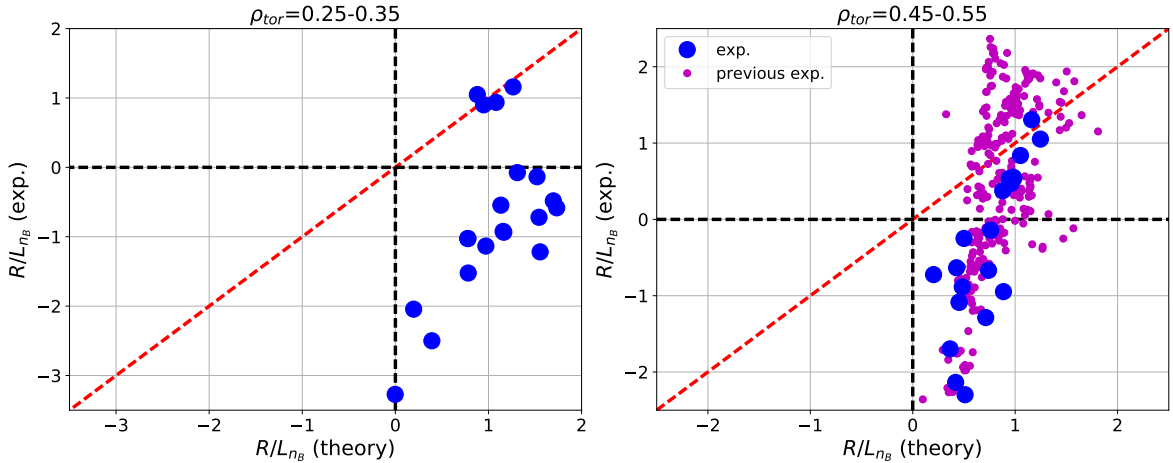
Figure 6.15.: Experimental and theoretical normalized logarithmic boron density gradient at $\rho_{tor} = 0.3$ (left) and $\rho_{tor} = 0.5$ (right). The red line represent perfect agreement. In the plot on the right, the purple points represent the database of the boron steady-state transport study in Ref. [45].
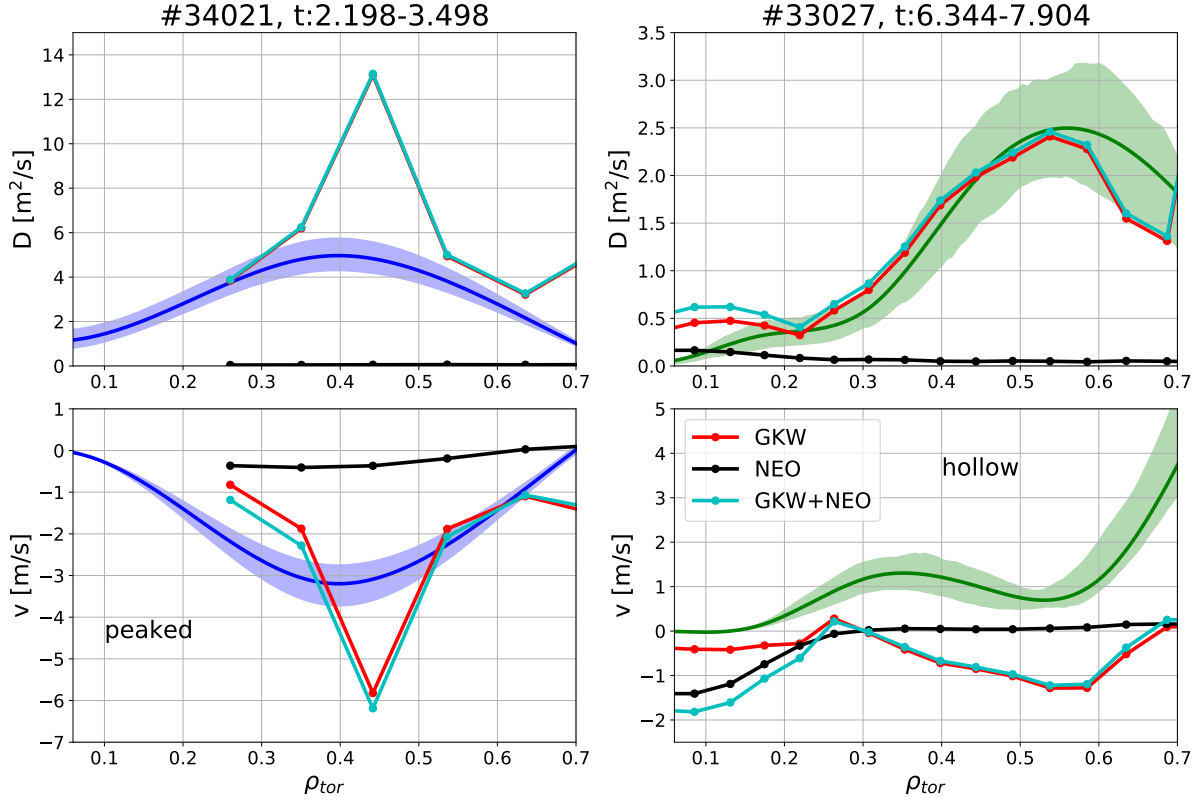
Figure 6.16.: D (top) and v (bottom) profiles of the data shown in figure 6.3, where the left profiles in blue correspond to a peaked boron density profile and the right profiles in green correspond to a hollow boron density profiles (see figure 6.2). Here the theoretical predictions from NEO in black, GKW in red, and the sum of both in light blue have been included.

At this point, it could also be of interest to show how good the agreement is between the experimental profile data shown in figures 6.2 and 6.3 and the theoretical profiles. In figure 6.16, the profiles of the neoclassical transport coefficients (black), the turbulent ones from GKW (red), and the sum of both (light blue) are shown along with the profiles of the experimental transport coefficients. The blue profiles on the left hand side belong to the peaked boron density profile (negative v) of of figure 6.2 left and the green profiles on the right hand side correspond to the hollow boron density profile (positive v) of figure 6.2 right. The agreement in D between theory and experiment for the hollow profile (green) is very good, but not as good for the peaked profile (blue), which will be discussed in more detail below. As we saw before when looking at the whole database, in the case of the hollow profile, the theoretical v is negative, and hence predicting a peaked profile, whereas the experimental v is positive. For the peaked profile the theoretical v is, at mid-radius, even more negative than the experimental one. This confirms the general trend seen for the whole database in figure 6.13, namely that the theoretical v is always more negative than the experimental one. As can be seen on the left hand side of figure 6.16, the agreement in D between GKW and experiment for the peaked profile is good except at one radial location ($\rho_{tor} = 0.45$). To further investigate the reason for this, a sensitivity study of GKW was performed. The value of R/L_{n_e}, R/L_{T_e}, T_e/T_i, and R/L_{T_i} at this radial location were varied within the experimental error bars. New GKW simulations were then performed to inspect
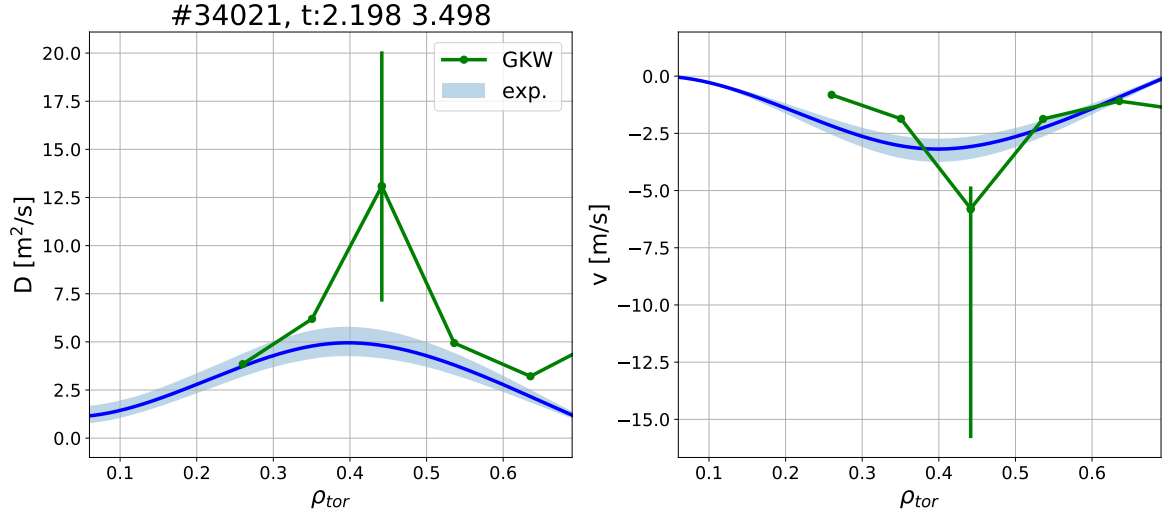
Figure 6.17.: Result of the GKW sensitivity study at $\rho_{tor} = 0.45$, where the input value of R/L_{T_i} was varied within the experimental error bars.

how such variations of the input parameters affect the resulting transport coefficients. The variations in R/L_{n_e}, R/L_{T_e}, and T_e/T_i rendered little variations in D and v. R/L_{T_i}, however, caused a quite large fluctuation of the transport coefficients, which can be seen in figure 6.17 where the resulting variation in D and v created by the change in R/L_{T_i} is symbolized with the green error bar at $\rho_{tor} = 0.45$. The reason for this behavior is that at this location the value of the real frequency ω_r obtains a value close to zero, meaning that we are close to the ITG-TEM transition. When changing the drive of the turbulence (R/L_{n_e}, R/L_{T_e}, T_e/T_i, and R/L_{T_i}) in such conditions, the transport coefficients can change drastically [128].

The two encircled data points at $\rho_{tor} = 0.5$ with a large diffusivity on the right hand side of figure 6.12, where there is a larger discrepancy between theory and experiment compared to the bulk of the database, are such cases where ω_r is close to zero and GKW is, thus, very sensitive to small variations in the input parameters. As already pointed out above, for the drift velocity these two cases correspond to the points which attain large negative values. By then making the comparison at a radial location further out, the agreement between theory and experiment is improved for both D and v. This can be seen in figure 6.18, where the encircled blue open points have been shifted to the orange open diamonds.

Next, we compare the experimental D, v, and R/L_{n_B} (blue filled points) with the theoretical ones (open red points) as a function of different plasma parameters, namely R/L_{n_e} (first row of figure 6.19), T_e/T_i (second row of figure 6.19), R/L_{T_i} (third row of figure 6.19), u' (fourth row of figure 6.19), and the deuterium Mach number (fifth row of figure 6.19) at $\rho_{tor} = 0.5$. In these plots we, again, see that the theoretical and experimental diffusion agree well with one another and that there is a discrepancy in the drift velocity mainly for positive v (negative R/L_{n_B}), that is, hollow boron profiles. The trends of the transport coefficients with the different plasma parameters seen for the experimental data are also present in the theoretical predictions, however, the trends are not as strong. The theoretical predictions of v saturates at high values of
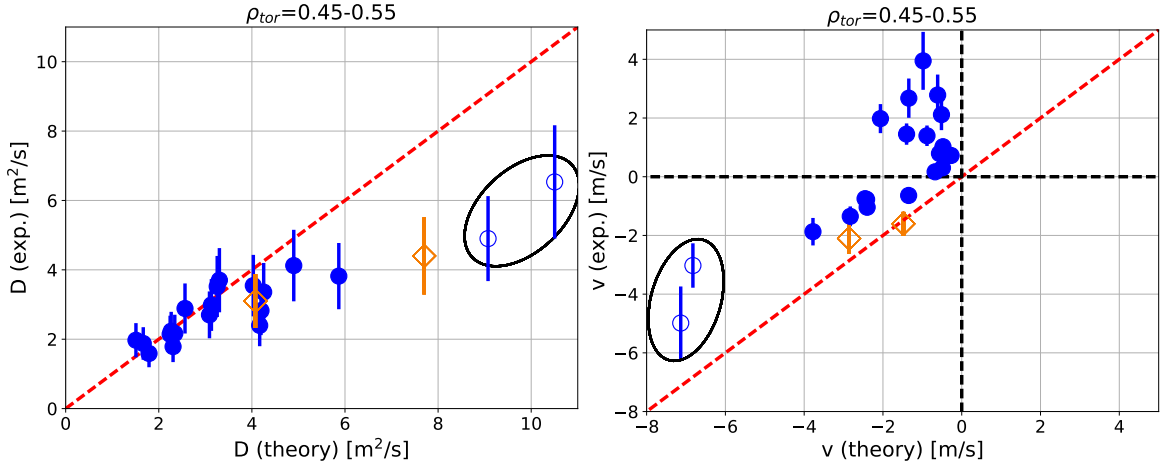
Figure 6.18.: Experimental and theoretical diffusion coefficient (left) and drift velocity (right). When the comparison of the two data points, where GKW is very sensitive to the input value of R/L_{T_i}, is made at a radial location further out the open blue circles are shifted to the open orange diamonds.

R/L_{T_i}, u' and Mach number, and low values of R/L_{n_e} and T_e/T_i. These are indeed cases with the most hollow boron density profiles. In the plot to the right in the first row of figure 6.19 it can also be seen that the experimentally measured boron profiles are always less peaked than the electron density profiles as the blue points lie bellow the one-to-one line. The same holds true for the theoretically predicted boron profiles, but here we, again, see that theory fails to reproduce the most hollow boron profiles, hence, there is a larger gap between the blue and red points for positive v and negative R/L_{n_B}. The same behavior can be seen in the other plots of figure 6.19, that is, experimental profiles are more hollow at low T_e/T_i, high R/L_{T_i}, high u', and high Mach number than the theoretical simulations.

When looking at the different off-diagonal components that make up the turbulent convection in figure 6.10, it can be seen that the outward terms (thermo-diffusion and roto-diffusion) are always balanced by the inward term (pure pinch). That is, when the outward components obtain higher positive values with increasing ω_r, the inward component obtains a higher negative value. To, thus, achieve a better agreement between theory and experiment, the outward component must be higher for all values of ω_r.

The same trends observed in the plots at $\rho_{tor} = 0.5$ are also seen at $\rho_{tor} = 0.3$. As already mentioned in section 6.1 the datasets displayed in figure 6.19 are not independent. Since there is a correlation between the plasma parameters (low R/L_{n_e}, high R/L_{T_i}, high u', and high Mach number occur together), it is difficult to explain the behavior of the transport coefficients with one single mechanism.
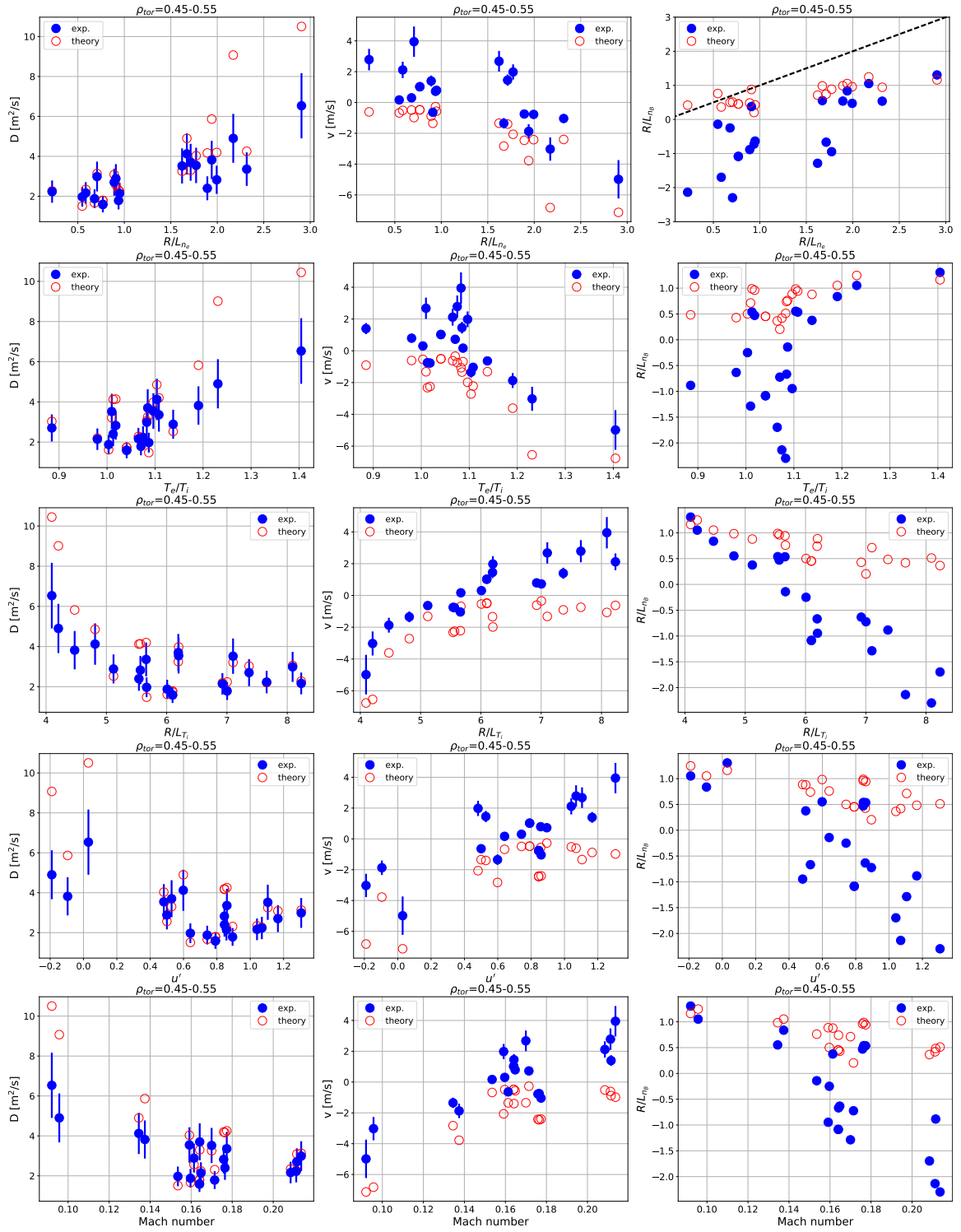
Figure 6.19.: Experimental (blue filled points) and theoretical (open red points) D (left), v (middle), and R/L_{n_B} (right) as a function of R/L_{n_e} (first row), T_e/T_i (second row), R/L_{T_i} (third row), u' (fourth row), and the deuterium Mach number (fifth row) at $\rho_{tor} = 0.5$.

6.3.6. Advanced theoretical models for the convective transport

In chapter 4, it was already mentioned that several low-Z impurity transport studies at other machines also have reported a discrepancy between theory and experiment for mainly the hollow impurity density profiles seen in this study and the one of Ref. [45]. These previous studies were steady-state analysis which did not provide separate information on D and v meaning it was not clear if both D and v were incorrect. However, with the new database of the individual transport coefficients presented in this work, we are able to further pinpoint the source of the disagreement, namely the drift velocity v. Theoretical work is ongoing on finding the missing puzzle piece of the outward drift in the convection so that the hollow impurity density profiles can be correctly reproduced. Including, for example, fast ions in the gyrokinetic simulations seem to be able to cure this problem but only to some small extent [129]. This additional effect only plays a role in discharges with high fast ion pressure, that is, discharges with a very high fraction of NBI heating power to the total heating power. In the case of boron, the inclusion of fast ions in the simulations results in a better agreement with the experimental normalized logarithmic boron density gradient, whereas for helium the effect is the opposite: worse agreement [129]. This effect was also tested on the database of this thesis. An additional quasi-linear gyrokinetic simulation including fast ions for one experimental data point with the highest fast ion pressure was performed. This case had $10\,\mathrm{MW}$ of NBI plus $0.5\,\mathrm{MW}$ of ECRH. The effect the inclusion of fast ions in the gyrokinetic simulation had on v at mid-radius for this particular case can be seen in figure 6.20. Here, the solid green circle is the original simulation without fast ions. When including the fast ions, the solid green circle is shifted to the open green circle. As can be seen, v obtains a less negative value (going from $-1.2\,\mathrm{m/s}$ to $-0.8\,\mathrm{m/s}$ at $\rho_{tor} = 0.5$) when including the fast ions in the simulation, but it is still far off from the experimental value ($4\,\mathrm{m/s}$). We can conclude that as the observation in Ref. [129], including fast ions will result in a less peaked boron density profile, but it cannot by far reproduced the very hollow experimental profile and can, thus, not completely cure the problem.

Additional solutions have been sought by including a cross-talk between the neo-classical and turbulent transport channels [130, 131]. In Ref. [131] the impact of the neoclassical distribution function on the turbulent impurity transport was investigated by means of coupling the codes NEO and GKW as well as fluid calculations. It was found that the inclusion of the neoclassical background caused an increase in the roto-diffusion term and, thus, a reduced inward convection. This effect increases with increasing collisionality, R/L_{T_i}, R/L_{n_e}, impurity mass, and safety factor. It is expected to have the largest impact on modest to heavy impurities at the edge of the plasma. Whether this effect can cause a better agreement between theory and experiment of the present study has not yet been investigated.

6.4. Multiple linear regression analysis

In the previous sections, we saw trends between the transport coefficients and different plasma parameters. Multiple linear regression analyses were performed with the aim to
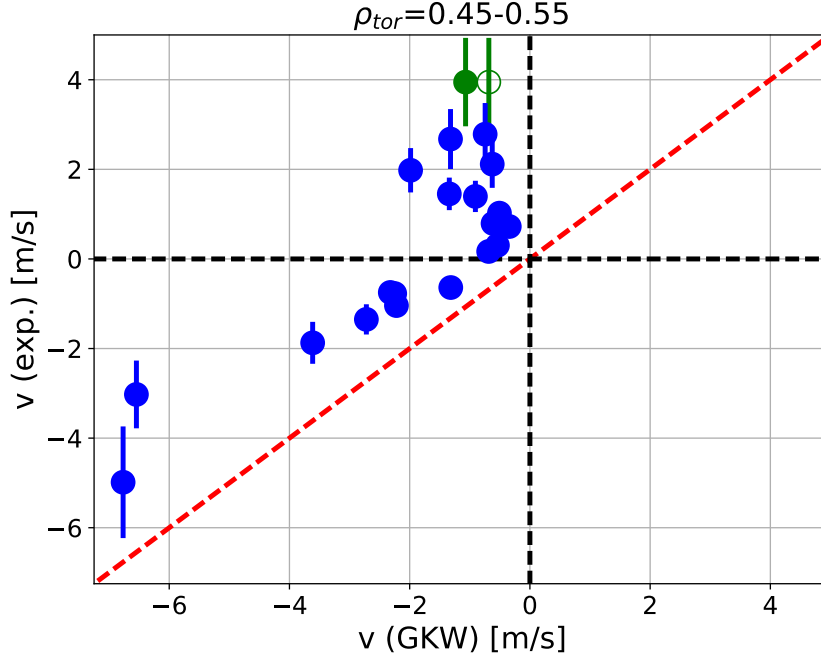
Figure 6.20.: The result of including fast ions in the gyrokinetic simulation of one experimental observation with the highest fast ion pressure. The turbulent drift velocity is less negative (shift of the green closed circle to the green open circle), however, it is still far away from reproducing the experimental drift velocity.

identify the relative importance of the plasma parameters on D and v. The regression method of our choice was ordinary least square. Since the database is relatively small, the regressions were limited to include only two regressors (the independent variables)[2]. In these regressions, different combinations of R/L_{T_i}, u', R/L_{n_e}, T_e/T_i, ν_{eff}, R/L_{T_e}, and deuterium Mach number were attempted. To determine if a variable was statistically significant or not the t-statistic and the p-value were examined with the criteria that $|t| \geq 2$ and $p \leq 0.05$. The t-statistic is defined as the regression coefficient divided by its standard deviation and it gives a measure of the significance of the regressor. A $p \leq 0.05$ means that the probability to incorrectly reject the null hypothesis is 5%. It was found that the two plasma parameters with t-statistic greater than 2 and p-value below 0.05 which yielded the best regressions for the experimental diffusion coefficient were R/L_{n_e} and T_e/T_i. For the experimental drift velocity, on the other hand, the regressors with the lowest p-value were R/L_{n_e} and u'. These regressions that best reproduced the experimental D and v at $\rho_{tor} = 0.5$ were:

$$D_{exp} = -3.81 \pm 1.51 + (5.30 \pm 1.52)\frac{T_e}{T_i} + (0.81 \pm 0.22)\frac{R}{L_{n_e}}, \qquad (6.6)$$

$$v_{exp} = -0.35 \pm 1.15 + (2.95 \pm 0.85)u' - (1.06 \pm 0.48)\frac{R}{L_{n_e}}. \qquad (6.7)$$

Judging from the t-statistic and the p-values, which are listed in table 6.3, R/L_{n_e} is the most statistically significant regressor for D_{exp}, whereas for v_{exp}, u' has a slightly

---

[2]The standard rule of thumb in statistics: one regressor per 10 data points.

	t-statistic		p-value		adjusted R^2	RMSE
	T_e/T_i	R/L_{n_e}	T_e/T_i	R/L_{n_e}		
D_{exp}	3.480	3.654	0.003	0.002	0.746	0.539
D_{theory}	3.867	4.735	0.001	1.916e-4	0.812	1.453
	u'	R/L_{n_e}	u'	R/L_{n_e}		
v_{exp}	3.464	-2.201	0.030	0.042	0.669	1.122
v_{theory}	3.460	-4.130	0.003	0.001	0.786	2.514

Table 6.3.: t-statistic, p-value, adjusted R^2, and RMSE of the most successful regressions.
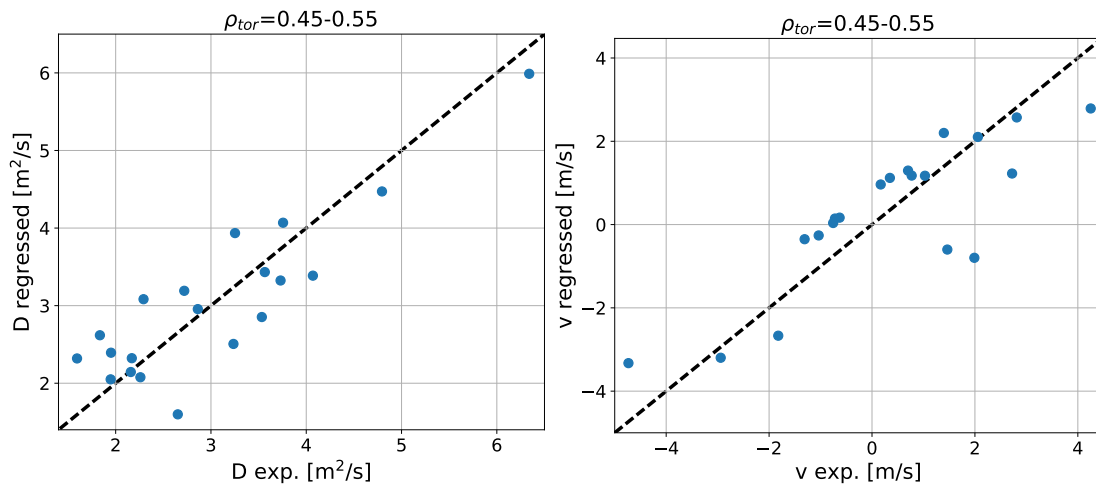
Figure 6.21.: The regression of the experimental D (left) and v (right) at $\rho_{tor} = 0.5$.

higher significance than R/L_{n_e}. The outcome of the regressions are shown in figure 6.21. The adjusted R^2 and root mean squared error (RMSE) of the regressions can also be found in table 6.3. To only look at the RMSE is dangerous, since it is very sensitive to outliers and if one or several are present, the RMSE will increase. This is not the case for the adjusted R^2 and this is the reason why both were taken into consideration. The adjusted R^2 was used instead of the normal R^2, since the first one penalizes the addition of regressors that are not significant to the regression whereas the latter always increases with increasing number of regressors. The adjusted R^2 takes values between 0 and 1, and the higher, the better is the regression. This is in contrast to the RMSE, which should be as low as possible.

As a comparison, the four next best regressions of D_{exp} and v_{exp} are listed in table 6.4 and 6.5, respectively. The first column of the t-statistic and p-value correspond to the first regressor and the second column to the second regressor. Even though the p-value of one of the regressors were very low and even below 0.05, the other was not and these regressions were rejected. For example, judging from the third row of figure 6.19, it seems that R/L_{T_i} can explain the trend seen in the experimental drift velocity very well and this is indeed confirmed by examining the p-values of R/L_{T_i}. The accompanying regressor in these regression do, however, have a very large p-value

D_{exp}					adjusted R^2	RMSE
	t-statistic		**p-value**			
R/L_{n_e}, Mach	3.189	-1.541	0.005	0.142	0.658	0.660
R/L_{n_e}, u'	3.523	-1.445	0.003	0.167	0.612	0.665
T_e/T_i, Mach	2.748	-1.119	0.014	0.279	0.578	0.695
T_e/T_i, R/L_{T_i}	3.486	-0.815	0.003	0.426	0.563	0.706

Table 6.4.: t-statistic, p-value, adjusted R^2, and RMSE of the poorer regressions of D_{exp}.

v_{exp}					adjusted R^2	RMSE
	t-statistic		**p-value**			
R/L_{n_e}, T_e/T_i	-2.017	-2.635	0.060	0.017	0.544	1.316
R/L_{n_e}, Mach	-1.743	3.830	0.099	0.001	0.697	1.073
T_e/T_i, R/L_{T_i}	-1.172	6.476	0.257	0.000	0.815	0.839
R/L_{n_e}, R/L_{T_i}	-0.981	5.804	0.341	0.000	0.811	0.848

Table 6.5.: t-statistic, p-value, adjusted R^2, and RMSE of the poorer regressions of v_{exp}.

and these regressions are, therefore, dismissed.

Using the regressors of the experimental transport coefficients for the theoretically predicted transport coefficients at $\rho_{tor} = 0.5$ resulted in the following regressions:

$$D_{theory} = -9.78 \pm 2.63 + (10.25 \pm 2.65)\frac{T_e}{T_i} + (1.84 \pm 0.39)\frac{R}{L_{n_e}} \qquad (6.8)$$

$$v_{theory} = -1.51 \pm 0.86 + (2.20 \pm 0.64)u' - (1.48 \pm 0.36)\frac{R}{L_{n_e}}. \qquad (6.9)$$

For the predicted diffusion coefficient, R/L_{n_e} was also the most significant regressor (the t-statistic, the p-values, adjusted R^2, and RMSE of these regressions can also be found in table 6.3). The coefficients in front of R/L_{n_e} and T_e/T_i do not cover the same range in the experimental and predicted regressions. For the predicted drift velocity, however, R/L_{n_e} had a slightly higher statistical significance than u' (the opposite was observed for the experimental drift velocity). Here, the ranges of the coefficients in front of u' and R/L_{n_e}, do partially overlap in the experimental and predicted regressions. In figure 6.22 the regressions of D_{theory} and v_{theory} can be seen. Compared to the regressions of the experimental transport coefficients, the RMSE are notably higher due to outlying data points. The regressions are, however, better than for the experimental D and v, which can be seen on the considerably lower p-values as well as the higher adjusted R^2 values.

The linear regressions imply that R/L_{n_e} and T_e/T_i are the two plasma parameters that best explain the trends seen in the database for the diffusion coefficient and R/L_{n_e} and u' for the drift velocity. When performing regressions with four or up to six regressors, all the regressors except one had very large p-values and were, thus, insignificant. To
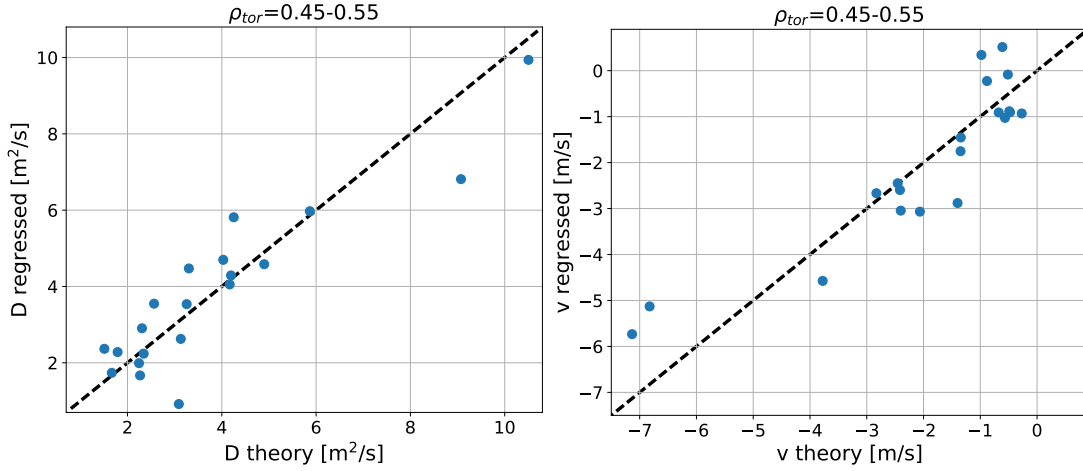
Figure 6.22.: The regression of the predicted D (left) and v (right) at $\rho_{tor} = 0.5$.

draw any certain conclusions from such exercises, the database must be significantly increased.

6.5. Projections for a future fusion reactor

In a future fusion reactor, helium will be produced in the fusion reaction between the deuterium and the tritium ions and there will, hence, exist a helium source in the center of the plasma. In chapter 1 we already discussed the danger of fuel dilution and that a too high concentration of impurities has a negative effect on the fusion performance. The produced helium, therefore, needs to be transported outward in order to avoid helium accumulation in the plasma center. To achieve that, the helium density profile should preferably be hollow, meaning a drift directed outwards, and strong enough to compensate the source effect. If the helium profile is flat or the drift velocity is only weakly directed outwards, then additionally, the diffusion coefficient of helium should be large enough compared to the ion heat conductivity χ_i. The ratio D/χ_i is a relative measure of the strength of the helium particle transport with respect to the heat transport of the plasma. The impurities should preferably be transported outward to a higher extent than the heat of the plasma and we, thus, want this ratio to be as high as possible. In Ref. [50] it is foreseen that central helium accumulation can be avoided if the diffusivity of helium to ion heat conductivity ratio is bigger than 0.3. Experimental findings suggest that helium transport does not seem to behave exactly as boron transport [45], but nevertheless as a first proxy we can study D/χ_i for boron. In figure 6.23, experimental (blue filled points) and turbulent (open red points) D/χ_i are plotted as a function of the real mode frequency ω_r (left), the electron to ion temperature ratio T_e/T_i (middle), and the electron heat flux to total heat flux ratio Q_e/Q_{tot} (right) at a central plasma position (top) and at mid-radius (bottom). The experimental diffusion coefficient has been divided by the anomalous part of the power balance ion heat conductivity from TRANSP $\chi_{i,an}$. The turbulent diffusion and ion heat conductivity are both calculated with GKW. We can see in the middle plots that we have a clear scaling of D/χ_i with increasing T_e/T_i in both the experimental
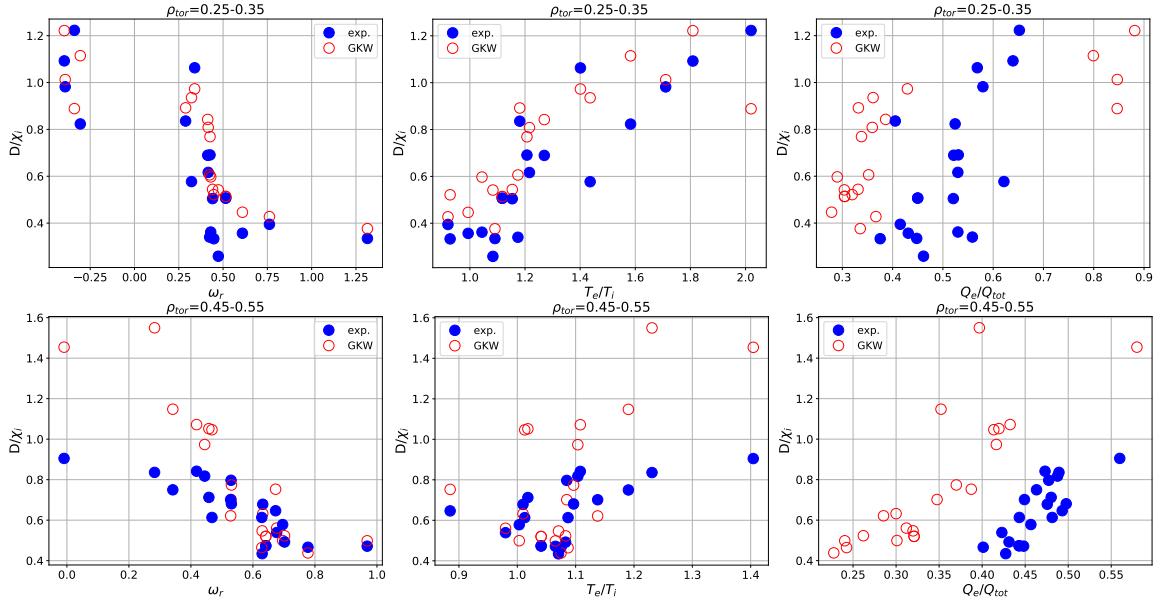
Figure 6.23.: Experimental (blue filled points) and turbulent (open red points) D/χ_i plotted as a function of the frequency of the most unstable mode ω_r, the electron to ion temperature ratio T_e/T_i, and the electron heat flux to total heat flux ratio Q_e/Q_{tot} at a central position of the plasma ($\rho_{tor} = 0.3$) and at mid-radius ($\rho_{tor} = 0.5$).

measurements and turbulent calculations. ITER is foreseen to operate at T_e/T_i values close to unity [50]. Around this value of T_e/T_i, the D/χ_i values for boron are slightly higher than 0.3, which is promising for a future fusion reactor.

The result presented in figure 6.23 is also interesting from another point of view when it comes to validating the turbulent transport theory. In many present devices, and also envisaged for future fusion devices, the plasma facing components are made up of a heavy elements, for example, tungsten in AUG. The reason being simply that heavier elements like tungsten can withstand high heat loads and has a lower tritium retention than lighter elements. The side-effect of utilizing high-Z elements as a wall material is that these elements will be sputtered or eroded during operation and, thus, introduced as impurities in the plasma and we already saw in chapter 1, figure 1.5 that the higher the mass of the impurity, the smaller the operational window becomes. To achieve a burning plasma the concentration of, for example, tungsten must be substantially lower than that of helium or carbon. Therefore, means of controlling the impurity accumulation of also the high-Z impurities are a must. In present day devices the transport of heavy impurities is dominated by neoclassical transport [81]. This neo-classical transport produces an inward convection which increases with impurity charge and can cause a central accumulation of especially heavy impurities if a counteracting mechanism is not present. It has been observed that such an accumulation of high-Z impurities can be avoided by applying central heating to the electron channel in a dominated NBI heated plasma [22, 53]. It is believed that the turbulent diffusion is the mechanism responsible for offsetting the inward neoclassical drift velocity and, thus, preventing central accumulation [53]. This mechanism may well play a critical role of

avoiding high-Z impurity accumulation in future device, especially since the turbulent transport of the heavier impurities is expected to play a more important role in these devices.

To better understand how the turbulent diffusion of high-Z impurities depends on the electron to ion heating ratio, we report here on a purely theoretical gyrokinetic study [128]. In this study, non-linear gyrokinetic simulations with the code GKW of the impurity tungsten was performed. In these simulations the turbulent tungsten diffusion in the central region of the plasma was investigated when varying the ion and electron heat fluxes while keeping the total heat flux constant. It was found that the ratio of the tungsten diffusivity to the ion heat conductivity was a non-monotonic function of the electron to ion heat flux ratio Q_e/Q_i. It reached a maximum at comparable levels of electron and ions heat fluxes and the electron heat flux slightly exceeded the ion heat flux (see left hand side of figure 6.24). These results suggest that in a dominantly ion heated plasma, the addition of the electron heating has a more favorable effect than the addition of ion heating. On the other hand, in a dominantly electron heated plasma, adding heating to the ion channel is more favorable than adding heating to the electron channel. Linear simulations showed a good agreement with the non-linear ones (see right hand side of figure 6.24), which suggests that the reason for this behavior could be explained with linear physics. On the right hand side of figure 6.24 the tungsten diffusion to heat conductivity ratios is plotted as a function of the real frequency of the most unstable mode ω_r and also here the non-monotonic behavior can be seen. Negative values of ω_r correspond to TEM being the most unstable mode and positive values of ω_r to ITG. A quasi-linear analytical model showed that this effect is a consequence of the energy dependence of the curvature and ∇B drift [128]. There is a shift in the real mode frequency ω_r between the maximum diffusivity and the maximum heat conductivity. If the ∇B drift was independent of particle energy, the diffusivity to heat conductivity ratio would be constant and would not change with ω_r. Since the ∇B drift depends on the particle charge, the effect is stronger the higher the charge of the impurity.

If this effect is indeed real, it could be a vital piece of information to avoid high-Z impurity accumulation in future fusion devices, but so far no experimental studies on tungsten transport have been conducted to confirm these theoretical findings. As a first step of validation, it is interesting to examine how D/χ_i for boron in the present database behaves as a function of ω_r, T_e/T_i, and Q_e/Q_{tot}, which was shown in figure 6.23 for two radial regions in the plasma. The experimental D/χ_i is shown with blue filled symbols and the ones from the gyrokinetic simulations in open red symbols. In the experiments of this study we never achieved TEM dominated plasmas and in the the whole database the turbulence is ITG driven as can be seen on the left top and bottom plots of figure 6.23. By comparing these plots with the right hand side plot of figure 6.24, we see that the same trend can be seen for positive ω_r, that is, decreasing D/χ_i with increasing ω_r. By then comparing the middle and right plots of figure 6.23 with the left plot of figure 6.24 we see the same rising trend when the plasma is dominantly ion heated. The offset seen between the red and blue symbols in the left plots of figure 6.24 is due to the mis-match in the experimental and simulated heat fluxes. The ion and electron heat flux of the gyrokinetic simulations were never matched to the experimental ones from TRANSP in the present study except for the one non-linear
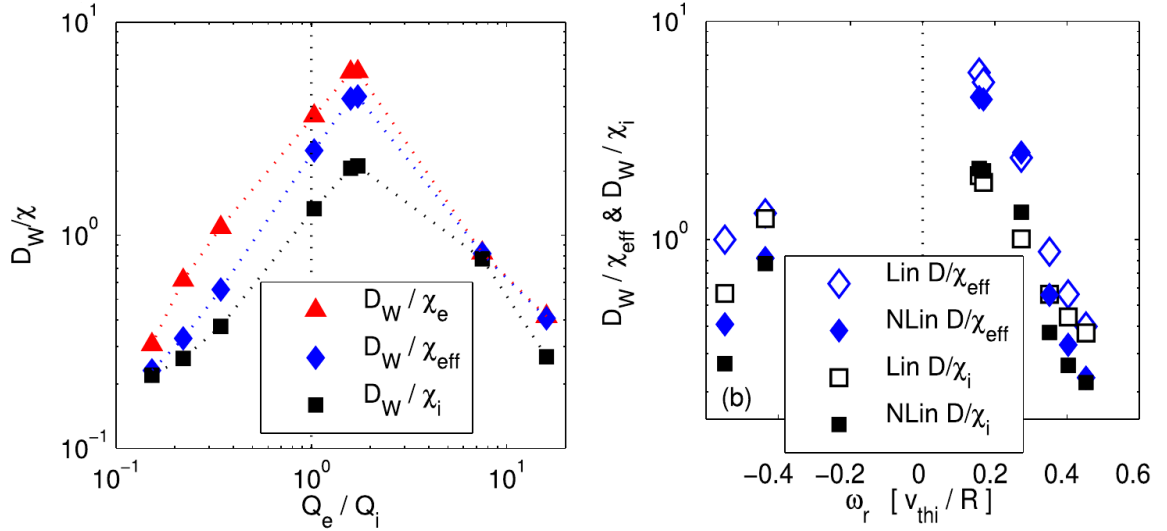
Figure 6.24.: Simulated tungsten diffusivity to heat conductivity ratio D/χ as a function of the electron to ion heat flux ratio Q_e/Q_i (left) and the real frequency of the unstable mode ω_r (right) from the study in Ref. [128].

simulation shown in chapter 5. Nevertheless, the same rising trend can be seen in the experimental data as well as in the gyrokinetic simulations. In order to verify the decrease of D/χ_i at higher electron heat fluxes seen on the left hand side of figure 6.24, experiments with a higher ratio of electron to ion heating must be conducted. Such experiments remain to be performed in the future.

To summarize, to avoid central impurity accumulation of any impurity, the impurity density profile should be hollow (positive drift velocity). In the database of this study, we saw that the majority of the observations had indeed a hollow boron density profile. These data points were obtained in plasmas which were dominantly NBI heated. The higher the NBI heating fraction, the more hollow were the boron density profiles. It was also observed that the boron density profiles were less peaked than the profiles of the main ions. From the standpoint of avoiding impurity accumulation, this is also a desired characteristic.

Additionally, the diffusion coefficient should preferably be high. Here it is worth noting that for our database, the highest diffusion and positive drift velocity is not obtained at the same time. The larges D is achieved for the peaked boron profiles, whereas the most hollow profiles have a more moderate value of the diffusivity.

The regressions deduced in the previous section for our boron database can be used as a first estimation for ITER. For D, the most relevant parameters were R/L_{n_e} and T_e/T_i and for v, u' and R/L_{n_e}. The values of these parameters foreseen for ITER are $R/L_{n_e} \approx 2$, $T_e/T_i \approx 1$, and $u' \approx 0$ [50]. Inserting these values in equations (6.6) and (6.7) yield $D = 3.11 \pm 0.5\,\mathrm{m^2/s}$ and $v = 1.77 \pm 0.19\,\mathrm{m/s}$. This suggests that the diffusivity would be moderate and the boron density profile would be hollow, which is indeed a desirable feature. Note however, that due to the scarce number of observations in the database only two regressors could be used. The plasma parameters in the database are also highly correlated with each other making it even harder to

pinpoint which are the most relevant ones. In order to be able to use more than two regressors, more experiments need to be performed in order to increase the size of the database. Additionally, more experimental data could perchance decorrelate the plasma parameters. It would perhaps then be clearer which plasma parameters are the most relevant ones for explaining the boron transport and more reliable projections for ITER could be drawn.

As a last comment, it is also worth emphasizing that steady-state studies conducted at AUG have shown that the transport of helium and boron seem to behave differently [45]. In the same plasma scenario, the value of $R/L_{n_{He}}$ was higher than the value of R/L_{n_B} meaning that the measured helium profile was more peaked than the measured boron profile. Since it was a steady-state study, it was not possible to individually deduce D and v. Here, future transient transport experiments need to be conducted to shed more light on the helium transport.

6.6. Conclusion

In this chapter we presented the transport coefficients of the complete boron database. These transport coefficients were obtained with the modulation method explained in chapter 5. The data was compared to a previous boron steady-state transport study also conducted at AUG. Despite the fact that the previous study was able to span a little bit wider parameter space, the two databases agree well with each other and both of them feature the same trends with plasma parameters. It was, for example, seen that the boron density profiles were always hollower or less peaked than the electron density profiles. This is a desired feature for a future devices, since it means that the impurity has a smaller inward transport than the one of the main ions and there is, hence, a smaller chance of central impurity accumulation.

In order to validate the impurity transport theory, the experimental results were also compared to neoclassical theory, calculated with the code NEO, and turbulent theory, simulated with the code GKW. The transport predicted by neoclassical theory can not describe the experimental observations and it can be concluded that the transport of the complete database is turbulence driven. For almost the whole database the experimental diffusivity was in good agreement with the turbulent diffusivity. The experimental convection, on the other hand, was always under predicted by the turbulent simulations meaning that the theory predicted more peaked boron density profiles than what was measured. The largest discrepancy in v between theory and experiment was seen for the most hollow boron density profiles. This indicates that an important piece of physics is missing in the theory. The attempts to explain the hollow impurity density profiles have so far rendered a bit better agreement. For example, the inclusion of fast ions in the gyrokinetic simulations results in a less negative convection than the simulation without fast ions. However, these attempts cannot yet fully bridge the gap between theory and experiment.

Scalings between the transport coefficients and plasma parameters were observed. In order to identify which plasma parameters are responsible for the observed trends in D and v, multiple linear regressions were performed. The two plasma parameters found to describe the data the best were for the diffusivity R/L_{n_e} and T_e/T_i and for the

convection u' and R/L_{n_e}. This result should, however, be taken with a grain of salt, since it is hard draw reliable conclusions from the statistical methods used on a dataset with such a limited number of observations.

Even though the turbulent transport theory is unable to properly explain the convection the agreement seen for the diffusivity is good. This is further strengthened by comparing the diffusion to ion heat conductivity ratio. In a purely theoretical study, it was earlier observed that this ratio follows a non-monotonic behavior as a function of the electron to ion heat flux ratio and obtaining a maximum at equal levels of electron and ion heat flux. These theoretical result could partly be verified by the boron data of the present study. In order to fully confirm this behavior experimentally, data with considerably higher electron heat flux compared to the ion heat flux must be obtained.

Chapter 7.

Conclusion and Outlook

7.1. Conclusion

Fusion plasmas are operated with hydrogen isotopes. Minor contributions from other elements are called impurities. Such impurities can stem from sputtering and erosion of the wall materials or be injected via gas puffing, pellets, and laser blow-off. Additionally, a future fusion reactor will produce helium ash. The main problems posed by the presence of impurities are fuel dilution and radiative power losses of the plasma, where the former is mainly caused by the low-Z impurities, such as helium and boron, and the latter by the high-Z impurities, such as tungsten. Too high impurity concentrations will have a detrimental effect on the fusion plasma performance and, therefore, impurity transport plays a critical role in creating a self-sustained burning plasma in a future fusion reactor. Since impurities will always, to some degree, be present in a fusion reactor, it is critical to understand and control the transport of both low- and high-Z impurities.

Particle transport can be described with the radial transport equation and it is characterized by diffusion, with the diffusion coefficient D, and convection, with the drift velocity v. In steady-state conditions, that is when the impurity density does not vary in time, only the ratio v/D can be obtained. This procedure is relatively straightforward and many of the previous transport studies only perform a steady-state analysis. To individually determine D and v, a transient transport analysis needs to be carried out. For that an impurity density signal varying in time is necessary. Normally, transient transport studies obtain such signals by injecting impurities via laser blow-off or gas puffing. Drawbacks of these two experimental methods are that they can cause a quite large perturbation to the background plasma.

In this thesis, we first presented a novel method of inducing a time modulated boron density signal at the ASDEX Upgrade (AUG) tokamak, which does not involve gas puffing or laser blow-off, and then how the core boron transport coefficients can be inferred from this time-dependent boron signal. Secondly, a database of boron transport coefficients was assembled and the deduced transport coefficients were compared to the theoretically predicted ones from neoclassical and gyrokinetic theory. This is a vital step, since the theory must be validated by present experimental transport investigations in order to employ the transport models and correctly predict the impurity transport in a future fusion device.

The analysis procedure starts with measuring the boron content in the plasma with the charge exchange recombination spectroscopy (CXRS) diagnostics, which yields data of high spatial and temporal resolution. The CXRS diagnostics provides a direct measurement of the intensity of the B^{5+} $(7 \rightarrow 6)$ charge exchange line actively excited by a charge exchange reaction with a neutral particle from the neutral beam injection heating. From the measured boron intensity, the boron density is calculated with the in-house code CHICA. For this, the neutral beam density and effective charge exchange emission rates must be known. In this code, the beam halo is also taken into account, which has been shown to have a non-negligible impact on the resulting impurity density profile. Great care was taken to cross-check that the different CXRS systems at AUG deliver the same shape of the boron density profile, which is the most important factor for transport analyses. Furthermore, it has been checked that the different beam attenuation codes available within CHICA deliver the same result.

The modulation of the boron density itself was induced by modulating the power of the ion cyclotron resonance heating (ICRH). The ICRH power is modulated as a square wave, with a frequency of $8 - 10 \, \text{Hz}$ and this results in a periodic modulation of the boron density with the same frequency. The boron modulation is strongest when the experiments are performed close to a boronization, which suggests that the boron is originating from the boron coating on the plasma facing components. The amplitude of the boron modulation scales with increasing ICRH power. However, increasing the level of the ICRH power modulation also increases the modulation of background plasma parameters such as the electron density, the electron temperature, and the ion temperature. An ICRH power level of $1 \, \text{MW}$ was chosen. It is enough to obtain a modulation of the edge boron density of $10 \, \%$ while keeping the modulation of the background plasma to less than $4 \, \%$. It was concluded that this method can be utilized in a wide variety of high confinement (H-mode) plasmas at AUG. Furthermore, with this technique multiple boron modulation cycles can be measured and analyzed, which reduces the statistical uncertainty. This is an advantage over other impurity modulation techniques such as gas puffing and laser blow-off, which often deduce the transport coefficients by analyzing a limited number of cycles or only even an individual cycle per measurement. In our experiments, $6 - 12$ boron modulation cycles were analyzed making one experimental segment $1 - 2$ seconds long.

The functional form of the resultant modulated boron density signal is well described by a sum of a cosine and a sine function with the frequency of the modulation. With this Ansatz for the reconstructed boron density, the transport coefficients can then be deduced from the radial transport equation by solving an inverse problem in the form of a minimization. This is a non-linear optimization problem, which is solved with Sequential Least SQuare Programming. Second order finite differences are used when solving the transport equation. The advantage of the Ansatz used is two-fold. Firstly, it describes the shape of the measured boron signal very well and secondly, it represents a Fourier transform in time which means that no time discretization is necessary and this in turn speeds up the computational time dramatically. The complete framework was benchmarked with the transport code STRAHL and verified with the Method of Manufactured Solutions. The resultant D and v profiles are represented by

arbitrary order B-splines, which impose smooth profiles. This is also a way of applying a regularization to the ill-posed inverse problem. The uncertainty on the transport coefficients were estimated with a Monte Carlo approach, where 10000 random samples were drawn from a multi-variate normal distribution of the experimental data. All in all, there is a very good agreement between the reconstructed and measured boron density thanks to the applied Ansatz and this method delivers highly spatially resolved transport coefficient profiles.

This method was applied in different H-mode plasma scenarios, where the heating power levels were varied as well as the plasma current and density profiles, and a database of boron transport coefficients was gathered. The values of the diffusivity in the database at mid-radius ranged from $2\,\text{m}^2/\text{s}$ up to $6\,\text{m}^2/\text{s}$. The boron density profiles were observed to vary from very hollow to peaked ones with the drift velocity values at mid-radius ranging between $-5\,\text{m/s}$ and $4\,\text{m/s}$. The experimental findings of this study were compared to a previous steady-state boron transport study also conducted at AUG [45]. For the normalized logarithmic boron density gradient, which is related to the ratio v/D, there is consistency between the two datasets and the same trends with plasma parameters were observed, even though the previous study was able to span a little bit wider parameter space. Clear trends between the transport coefficients and the gradients of the background temperatures, density, and toroidal flow velocity were observed in the database. It was also noted that the plasma parameters were highly correlated with each other, making it impossible to identify which of the plasma parameters are responsible for the trends seen in the transport coefficients. Despite this, a multiple linear regression analysis was performed to investigate the relative importance of the plasma parameters for D and v. Due to the limited number of observations in the database, only two regressors were adopted in the regressions. For the diffusivity, it was found that the parameters with the highest statistical significance were R/L_{n_e} and T_e/T_i, whereas for the drift velocity they were R/L_{n_e} and u'.

Additionally the database of the experimental boron transport coefficients was compared to the neoclassical and turbulent transport predictions. The neoclassical transport coefficients were considerably smaller than the experimental ones indicating that the transport in the performed experiments was turbulence driven. Comparing the experimental transport coefficients with the turbulent predictions from gyrokinetic theory showed a very good agreement in the diffusivity for almost the complete database. However, a discrepancy in the drift velocity v was observed. The theoretical v was always more inward (or less outward) than the experimental v, hence, the turbulent transport theory always predicted a more peaked boron density profile than what was experimentally measured. It was also observed that this discrepancy was worse for the most hollow boron density profiles meaning that there is still a piece of physics missing in the turbulent modeling especially for the hollow cases. The discrepancy for the most hollow impurity density profiles was also reported in other impurity transport studies [57, 106, 72, 45, 105, 101]. Work from the theoretical side is ongoing in trying to find what piece of physics is missing in the models to account for the transport of the hollow cases. Even though there is a discrepancy between the turbulent transport theory and the experiment for the drift velocity, there seem to be a good agreement

in the diffusivity. In a further step of validating the diffusivity, a good agreement was observed in the diffusion to ion heat conductivity ratio. An entirely theoretical study reported a non-monotonic behavior of this quantity as a function of the electron to ion heat flux ratio for tungsten [128], showing that this ratio is maximized when adding ECRH in a dominated NBI heated plasma or adding NBI in a dominated ECR heated plasma. If this behavior could be experimentally validated, it would be a useful piece of information for avoiding central impurity accumulation, especially for high-Z impurities. For boron we expect, theoretically, the same behavior and our experimental boron data is consistent with this.

To be certain to avoid central impurity accumulation in future fusion reactors, the impurity density profile should be hollow meaning a positive drift velocity. Additionally, the diffusion coefficient should be as high as possible. In our boron database, the experimental observations with hollow profiles were obtained in mainly NBI heated discharges and the cases with peaked profiles in plasmas where ECRH was the dominant heating source. It was, however, observed that the most peaked boron profiles also attained the highest value of the diffusion coefficient and the cases with hollow profiles obtained more moderate D values. At AUG, a parameter space has not yet been reached where we obtain both large diffusion and outward convection, hence the need to validate the theory. However, it was found that the boron density profile was always less peaked than the electron density profile, which is a desirable feature for a fusion reactor to avoid central impurity accumulation.

7.2. Outlook

The experimental method as well as the computational framework for deducing the transport coefficients show much potential. Therefore, it is safe to say that the findings presented in this thesis have only started to scratch the surface of possibilities regarding impurity transport analysis.

The numerical framework developed in this work is specially designed for a periodic sinusoidal-like density signal, which makes the computational process reliable and orders of magnitude faster than other similar approaches. However, that being said, it is also possible to modify it in order to handle a signal of another shape.

It was shown in chapter 6 that the gyrokientic codes are very sensitive to input gradients and the result of the simulation can vary significantly. The experimental profiles which go into these codes must be extracted from the discrete experimental data points and here the scientist is free to choose the level of smoothness of the data. A further improvement would then be to use Gaussian process regression [132, 133] for profile fitting instead of splines. Splines are commonly used in plasma physics to give a smooth representation of noisy experimental data, however, they suffer from several drawbacks. Manually setting the spline properties, such as the smoothing factor, is a source of systematic error when fitting profiles [134] and this often involves manual

hand tuning. Another disadvantage is the difficult and cumbersome uncertainty quantification for spline fits and their derivatives. One common approach here is to perform a brute force Monte Carlo sampling to obtain confidence intervals of the profiles and their derivatives. Parameterizing a profile with Gaussian processes is a Bayesian non-parametric regression technique [132, 133]. It is a stochastic process where all the assessed parameters are normally distributed, which makes it straightforward to evaluate the uncertainty of the fit without the need for a Monte Carlo approach like for the splines. Non-parametric means that the data itself give rise to the shape of the profile without the need for human intervention. Using Gaussian processes instead of splines when fitting the input profiles is a more rigorously and correct approach, which in the end would result in smaller uncertainties on the modeled parameters.

The next natural step would then be to cast the complete minimization problem in a Bayesian framework. Solving a *Bayesian inverse problem* has several advantages. First, setting the problem in a Bayesian statistical framework makes it well-posed. Second, just as for the Gaussian processes, it is unambiguous to assess the profile uncertainties of the deduced parameters. We would, hence, directly when solving the inverse problem obtain an accurate estimation of the transport coefficient uncertainties without the need for the brute force Monte Carlo approach used in this work. The ultimate goal would be to integrate the whole pipeline starting from the CXRS raw data, to the CHICA code and then finally to the deduced transport coefficients in a Bayesian framework. One way of implementation is to solve the transport equation along with other deterministic operations in Theano [135] and setting up the entire Bayesian framework using probabilistic programming [136]. Only in such a manner can all the various uncertainties completely be taken into account, understood, and also minimized.

From the experimental side, more boron modulation experiments should be conducted to expand the database. Firstly, a database with more observations would hopefully help to decorrelate the plasma parameters. It would then perhaps be easier to identify which plasma parameters are responsible for the trends seen in the transport coefficients. A larger database would also enable more regressors to be used in the multivariate linear regression, which would also help in identifying the most relevant plasma parameters. In particular, even more peaked boron density profiles, that is, experiments with an even higher level of ECRH power than obtained in this study is of highest interest. Such data with increased electron to ion heat flux ratio and electron to ion temperature ratio would finally be able to confirm or contradict the non-monotonic behavior seen in D/χ_i with respect to Q_e/Q_i from the gyrokinetic modeling and this is a further step in validating the turbulent transport theory.

Another interesting subject is to perform the boron modulation experiments in hydrogen plasmas, since this scenario effectively changes the mass ratio of boron to the main ion species from five to ten, which will influence the predictions of the profile gradients and transport coefficients from the gyrokinetic modeling. Therefore, these experiments would place an additional test on the theory and potentially provide more insight into the previously obtained discrepancy between the modeling and the ex-

perimental measurements. The first experiments to test the feasibility of the ICRH modulation method in hydrogen plasma have already taken place and rendered a positive result. The next step would then be to perform dedicated transport experiments in hydrogen plasmas to match the plasma parameters in an already existing deuterium case. The difference in the transport between hydrogen and deuterium can then be directly compared.

As already mentioned in chapter 4, the best theoretical validation is to measure several impurities simultaneously. The next step would then be to extend this boron modulation study to include other impurities. Even though the ICRH modulation does not seem to affect other impurities than boron, gas puffing experiments could be performed to obtain a time-dependent density signal for other impurities such as nitrogen and helium. A few tests have already been carried out puffing nitrogen, but so far the obtained nitrogen signal was not particularly stable and did not penetrate sufficiently deep into the plasma. A new piezo valve for gas injections was recently installed at AUG [137]. This new system enables gas injections with high duty cycles, making it ideal for transport studies. Due to the versatility of the system it should be possible to program the opening and closing of the piezo valve in such a way to obtain a steady modulated impurity signal such as the boron signal presented in this thesis. The already existing numerical framework could then be directly applied without the need for further modifications. To study the transport of helium is of highest interest for a future reactor, but the interpretation of the helium charge exchange spectra is hampered by an additional emission called the plume emission [32]. This makes the direct evaluation such as the one for boron or nitrogen not possible and to correctly determine the helium density, the plume effect must be modeled [138]. Therefore, the first plan is to puff nitrogen with this new valve, since the analysis of acquiring the nitrogen density from the measured nitrogen intensity is as straightforward as for boron. If this is successful, these puffing experiments could then be expanded to helium.

Bibliography

[1]   J. D. Lawson. "Some criteria for a power producing thermonuclear reactor". In: *Proceedings of the Physical Society. Section B* 70.1 (1957), p. 6. DOI: `https://doi.org/10.1088/0370-1301/70/1/303`.

[2]   D. Keefe. "Inertial confinement fusion". In: *Annual Review of Nuclear and Particle Science* 32.1 (1982), pp. 391–441.

[3]   J. Ongena et al. "Magnetic-confinement fusion". In: *Nature Physics* 12.5 (2016), p. 398. DOI: `https://doi.org/10.1038/nphys3745`.

[4]   *EUROfusion - European Consortium for the Development of Fusion Energy.* 2018. URL: `http://www.euro-fusion.org/`.

[5]   H. Zohm. *Magnetohydrodynamic stability of tokamaks.* John Wiley & Sons, 2014.

[6]   S. Von Goeler, W. Stodiek, and N. Sauthoff. "Studies of internal disruptions and m= 1 oscillations in tokamak discharges with soft—x-ray tecniques". In: *Physical Review Letters* 33.20 (1974), p. 1201. DOI: `https://doi.org/10.1103/PhysRevLett.33.1201`.

[7]   V. Shafranov. "Plasma equilibrium in a magnetic field". In: *Reviews of plasma physics* 2 (1966), p. 103.

[8]   F. M. Laggner. "Inter-ELM pedestal structure development in ASDEX Upgrade". Dissertation. Technische Universität Wien, 2017. URL: `https://pure.mpg.de/pubman/faces/ViewItemOverviewPage.jsp?itemId=item_2452969`.

[9]   F. Wagner et al. "Regime of improved confinement and high beta in neutral-beam-heated divertor discharges of the ASDEX tokamak". In: *Physical Review Letters* 49.19 (1982), p. 1408. DOI: `https://doi.org/10.1103/PhysRevLett.49.1408`.

[10] F. Ryter et al. "H-mode threshold and confinement in helium and deuterium in ASDEX Upgrade". In: *Nuclear Fusion* 49.6 (2009), p. 062003. DOI: `https://doi.org/10.1088/0029-5515/49/6/062003`.

[11] *Association EUROATOM-CEA Commissariat á l'Energie Atomique.* 2018. URL: `http://www-fusion-magnetique.cea.fr`.

[12] H. Zohm. "Edge localized modes (ELMs)". In: *Plasma Physics and Controlled Fusion* 38.2 (1996), p. 105. DOI: `https://doi.org/10.1088/0741-3335/38/2/001`.

[13] R. Dux. "Impurity transport in tokamak plasmas". Habilitation. Universität Augsburg, 2004. URL: `http://hdl.handle.net/11858/00-001M-0000-0027-2036-E`.

[14] A. Kallenbach et al. "Impurity seeding for tokamak power exhaust: from present devices via ITER to DEMO". In: *Plasma Physics and Controlled Fusion* 55.12 (2013), p. 124041. DOI: https://doi.org/10.1088/0741-3335/55/12/124041.

[15] A. Herrmann and O. Gruber. "Chapter 1: ASDEX Upgrade-Introduction and overview". In: *Fusion Science and Technology* 44.3 (2003), pp. 569–577. DOI: https://doi.org/10.13182/FST03-A399.

[16] R. Neu et al. "Plasma wall interaction and its implication in an all tungsten divertor tokamak". In: *Plasma Physics and Controlled Fusion* 49.12B (2007), B59. DOI: https://doi.org/10.1088/0741-3335/49/12B/S04.

[17] J. Wesson. *Tokamaks*. 4th ed. Oxford University Press, 2011.

[18] E. Speth. "Neutral beam heating of fusion plasmas". In: *Reports on Progress in Physics* 52.1 (1989), p. 57. DOI: https://doi.org/10.1088/0034-4885/52/1/002.

[19] B. Streibl et al. "Chapter 2: Machine design, fueling, and heating in ASDEX Upgrade". In: *Fusion science and technology* 44.3 (2003), pp. 578–592. DOI: https://doi.org/10.13182/FST03-A400.

[20] J. Stober et al. "ECRH on ASDEX Upgrade-System status, feed-back control, plasma physics results". In: *EPJ Web of Conferences*. Vol. 32. EDP Sciences. 2012, p. 02011.

[21] A. Kallenbach et al. "Non-boronized compared with boronized operation of ASDEX Upgrade with full-tungsten plasma facing components". In: *Nuclear Fusion* 49.4 (2009), p. 045007. DOI: https://doi.org/10.1088/0029-5515/49/4/045007.

[22] R. Neu et al. "New results from the tungsten programme at ASDEX Upgrade". In: *Journal of nuclear materials* 313 (2003), pp. 116–126. DOI: https://doi.org/10.1016/S0022-3115(02)01386-7.

[23] H. Faugel et al. "The ASDEX Upgrade ICRF system: Operational experience and developments". In: *Fusion engineering and design* 74.1 (2005), pp. 319–324. DOI: https://doi.org/10.1016/j.fusengdes.2005.06.268.

[24] T. Odstrčil. "On the Origin, Properties, and Implications of Asymmetries in the Tungsten Impurity Density in Tokamak Plasmas". Dissertation. Technische Universität München, 2017. URL: http://nbn-resolving.de/urn/resolver.pl?urn:nbn:de:bvb:91-diss-20170713-1357047-1-7.

[25] I. H. Hutchinson. *Principles of Plasma Diagnostics*. 2nd ed. Cambridge University Press, 2002.

[26] A. Mlynek et al. "Design of a digital multiradian phase detector and its application in fusion plasma interferometry". In: *Review of scientific instruments* 81.3 (2010), p. 033507. DOI: https://doi.org/10.1063/1.3340944.

[27] J. Schweinzer et al. "Reconstruction of plasma edge density profiles from Li I (2s-2p) emission profiles". In: *Plasma Physics and Controlled Fusion* 34.7 (1992), p. 1173. DOI: https://doi.org/10.1088/0741-3335/34/7/001.

[28] M. Willensdorfer et al. "Improved chopping of a lithium beam for plasma edge diagnostic at ASDEX Upgrade". In: *Review of scientific instruments* 83.2 (2012), p. 023501. DOI: `https://doi.org/10.1063/1.3682003`.

[29] B. Kurzan and H. Murmann. "Edge and core Thomson scattering systems and their calibration on the ASDEX Upgrade tokamak". In: *Review of scientific instruments* 82.10 (2011), p. 103501. DOI: `https://doi.org/10.1063/1.3643771`.

[30] N. Salmon. "First electron temperature edge measurements on the ASDEX Upgrade tokamak using a heterodyne radiometer". In: *International journal of infrared and millimeter waves* 15.1 (1994), pp. 53–60. DOI: `https://doi.org/10.1007/BF02265876`.

[31] R. Fischer et al. "Integrated data analysis of profile diagnostics at ASDEX Upgrade". In: *Fusion science and technology* 58.2 (2010), pp. 675–684. DOI: `https://doi.org/10.13182/FST10-110`.

[32] R. Fonck, D. Darrow, and K. Jaehnig. "Determination of plasma-ion velocity distribution via charge-exchange recombination spectroscopy". In: *Physical Review A* 29.6 (1984), p. 3288. DOI: `https://doi.org/10.1103/PhysRevA.29.3288`.

[33] R. Isler. "An overview of charge-exchange spectroscopy as a plasma diagnostic". In: *Plasma Physics and Controlled Fusion* 36.2 (1994), p. 171. DOI: `https://doi.org/10.1088/0741-3335/36/2/001`.

[34] A. Whiteford et al. "Atomic Data and Analysis Structure". In: (2007).

[35] E. Viezzer et al. "High-resolution charge exchange measurements at ASDEX Upgrade". In: *Review of scientific Instruments* 83.10 (2012), p. 103501. DOI: `https://doi.org/10.1063/1.4755810`.

[36] R. McDermott et al. "Extensions to the charge exchange recombination spectroscopy diagnostic suite at ASDEX Upgrade". In: *Review of Scientific Instruments* 88.7 (2017), p. 073508. DOI: `https://doi.org/10.1063/1.4993131`.

[37] *Princeton Instruments*. URL: `http://www.princetoninstruments.com`.

[38] R. E. Bell. "Exploiting a transmission grating spectrometer". In: *Review of scientific instruments* 75.10 (2004), pp. 4158–4161. DOI: `https://doi.org/10.1063/1.1787601`.

[39] M. Von Hellermann et al. "Analytical approximation of cross-section effects on charge exchange spectra observed in hot fusion plasmas". In: *Plasma physics and controlled fusion* 37.2 (1995), p. 71. DOI: `https://doi.org/10.1088/0741-3335/37/2/002`.

[40] R. E. Bell and E. Synakowski. "New understanding of poloidal rotation measurements in a tokamak plasma". In: *AIP Conference Proceedings*. Vol. 547. 1. AIP. 2000, pp. 39–52. DOI: `https://doi.org/10.1063/1.1361778`.

[41] P. Zeeman. "The effect of magnetisation on the nature of light emitted by a substance". In: *Nature* 55.347 (1897). DOI: `https://doi.org/10.1038/055347a0`.

[42] R. McDermott et al. "Evaluation of impurity densities from charge exchange recombination spectroscopy measurements at ASDEX Upgrade". In: *Plasma Physics and Controlled Fusion* 60.9 (2018), p. 095007. DOI: https://doi.org/10.1088/1361-6587/aad256.

[43] W. Heidbrink et al. "A code that simulates fast-ion D α and neutral particle measurements". In: *Communications in Computational Physics* 10.3 (2011), pp. 716–741. DOI: https://doi.org/10.4208/cicp.190810.080211a.

[44] H. P. Summers. *The ADAS User Manual, version 2.6*. 2004. URL: http://www.adas.ac.uk.

[45] A. Kappatou. "Investigations of helium transport in ASDEX Upgrade plasmas with charge exchange recombination spectroscopy". Dissertation. Technische Universiteit Eindhoven, 2014. URL: http://hdl.handle.net/11858/00-001M-0000-0029-5701-F.

[46] P. Helander and D. J. Sigmar. *Collisional transport in magnetized plasmas*. Vol. 4. Cambridge University Press, 2005.

[47] S. Hirshman and D. Sigmar. "Neoclassical transport of impurities in tokamak plasmas". In: *Nuclear Fusion* 21.9 (1981), p. 1079. DOI: https://doi.org/10.1088/0029-5515/21/9/003.

[48] R. Dux et al. "Z dependence of the core impurity transport in ASDEX Upgrade H mode discharges". In: *Nuclear Fusion* 39.11 (1999), p. 1509. DOI: https://doi.org/10.1088/0029-5515/39/11/302.

[49] R. Guirlet et al. "Parametric dependences of impurity transport in tokamaks". In: *Plasma physics and controlled fusion* 48.12B (2006), B63. DOI: https://doi.org/10.1088/0741-3335/48/12B/S06.

[50] ITER EDA. "Plasma confinement and transport". In: *Nuclear Fusion* 39.12 ITER physics basis (1999), pp. 2175–2249. DOI: https://doi.org/10.1088/0029-5515/39/12/301.

[51] A. Ware. "Pinch-Effect oscillations in an unstable tokamak plasma". In: *Physical Review Letters* 25.14 (1970), p. 916. DOI: https://doi.org/10.1103/PhysRevLett.25.916.

[52] E. Scavino et al. "Effects of ECRH power and safety factor on laser blow-off injected impurity confinement in TCV". In: *Plasma physics and controlled fusion* 46.5 (2004), p. 857. DOI: https://doi.org/10.1088/0741-3335/46/5/008.

[53] R. Dux et al. "Influence of the heating profile on impurity transport in ASDEX Upgrade". In: *Plasma Physics and Controlled Fusion* 45.9 (2003), p. 1815. DOI: https://doi.org/10.1088/0741-3335/45/9/317.

[54] M. Puiatti et al. "Analysis of metallic impurity density profiles in low collisionality Joint European Torus H-mode and L-mode plasmas". In: *Physics of Plasmas* 13.4 (2006), p. 042501. DOI: https://doi.org/10.1063/1.2187424.

[55] C. Giroud et al. "Method for experimental determination of Z dependence of impurity transport on JET". In: *Nuclear fusion* 47.4 (2007), p. 313. DOI: https://doi.org/10.1088/0029-5515/47/4/010.

[56] T. Parisot et al. "Experimental impurity transport and theoretical interpretation in a Tore Supra lower-hybrid heated plasma". In: *Plasma Physics and Controlled Fusion* 50.5 (2008), p. 055010. DOI: https://doi.org/10.1088/0741-3335/50/5/055010.

[57] C. Angioni et al. "Gyrokinetic modelling of electron and boron density profiles of H-mode plasmas in ASDEX Upgrade". In: *Nuclear Fusion* 51.2 (2011), p. 023006. DOI: https://doi.org/10.1088/0029-5515/51/2/023006.

[58] M. Sertoli et al. "Local effects of ECRH on argon transport in L-mode discharges at ASDEX Upgrade". In: *Plasma Physics and Controlled Fusion* 53.3 (2011), p. 035024. DOI: https://doi.org/10.1088/0741-3335/53/3/035024.

[59] N. Howard et al. "Quantitative comparison of experimental impurity transport with nonlinear gyrokinetic simulation in an Alcator C-Mod L-mode plasma". In: *Nuclear Fusion* 52.6 (2012), p. 063002. DOI: https://doi.org/10.1088/0029-5515/52/6/063002.

[60] B. A. Grierson et al. "Impurity confinement and transport in high confinement regimes without edge localized modes on DIII-D". In: *Physics of Plasmas* 22.5 (2015), p. 055901. DOI: https://doi.org/10.1063/1.4918359.

[61] T. Pütterich et al. "ELM flushing and impurity transport in the H-mode edge barrier in ASDEX Upgrade". In: *Journal of Nuclear Materials* 415.1 (2011), S334–S339. DOI: https://doi.org/10.1016/j.jnucmat.2010.09.052.

[62] A. Peeters. "Reduced charge state equations that describe Pfirsch Schlüter impurity transport in tokamak plasma". In: *Physics of Plasmas* 7.1 (2000), pp. 268–275. DOI: https://doi.org/10.1063/1.873812.

[63] E. Scavino et al. "Effects of plasma shape on laser blow-off injected impurity transport in TCV". In: *Plasma physics and controlled fusion* 45.11 (2003), p. 1961. DOI: https://doi.org/10.1088/0741-3335/45/11/002.

[64] F. Romanelli. "Ion temperature-gradient-driven modes and anomalous ion transport in tokamaks". In: *Physics of Fluids B: Plasma Physics* 1.5 (1989), pp. 1018–1025. DOI: https://doi.org/10.1063/1.859023.

[65] B. Coppi and F. Pegoraro. "Theory of the ubiquitous mode". In: *Nuclear Fusion* 17.5 (1977), p. 969. DOI: https://doi.org/10.1088/0029-5515/17/5/009.

[66] J. Weiland. *Collective Modes in Inhomogeneous Plasmas: Kinetic and Advanced Fluid Theory*. CRC Press, 1999.

[67] U. Stroth. *Plasmaphysik: Phänomene, Grundlagen, Anwendungen*. Studium (Vieweg + Teubner). Vieweg+Teubner Verlag, 2011. ISBN: 9783834816153. URL: https://books.google.se/books?id=p6xcX_I33kMC.

[68] J. Weiland, A. Jarmen, and H. Nordman. "Diffusive particle and heat pinch effects in toroidal plasmas". In: *Nuclear Fusion* 29.10 (1989), p. 1810. DOI: https://doi.org/10.1088/0029-5515/29/10/015.

[69] B. Coppi and G. Rewoldt. "New trapped-electron instability". In: *Physical Review Letters* 33.22 (1974), p. 1329. DOI: https://doi.org/10.1103/PhysRevLett.33.1329.

[70] B. Kadomtsev and O. Pogutse. "Trapped particles in toroidal magnetic systems". In: *Nuclear Fusion* 11.1 (1971), p. 67. DOI: `https://doi.org/10.1088/0029-5515/11/1/010`.

[71] C. Angioni and A. Peeters. "Direction of impurity pinch and auxiliary heating in tokamak plasmas". In: *Physical review letters* 96.9 (2006), p. 095003. DOI: `https://doi.org/10.1103/PhysRevLett.96.095003`.

[72] F. Casson et al. "Validation of gyrokinetic modelling of light impurity transport including rotation in ASDEX Upgrade". In: *Nuclear Fusion* 53.6 (2013), p. 063026. DOI: `https://doi.org/10.1088/0029-5515/53/6/063026`.

[73] Y. Camenen et al. "Impact of the background toroidal rotation on particle and heat turbulent transport in tokamak plasmas". In: *Physics of Plasmas* 16.1 (2009), p. 012503. DOI: `https://doi.org/10.1063/1.3057356`.

[74] E. A. Belli and J. Candy. "Kinetic calculation of neoclassical transport including self-consistent electron and impurity dynamics". In: *Plasma Physics and Controlled Fusion* 50.9 (2008), p. 095010. DOI: `https://doi.org/10.1088/0741-3335/50/9/095010`. URL: `http://stacks.iop.org/0741-3335/50/i=9/a=095010`.

[75] E. A. Belli and J. Candy. "Full linearized Fokker–Planck collisions in neoclassical transport simulations". In: *Plasma Physics and Controlled Fusion* 54.1 (2012), p. 015015. DOI: `https://doi.org/10.1088/0741-3335/54/1/015015`. URL: `http://stacks.iop.org/0741-3335/54/i=1/a=015015`.

[76] A. Peeters et al. "The nonlinear gyro-kinetic flux tube code {GKW}". In: *Computer Physics Communications* 180.12 (2009). 40 {YEARS} {OF} CPC: A celebratory issue focused on quality software for high performance, grid and novel computing architectures, pp. 2650 –2672. ISSN: 0010-4655. DOI: `http://dx.doi.org/10.1016/j.cpc.2009.07.001`. URL: `http://www.sciencedirect.com/science/article/pii/S0010465509002112`.

[77] M. Sato et al. "Impurity Behavior in JIPP T–II Tokamak Plasma". In: *Journal of the Physical Society of Japan* 50.6 (1981), pp. 2114–2121. DOI: `https://doi.org/10.1143/JPSJ.50.2114`.

[78] TFR Group. "Light impurity transport in the TFR tokamak: Comparison of oxygen and carbon line emission with numerical simulations". In: *Nuclear Fusion* 22.9 (1982), p. 1173. DOI: `https://doi.org/10.1088/0029-5515/22/9/004`.

[79] F. De Marco, R Giannella, and G Mazzitelli. "Behaviour of oxygen impurities in the Frascati Tokamak". In: *Plasma Physics* 24.3 (1982), p. 257. DOI: `https://doi.org/10.1088/0032-1028/24/3/004`.

[80] TFR Group. "Heavy-impurity transport in the TFR tokamak–comparison of line emission with numerical simulations". In: *Nuclear Fusion* 23.5 (1983), p. 559. DOI: `10.1088/0029-5515/23/5/001`.

[81] C. Angioni et al. "Tungsten transport in JET H-mode plasmas in hybrid scenario, experimental observations and modelling". In: *Nuclear Fusion* 54.8 (2014), p. 083028. DOI: `https://doi.org/10.1088/0029-5515/54/8/083028`.

[82] C. Angioni et al. "Gyrokinetic study of turbulent convection of heavy impurities in tokamak plasmas at comparable ion and electron heat fluxes". In: *Nuclear Fusion* 57.2 (2016), p. 022009. DOI: https://doi.org/10.1088/0029-5515/57/2/022009.

[83] C. Angioni et al. "Density response to central electron heating: theoretical investigations and experimental observations in ASDEX Upgrade". In: *Nuclear Fusion* 44.8 (2004), p. 827. DOI: https://doi.org/10.1088/0029-5515/44/8/003.

[84] E. Fable, C Angioni, and O Sauter. "The role of ion and electron electrostatic turbulence in characterizing stationary particle transport in the core of tokamak plasmas". In: *Plasma Physics and Controlled Fusion* 52.1 (2009), p. 015007. DOI: https://doi.org/10.1088/0741-3335/52/1/015007.

[85] C. Angioni et al. "Off-diagonal particle and toroidal momentum transport: a survey of experimental, theoretical and modelling aspects". In: *Nuclear Fusion* 52.11 (2012), p. 114003. DOI: https://doi.org/10.1088/0029-5515/52/11/114003.

[86] C. Angioni et al. "Relationship between density peaking, particle thermodiffusion, Ohmic confinement, and microinstabilities in ASDEX Upgrade L-mode plasmas". In: *Physics of plasmas* 12.4 (2005), p. 040701. DOI: https://doi.org/10.1063/1.1867492.

[87] M. Wade et al. "Helium transport and exhaust studies in enhanced confinement regimes in DIII-D". In: *Physics of Plasmas* 2.6 (1995), pp. 2357–2365. DOI: https://doi.org/10.1063/1.871489.

[88] N. Howard et al. "Measurement of plasma current dependent changes in impurity transport and comparison with nonlinear gyrokinetic simulation". In: *Physics of Plasmas* 19.5 (2012), p. 056110. DOI: https://doi.org/10.1063/1.3694113.

[89] J. Rice et al. "Core impurity transport in Alcator C-Mod L-, I-and H-mode plasmas". In: *Nuclear Fusion* 55.3 (2015), p. 033014. DOI: https://doi.org/10.1088/0029-5515/55/3/033014.

[90] M. Valisa et al. "Metal impurity transport control in JET H-mode plasmas with central ion cyclotron radiofrequency power injection". In: *Nuclear Fusion* 51.3 (2011), p. 033002. DOI: https://doi.org/10.1088/0029-5515/51/3/033002.

[91] M. Graf et al. "Spectroscopic measurement of impurity transport coefficients and penetration efficiencies in Alcator C-Mod plasmas". In: *Review of scientific instruments* 66.1 (1995), pp. 636–638. DOI: https://doi.org/10.1063/1.1146311.

[92] A. Loarte et al. "Tungsten impurity transport experiments in Alcator C-Mod to address high priority research and development for ITER". In: *Physics of Plasmas* 22.5 (2015), p. 056117. DOI: https://doi.org/10.1063/1.4921253.

[93] K. Krieger, G. Fußmann, et al. "Determination of impurity transport coefficients by harmonic analysis". In: *Nuclear Fusion* 30.11 (1990), p. 2392. DOI: https://doi.org/10.1088/0029-5515/30/11/015.

[94] M. Sertoli, R. Dux, T. Pütterich, et al. "Modification of impurity transport in the presence of saturated (m, n)=(1, 1) MHD activity at ASDEX Upgrade". In: *Plasma Physics and Controlled Fusion* 57.7 (2015), p. 075004. DOI: `https://doi.org/10.1088/0741-3335/57/7/075004`.

[95] M. Sertoli et al. "Parametric dependencies of the experimental tungsten transport coefficients in ICRH and ECRH assisted ASDEX Upgrade H-modes". In: *Physics of Plasmas* 24.11 (2017), p. 112503. DOI: `https://doi.org/10.1063/1.4996412`.

[96] S. Henderson et al. "Neoclassical and gyrokinetic analysis of time-dependent helium transport experiments on MAST". In: *Nuclear Fusion* 54.9 (2014), p. 093013. DOI: `https://doi.org/10.1088/0029-5515/54/9/093013`.

[97] S. Henderson et al. "Charge dependence of neoclassical and turbulent transport of light impurities on MAST". In: *Plasma Physics and Controlled Fusion* 57.9 (2015), p. 095001. DOI: `https://doi.org/10.1088/0741-3335/57/9/095001`.

[98] D. Pasini et al. "Measurements of impurity transport in JET". In: *Plasma physics and controlled fusion* 34.5 (1992), p. 677. DOI: `https://doi.org/10.1088/0029-5515/30/10/007`.

[99] M. Puiatti et al. "Radiation pattern and impurity transport in argon seeded ELMy H-mode discharges in JET". In: *Plasma Physics and Controlled Fusion* 44.9 (2002), p. 1863. DOI: `https://doi.org/10.1088/0741-3335/44/9/305`.

[100] M. Puiatti et al. "Simulation of the time behaviour of impurities in JET Ar-seeded discharges and its relation with sawtoothing and RF heating". In: *Plasma physics and controlled fusion* 45.12 (2003), p. 2011. DOI: `https://doi.org/10.1088/0741-3335/45/12/003`.

[101] N. Bonanomi et al. "Light impurity transport in JET ILW L-mode plasmas". In: *Nuclear Fusion* 58.3 (2018), p. 036009. DOI: `https://doi.org/10.1088/1741-4326/aaa4d3`.

[102] J. Hong et al. "Control of core argon impurity profile by ECH in KSTAR L-mode plasmas". In: *Nuclear Fusion* 55.6 (2015), p. 063016. DOI: `https://doi.org/10.1088/0029-5515/55/6/063016`.

[103] D. Villegas et al. "Experimental electron temperature gradient dependence of heavy impurity transport in fusion devices". In: *Physical review letters* 105.3 (2010), p. 035002. DOI: `https://doi.org/10.1103/PhysRevLett.105.035002`.

[104] D. Villegas et al. "Experimental and theoretical study of nickel transport dependence on gradients in Tore Supra". In: *Nuclear Fusion* 54.7 (2014), p. 073011. DOI: `https://doi.org/10.1088/0029-5515/54/7/073011`.

[105] P. Manas et al. "Gyrokinetic modeling of impurity peaking in JET H-mode plasmas". In: *Physics of Plasmas* 24.6 (2017), p. 062511. DOI: `https://doi.org/10.1063/1.4985330`.

[106] H. Nordman et al. "Fluid and gyrokinetic simulations of impurity transport at JET". In: *Plasma Physics and Controlled Fusion* 53.10 (2011), p. 105005. DOI: `https://doi.org/10.1088/0741-3335/53/10/105005`.

[107] A. Jacchia et al. "Determination of diffusive and nondiffusive transport in modulation experiments in plasmas". In: *Physics of Fluids B: Plasma Physics* 3.11 (1991), pp. 3033–3040. DOI: https://doi.org/10.1063/1.859781.

[108] F. Sommer et al. "Transport properties of H-mode plasmas with dominant electron heating in comparison to dominant ion heating at ASDEX Upgrade". In: *Nuclear Fusion* 55.3 (2015), p. 033006. DOI: https://doi.org/10.1088/0029-5515/55/3/033006.

[109] M. Nave et al. "Role of sawtooth in avoiding impurity accumulation and maintaining good confinement in JET radiative mantle discharges". In: *Nuclear fusion* 43.10 (2003), p. 1204. DOI: https://doi.org/10.1088/0029-5515/43/10/023.

[110] T. Pütterich et al. "Observations on the W-transport in the core plasma of JET and ASDEX Upgrade". In: *Plasma Physics and Controlled Fusion* 55.12 (2013), p. 124036. DOI: https://doi.org/10.1088/0741-3335/55/12/124036.

[111] C. Bruhn et al. "A novel method of studying the core boron transport at ASDEX Upgrade". In: *Plasma Physics and Controlled Fusion* 60.8 (2018). DOI: https://doi.org/10.1088/1361-6587/aac870.

[112] F. Perkins. "Radiofrequency sheaths and impurity generation by ICRF antennas". In: *Nuclear Fusion* 29.4 (1989), p. 583. DOI: https://doi.org/10.1088/0029-5515/29/4/004.

[113] H. Manning et al. "Impurity generation during ICRF heating experiments on Alcator C". In: *Nuclear fusion* 26.12 (1986), p. 1665. DOI: https://doi.org/10.1088/0029-5515/26/12/008.

[114] J. Myra, D. D'Ippolito, and M. Gerver. "Faraday screen sheaths and impurity production during ion cyclotron heating". In: *Nuclear fusion* 30.5 (1990), p. 845. DOI: https://doi.org/10.1088/0029-5515/30/5/004.

[115] D. D'Ippolito et al. "A model of sheath-driven impurity production by ICRF antennas". In: *Plasma Physics and Controlled Fusion* 33.6 (1991), p. 607. DOI: https://doi.org/10.1088/0741-3335/33/6/005.

[116] M. A. Janzer. "Tungsten transport in the plasma edge at ASDEX Upgrade". Dissertation. Ludwig-Maximilians-Universität München, 2015. URL: http://nbn-resolving.de/urn:nbn:de:bvb:19-187453.

[117] V. Bobkov et al. "First results with 3-strap ICRF antennas in ASDEX Upgrade". In: *Nuclear Fusion* 56.8 (2016), p. 084001. DOI: https://doi.org/10.1088/0029-5515/56/8/084001.

[118] J. Winter et al. "Boronization in TEXTOR". In: *Journal of Nuclear Materials* 162 (1989), pp. 713–723. DOI: https://doi.org/10.1016/0022-3115(89)90352-8.

[119] V. Rohde et al. "Comparison of boronization and siliconization in ASDEX Upgrade". In: *26th EPS Conference on Controlled Fusion and Plasma Physics*. European Physical Society. 1999. URL: http://hdl.handle.net/11858/00-001M-0000-0028-E324-F.

[120] H. Takenaga et al. "Determination of particle transport coefficients in reversed shear plasma of JT-60U". In: *Plasma physics and controlled fusion* 40.2 (1998), p. 183. DOI: https://doi.org/10.1088/0741-3335/40/2/002.

[121] D. Kraft. *A software package for sequential quadratic programming*. Tech. rep. DFVLR-FB 88-28. Forschungsbericht- Deutsche Forschungs- und Versuchsanstalt fur Luft- und Raumfahrt, 1988.

[122] E. Jones, T. Oliphant, P. Peterson, et al. *SciPy: Open source scientific tools for Python*. 2001–. URL: http://www.scipy.org/.

[123] K. Salari and P. Knupp. *Code verification by the method of manufactured solutions*. Tech. rep. SAND2000-1444. Sandia National Labs., 2000. DOI: https://doi.org/10.2172/759450.

[124] P. J. Roache. "Code verification by the method of manufactured solutions". In: *Transactions-American Society of Mechanical Engineers Journal of Fluids Engineering* 124.1 (2002), pp. 4–10. DOI: http://doi.org/10.1115/1.1436090.

[125] H. Wilson. "Neoclassical tearing modes". In: *Fusion science and technology* 49.2T (2006), pp. 155–163. DOI: https://doi.org/10.13182/FST12-A13498.

[126] R. Dux. *STRAHL User Manual*. Tech. rep. IPP 10/30. 2014. URL: http://hdl.handle.net/11858/00-001M-0000-0027-0DB8-4.

[127] A. Pankin et al. "The tokamak Monte Carlo fast ion module NUBEAM in the National Transport Code Collaboration library". In: *Computer Physics Communications* 159.3 (2004), pp. 157–184. DOI: https://doi.org/10.1016/j.cpc.2003.11.002.

[128] C. Angioni. "Gyrokinetic study of the impact of the electron to ion heating ratio on the turbulent diffusion of highly charged impurities". In: *Physics of Plasmas* 22.10 (2015), p. 102501. DOI: https://doi.org/10.1063/1.4932070.

[129] P. Manas, A. Kappatou, and C. Angioni. "Light impurity turbulent transport in tokamaks: on the role of neutral beam fast ions". In: *Nuclear Fusion* (2018). to be submitted.

[130] D. Estève et al. "Self-consistent gyrokinetic modeling of neoclassical and turbulent impurity transport". In: *Nuclear Fusion* 58.3 (2018), p. 036013. DOI: https://doi.org/10.1088/1741-4326/aa6ebb.

[131] P. Manas et al. "Impact of the neoclassical distribution function on turbulent impurity and momentum fluxes: fluid model and gyrokinetic simulations". In: *Plasma Physics and Controlled Fusion* 59.3 (2017), p. 035002. DOI: https://doi-org.eaccess.ub.tum.de/10.1088/1361-6587/aa52e.

[132] D. Barber. *Bayesian reasoning and machine learning*. Cambridge University Press, 2012. URL: http://www.cs.ucl.ac.uk/staff/d.barber/brml/.

[133] M. Chilenski et al. "Improved profile fitting and quantification of uncertainty in experimental measurements of impurity transport coefficients using Gaussian process regression". In: *Nuclear Fusion* 55.2 (2015), p. 023012. DOI: https://doi.org/10.1088/0029-5515/55/2/023012.

[134] C. Holland et al. "Implementation and application of two synthetic diagnostics for validating simulations of core tokamak turbulence". In: *Physics of Plasmas* 16.5 (2009), p. 052301. DOI: https://doi.org/10.1063/1.3085792.

[135] Theano Development Team. "Theano: A Python framework for fast computation of mathematical expressions". In: *arXiv e-prints* abs/1605.02688 (May 2016). URL: http://arxiv.org/abs/1605.02688.

[136] J. Salvatier, T. V. Wiecki, and C. Fonnesbeck. "Probabilistic programming in Python using PyMC3". In: *PeerJ Computer Science* 2 (2016), e55.

[137] M. Griener et al. "Fast piezoelectric valve offering controlled gas injection in magnetically confined fusion plasmas for diagnostic and fuelling purposes". In: *Review of scientific instruments* 88.3 (2017), p. 033509. DOI: https://doi.org/10.1063/1.4978629.

[138] A. Kappatou et al. "A forward model for the helium plume effect and the interpretation of helium charge exchange measurements at ASDEX Upgrade". In: *Plasma Physics and Controlled Fusion* 60.5 (2018), p. 055006. DOI: https://doi.org/10.1088/1361-6587/aab25a.

Bibliography

114

Appendix

Appendix A.

Appendix

A.1. Derivation of analytical expressions for D and v

Suppose that the density $n(r,t)$ consists of a time independent background $n_0(r)$, the steady-state, and on top of this a small oscillation $n_\omega(r,t)$ at a given frequency ω. We can make the following Ansatz for the density:

$$n(r,t) := n_0(r) + n_\omega(r,t), \qquad n_\omega(r,t) := a(r)\cos(\omega t) + b(r)\sin(\omega t). \tag{A.1}$$

Since the radial transport equation is linear in time, we can independently insert n_0 and n_ω and obtain two equations. For the steady-state $n_0(r)$ the time derivative is zero:

$$\underbrace{\partial_t n_0(r)}_{=0} = \frac{1}{r}\frac{\partial}{\partial r}\left[r\left(D(r)\frac{\partial n_0(r)}{\partial r} - v(r)\cdot n_0(r)\right)\right]. \tag{A.2}$$

We obtain a single equation which allows us to acquire the ratio between the drift velocity and the diffusivity,

$$D(r)\frac{\partial n_0(r)}{\partial r} - v(r)\cdot n_0(r) = 0, \tag{A.3}$$

resulting in:

$$\frac{v(r)}{D(r)} = \underbrace{\frac{1}{n_0(r)}\frac{\partial n_0(r)}{\partial r}}_{\text{``normalized gradient``}}. \tag{A.4}$$

Continuing and inserting $n_\omega(r,t)$ in the transport equation equation (4.14) yields:

$$-\omega a(r)\sin(\omega t) + \omega b(r)\cos(\omega t)$$
$$= \frac{1}{r}\frac{\partial}{\partial r}\left[r\left[D(r)\left(a'(r)\cos(\omega t) + b'(r)\sin(\omega t)\right) - v(r)\left(a(r)\cos(\omega t) + b(r)\sin(\omega t)\right)\right]\right]. \tag{A.5}$$

We again sort the $\sin(\omega t)$ and $\cos(\omega t)$ terms in order to obtain two separate equations.

$$-\omega a(r)r = \frac{\partial}{\partial r}r\left[D(r)b'(r) - v(r)b(r)\right] \tag{A.6}$$

$$\omega b(r)r = \frac{\partial}{\partial r}r\left[D(r)a'(r) - v(r)a(r)\right] \tag{A.7}$$

Appendix A. Appendix

We integrate from 0 to r in order for the offset at $r = 0$ to drop out. From the n_0 mode we obtain a third equation, which makes the system overdetermined if n_0, a, and b are given from experimental data.

$$-\frac{\omega}{r} \int_0^r a(\tilde{r})\tilde{r} \, \mathrm{d}\tilde{r} = D(r)b'(r) - v(r)b(r) \tag{A.8}$$

$$\frac{\omega}{r} \int_0^r b(\tilde{r})\tilde{r} \, \mathrm{d}\tilde{r} = D(r)a'(r) - v(r)a(r) \tag{A.9}$$

$$v(r) = \frac{n_0'(r)}{n_0(r)}D(r) \tag{A.10}$$

Therefore, we obtain an additional equation for n_0, a, and b which should be considered when estimating the profiles from the measured data. We start with eliminating $v(r)$.

$$-\frac{\omega}{r} \int_0^r a(\tilde{r})\tilde{r} \, \mathrm{d}\tilde{r} = D(r)\left(b'(r) - \frac{n_0'(r)}{n_0(r)}b(r)\right) \tag{A.11}$$

$$\frac{\omega}{r} \int_0^r b(\tilde{r})\tilde{r} \, \mathrm{d}\tilde{r} = D(r)\left(a'(r) - \frac{n_0'(r)}{n_0(r)}a(r)\right) \tag{A.12}$$

Rearranging terms,

$$-\frac{1}{b(r)} \int_0^r a(\tilde{r})\tilde{r} \, \mathrm{d}\tilde{r} = \frac{D(r)r}{\omega}\left(\frac{b'(r)}{b(r)} - \frac{n_0'(r)}{n_0(r)}\right) \tag{A.13}$$

$$\frac{1}{a(r)} \int_0^r b(\tilde{r})\tilde{r} \, \mathrm{d}\tilde{r} = \frac{D(r)r}{\omega}\left(\frac{a'(r)}{a(r)} - \frac{n_0'(r)}{n_0(r)}\right), \tag{A.14}$$

we can eliminate the $\frac{D(r)r}{\omega}$ and obtain an equation only depending on the three estimated profiles n_0, a, and b:

$$\frac{1}{b(r)} \int_0^r a(\tilde{r})\tilde{r} \, \mathrm{d}\tilde{r} \left(\frac{a'(r)}{a(r)} - \frac{n_0'(r)}{n_0(r)}\right)$$
$$+ \frac{1}{a(r)} \int_0^r b(\tilde{r})\tilde{r} \, \mathrm{d}\tilde{r} \left(\frac{b'(r)}{b(r)} - \frac{n_0'(r)}{n_0(r)}\right) = 0 \text{ for all } r > 0. \tag{A.15}$$

Reordering terms to remove the profiles from the denominator makes the constraint less stiff:

$$\int_0^r a(\tilde{r})\tilde{r} \, \mathrm{d}\tilde{r} \, (a'(r)n_0(r) - a(r)n_0'(r))$$
$$+ \int_0^r b(\tilde{r})\tilde{r} \, \mathrm{d}\tilde{r} \, (b'(r)n_0(r) - b(r)n_0'(r)) = 0 \text{ for all } r > 0. \tag{A.16}$$

If equation (A.16) is fulfilled the desired profiles of v and D are given as:

$$D(r) = -\frac{\omega \int_0^r a(\tilde{r})\tilde{r} \, \mathrm{d}\tilde{r}}{r\left(b'(r) - \frac{n_0'(r)}{n_0(r)}b(r)\right)} = \frac{\omega \int_0^r b(\tilde{r})\tilde{r} \, \mathrm{d}\tilde{r}}{r\left(a'(r) - \frac{n_0'(r)}{n_0(r)}a(r)\right)} \tag{A.17}$$

$$v(r) = \frac{n_0'(r)}{n_0(r)}D(r) = -\frac{\omega \, n_0'(r) \int_0^r a(\tilde{r})\tilde{r} \, \mathrm{d}\tilde{r}}{r\left(n_0 b'(r) - n_0'(r)b(r)\right)}. \tag{A.18}$$

A.2. Second order finite difference discretization

We start by re-writing the radial transport equation

$$\partial_t n(r,t) = \frac{1}{r}\frac{\partial}{\partial r}\left[r\left(D(r)\frac{\partial n(r,t)}{\partial r} - v(r)\cdot n(r,t)\right)\right] \tag{A.19}$$

in another form:

$$\partial_t n(r,t) = \frac{1}{r}\left(D(r)\frac{\partial n(r,t)}{\partial r} - v(r)\cdot n(r,t)\right) +$$

$$\left(D'(r)\frac{\partial n(r,t)}{\partial r} + D(r)\frac{\partial^2 n(r,t)}{\partial r^2} - v'(r)\cdot n(r,t) - v(r)\cdot \frac{\partial n(r,t)}{\partial r}\right)$$

$$= D(r)\frac{\partial^2 n(r,t)}{\partial r^2} + \left(\frac{D(r)}{r} + D'(r) - v(r)\right)\frac{\partial n(r,t)}{\partial r} - \left(\frac{v(r)}{r} + v'(r)\right)n(r,t). \tag{A.20}$$

Considering only the steady-state ($\partial_t n(r,t) = 0$), this equation can be written as:

$$rD(r)\frac{\partial^2 n(r,t)}{\partial r^2} + (D(r) + rD'(r) - rv(r))\frac{\partial n(r,t)}{\partial r} - (v(r) + rv'(r))\,n(r,t) = 0. \tag{A.21}$$

For outlining the discretization scheme it is helpful to start with the steady-state inverse problem:

$$\min_{D,v,s_0}\frac{1}{2}\|n_0 - n_d\|^2 \qquad \text{such that} \tag{A.22}$$

$$\frac{1}{r}\frac{\partial}{\partial r}\left[r\left(D(r)n'(r) - v(r)\cdot n(r)\right)\right] = 0 \tag{A.23}$$

$$n(r_{max}) = s_0 \tag{A.24}$$

$$n'(r_{min}) = 0 \tag{A.25}$$

$$D \geq 0. \tag{A.26}$$

Here n_d is the steady-state measurement data and s_0 is the source term at the edge. We now consider the problem with a Neumann boundary condition for r_{min} and Dirichlet boundary condition for the constant source at r_{max}

$$A(r)n''(r) + B(r)n'(r) + C(r)n(r) = 0 \tag{A.27}$$

$$n(r_{max}) = s_0 \tag{A.28}$$

$$n'(r_{min}) = 0. \tag{A.29}$$

By comparing the above equation with equation (A.21) we conclude that A, B, and C correspond to:

$$A(r) = rD(r) \tag{A.30}$$

$$B(r) = D(r) + rD'(r) - rv(r) \tag{A.31}$$

$$C(r) = v(r) + rv'(r). \tag{A.32}$$

Appendix A. Appendix

We begin the discretization by introducing a radial grid with N points:

$$r_k := r_{min} + \underbrace{\frac{r_{max} - r_{min}}{N - 1}}_{:=h} k \text{ for } k = 0, \ldots, N - 1. \tag{A.33}$$

For every $k = 0, \ldots, N - 1$ we denote the point-wise approximation of the steady-state n as $n_k = n(r_k)$. The same definition applies for $A_k = A(r_k)$, $B_k = B(r_k)$, and $C_k = C(r_k)$. We use second order central finite differences for the first and second derivative of n

$$n''(r_k) \approx n_k'' := \frac{n_{k-1} - 2n_k + n_{k+1}}{h^2}, \quad n'(r_k) \approx n_k' := \frac{-n_{k-1} + n_{k+1}}{2h}. \tag{A.34}$$

We obtain a set of N linear equations:

$$A_k \frac{n_{k-1} - 2n_k + n_{k+1}}{h^2} + B_k \frac{-n_{k-1} + n_{k+1}}{2h} + C_k n_k = 0, \text{ for } k = 0, \ldots, N - 1. \tag{A.35}$$

At the boundaries ($k = 0$ and $k = N - 1$) we get the values n_{-1} and n_N, which have not been defined. We can eliminate n_{-1} and n_N by incorporating the boundary conditions. The Neumann condition applies at r_{min} ($k = 0$):

$$0 = n'(r_{min}) \approx n_0' = \frac{-n_{-1} + n_1}{2h} \Rightarrow n_{-1} = n_1. \tag{A.36}$$

We insert this into the discretized steady-state equation for $k = 0$, yielding a modification that does not contain n_{-1}.

$$A_0 \frac{-2n_0 + 2n_1}{h^2} + C_0 n_0 = 0 \tag{A.37}$$

The Dirichlet boundary condition already tells us the value of $n(r_{max}) = s_0$ and, therefore, we can eliminate one degree of freedom by neglecting the $k = N - 1$ equation, which contained the off-grid value n_N. We insert $n_{N-1} = s_0$ into the $k = N - 2$ equation

$$A_{N-2} \frac{n_{N-3} - 2n_{N-2} + n_{N-1}}{h^2} + B_{N-2} \frac{-n_{N-3} + n_{N-1}}{2h} + C_{N-2} n_{N-2} = 0 \tag{A.38}$$

yielding:

$$A_{N-2} \frac{n_{N-3} - 2n_{N-2} + s_0}{h^2} + B_{N-2} \frac{-n_{N-3} + s_0}{2h} + C_{N-2} n_{N-2} = 0. \tag{A.39}$$

s_0 now introduces an inhomogeneity to the linear system and, therefore, we move it to the right hand side.

$$A_{N-2} \frac{n_{N-3} - 2n_{N-2}}{h^2} + B_{N-2} \frac{-n_{N-3}}{2h} + C_{N-2} n_{N-2} = s_0 \left(-\frac{A_{N-2}}{h^2} - \frac{B_{N-2}}{2h} \right) \tag{A.40}$$

This can be written in a $(N-1) \times (N-1)$ matrix:

$$
\begin{pmatrix}
\frac{-2A_0}{h^2} + C_0 & \frac{2A_0}{h^2} & & & \\
\frac{A_1}{h^2} - \frac{B_1}{2h} & -\frac{2A_1}{h^2} + C_1 & \frac{A_1}{h^2} + \frac{B_1}{2h} & & \\
& \ddots & \ddots & \ddots & \\
& & \frac{A_{N-3}}{h^2} - \frac{B_{N-3}}{2h} & -\frac{2A_{N-3}}{h^2} + C_{N-3} & \frac{A_{N-3}}{h^2} + \frac{B_{N-3}}{2h} \\
& & & \frac{A_{N-2}}{h^2} - \frac{B_{N-2}}{2h} & \frac{2A_{N-2}}{h^2} + C_{N-2}
\end{pmatrix}
$$

$$
\underbrace{\hphantom{xxxxxxxxxxxxxxxxxxxxxxxxxxxxxxx}}_{:=OP}
$$

$$
\cdot \begin{pmatrix} n_0 \\ \vdots \\ n_{N-2} \end{pmatrix} = \begin{pmatrix} 0 \\ \vdots \\ 0 \\ s_0\left(-\frac{A_{N-2}}{h^2} - \frac{B_{N-2}}{2h}\right) \end{pmatrix}. \quad \text{(A.41)}
$$

Since we have not considered the full problem where the modulation is included, but only the steady state, the steady state inversion method can only give v and D up to a scaling factor. By comparing the results obtained by the matrix (A.41) with the analytical solution (5.14) we can check if the matrix is correctly computed. This is important since the same matrix is used when the full problem is solved. For a given frequency ω we extend (A.22) to a time-dependent problem using the Ansatz (A.1) for the modulation. The full problem now reads:

$$
\min_{D,v,s_0,a_0,b_0} \frac{1}{2} \int_0^T \|n + a\sin(\omega t) + b\cos(\omega t) - n_d(t)\|^2_{\mathcal{L}^2(r_{min},r_{max})} dt \quad \text{such that} \quad \text{(A.42)}
$$

$$
\frac{1}{r}\frac{\partial}{\partial r}\left[r\left(D(r)n'(r) - v(r)\cdot n(r)\right)\right] = 0 \quad \text{(A.43)}
$$

$$
n(r_{max}) = s_0 \quad \text{(A.44)}
$$

$$
n'(r_{min}) = 0 \quad \text{(A.45)}
$$

$$
\omega a(r)r + \frac{\partial}{\partial r}\left[r\left(D(r)b'(r) - v(r)b(r)\right)\right]r = 0 \quad \text{(A.46)}
$$

$$
a(r_{max}) = a_0 \quad \text{(A.47)}
$$

$$
a'(r_{min}) = 0 \quad \text{(A.48)}
$$

$$
\frac{\partial}{\partial r}\left[r\left(D(r)a'(r) - v(r)a(r)\right)\right] - \omega b(r)r = 0 \quad \text{(A.49)}
$$

$$
b(r_{max}) = b_0 \quad \text{(A.50)}
$$

$$
b'(r_{min}) = 0 \quad \text{(A.51)}
$$

$$
D \geq 0. \quad \text{(A.52)}
$$

This can be written in matrix form as follows:

$$
\begin{pmatrix} OP & & \\ & \omega r & OP \\ & OP & -\omega r \end{pmatrix} \begin{pmatrix} n_0 \\ a \\ b \end{pmatrix} = 0, \quad \text{(A.53)}
$$

where the matrix OP was outlined in equation (A.41). By now solving the full minimization problem with the finite differences discretization presented above, D and v can be completely determined.

Appendix A. Appendix

Acknowledgements